MODELLING OF THE HELIOSPHERE AND COSMIC RAY TRANSPORT

Jasper L. Snyman, B.Sc.(Hons.)

Dissertation submitted for the degree Master of Science in Physics
at the North-West University

Supervisor: Dr. S.E.S. Ferreira
Co-supervisor: Prof. M.S. Potgieter

December 2007
Potchefstroom
South Africa

MODELLING OF THE HELIOSPHERE AND COSMIC RAY TRANSPORT

JASPER L. SNYMAN

Abstract

A two dimensional hydrodynamic model describing the solar wind interaction with the local interstellar medium, which surrounds the solar system, is used to study the heliosphere both as a steady-state- and dynamic structure. The finite volume method used to solve the associated system of hydrodynamic equations numerically is discussed in detail. Subsequently the steady state heliosphere is studied for both the case where the solar wind and the interstellar medium are assumed to consist of protons only, as well as the case where the neutral hydrogen population in the interstellar medium is taken into account. It is shown that the heliosphere forms as three waves, propagating away from the initial point of contact between the solar wind and interstellar matter, become stationary. Two of these waves become stationary at sonic points, forming the termination shock and bow shock respectively. The third wave becomes stationary as a contact discontinuity, called the heliopause. It is shown that the position and geometry of the termination shock, heliopause and bow shock as well as the plasma flow characteristics of the heliosphere largely depend on the dynamic pressure of either the solar wind or interstellar matter. The heliosphere is modelled as a dynamic structure, including both the effects of the solar cycle and short term variations in the solar wind observed by a range of spacecraft over the past $\sim$ 30 years. The dynamic model allows the calculation of an accurate record of the heliosphere state over the past $\sim$ 30 years. This record is used to predict the time at which the Voyager 2 spacecraft will cross the termination shock. Voyager 1 observations of 10 MeV cosmic ray electrons are then used in conjunction with a cosmic ray modulation model to constrain the record of the heliosphere further. It is shown that the dynamic hydrodynamic model describes the heliosphere accurately within a margin of error of ± 0.7 years and ± 3 AU. The model predicts that Voyager 2 crossed the termination shock in 2007, corresponding to preliminary results from observations indicating that the crossing occurred in August 2007.

Keywords: hydrodynamic, heliosphere, termination shock, solar wind, local interstellar medium, Voyager, finite volume method

Opsomming

'n Twee dimensionele hidrodinamiese model wat die interaksie tussen die sonwind en interstellêre medium beskryf word gebruik om die heliosfeer te bestudeer, beide as 'n tydsonafhanklike en 'n tydsafhanklike struktuur. Die eindige volume metode wat gebruik word om die stelsel van hidrodinamiese vergelykings numeries op te los word noukeurig bespreek. Gevolglik word die heliosfeer ondersoek vir beide die geval waar dit aangeneem word dat die sonwind en interstellêre medium slegs protone bevat, en die geval waar die effek van neutrale waterstof deeltjies in die interstellêre medium ook bygereken word. Dit word gewys dat die struktuur van die heliosfeer uit drie staande golwe bestaan. Die staande golwe vorm sodra golwe wat vanaf die aanvanklike kontakpunt tussen die sonwind en interstellêre medium wegbeweeg, tot stilstand kom. Dit word getoon dat twee van hierdie golwe in staande golwe ontaard by posisies waar die vloeisnelheid van die sonwind en interstellêre medium oorgaan van supersoniese na subsoniese snelhede. Laasgenoemde golwe vorm onderskeidelik die terminasieskok en boegskok. Die derde staande golf vorm as 'n kontakdiskontinuïteit. Weldra word dit getoon dat die plasma vloei sowel as die posisie en geometrie van die terminasieskok, kontakdiskontinuïteit en boegskok beïnvloed word deur die dinamiese druk van beide die sonwind en die interstellêre medium. Beide die sonsiklus en korttermyn veranderings in die sonwind toestand, soos waargeneem deur verskeie ruimtetuie oor die afgelope $\sim$ 30 jaar, word gebruik om die heliosfeer as'n dinamiese struktuur te modelleer. 'n Akkurate rekord van die heliosfeer word uit die dinamiese model bereken en gebruik om te voorspel wanneer Voyager 2 oor die terminasieskok sal beweeg. Die resultate toon dat Voyager 2 gedurende 2007 oor die terminasieskok beweeg het. Dit stem ooreen met waarnemings wat toon dat Voyager 2 die terminasieskok moontlik in Augustus 2007 teëgekom het. Waarnemings van 10 MeV kosmiese straal elektrone deur Voyager 1, tesame met 'n kosmiese straal modulasie model, word gebruik om die akkuraatheid van die rekord van die heliosfeer vas te stel. Dit word getoon dat die heliosfeer akkuraat beskryf word deur die dinamiese hidrodinamiese model binne 'n foutgrens van ± 0.7 jaar en ± 3 AU.

Sleutelwoorde: hidrodinamies, heliosfeer, terminasie skok, sonwind,
interstellêre medium, Voyager, eindige volume metode

Nomenclature

ACR	anomolous cosmic ray
AU	astronomical unit
BS	bow shock
CLIC	cluster of local interstellar clouds
CR	cosmic ray
GCR	galactic cosmic ray
HMF	heliospheric magnetic field
HD	hydrodynamic
HP	heliopause
HS	heliosphere
LIC	local interstellar cloud
LISM	local interstellar medium
MHD	magneto-hydrodynamic
PUI	pick-up ion
SW	solar wind
TS	termination shock

Contents

Chapter 1

Introduction

Broadly speaking, the heliosphere refers to the influence sphere of the Sun ('helios' referring to the ancient Greek god of the Sun). The heliosphere has its origins in the solar wind (SW) which is a highly ionized plasma of solar origin expanding away from the Sun at supersonic velocities. The heliosphere forms due to the interaction between the SW and interstellar matter (here referred to as the local interstellar medium or LISM) surrounding the solar system, where the SW blows a low density bubble in the surrounding interstellar matter.

Early examples of studies modelling the heliosphere can be found in *Parker* (1961); *Axford et al.* (1963) and *Holzer* (1972). By 1970 the hydrodynamic treatment of expanding stellar winds (such as the SW) was well established (see for example the review by *Holzer and Axford,* 1970). These studies formulated the SW-LISM interaction problem to consist of several parts which had to be solved self-consistently: firstly the interaction between ionized particles in the SW and LISM needed to be calculated. Secondly the effect of neutral particles in the LISM on this interaction had to be taken into account. Due to the ionized nature of the SW and LISM both these plasmas carry magnetic fields. Therefore, in addition to the various mutual interactions between ionized and neutral particles a solution to the electrodynamic equations describing the interaction between the magnetic field and the plasma in which it is embedded has to be calculated self-consistently.

As computing power increased solutions to the SW-LISM interaction could be calculated with progressively greater detail. Most of the initial numerical calculations neglected the magnetic field in the SW-LISM interaction. In this regard a model was formulated by *Baranov and Malama* (1993) which treated the interaction between ionized particles in the SW and LISM hydrodynamically. The interaction with the neutral particle population in the LISM is treated kinetically. In 1995 *Pauls et al.* (1995) simplified the formulation of *Baranov and Malama* (1993) by treating the neutral component in the LISM hydrodynamically. While this approach has certain limitations regarding the state of the neutral species, it was successful in capturing the major characteristics of the heliosphere. Subsequent hydrodynamic formulations of the SW-LISM interaction were used in the studies presented by *Pauls and Zank* (1996); *Zank et al.* (1996); *Izmodenov* (1997); *Pauls and Zank* (1997); *Kausch* (1998) and *Fahr et al.* (2000) among others. A

hydrodynamic formulation including a self consistent solution to the magnetic field equations [1] was also developed by *Pogorelov and Semenov* (1997); *Pogorelov and Matsuda* (1998); *Ratkiewicz et al.* (1998); *Pogorelov et al.* (2004) and *Opher et al.* (2006). Recently it has been noted by *Pogorelov et al.* (2007) that these models may over-estimate the effect of the heliospheric and interstellar magnetic fields on the heliospheric geometry.

In this regard the aim of this work is to model the heliosphere realistically and dynamically. Such an exercise has importance both with regard to the heliosphere and astrospheres forming around distant stars. Regarding the latter, hydrodynamical models such as the one discussed and used in this work can be applied to these astrospheres in order to infer properties of the stellar winds forming these structures.

Regarding the heliosphere it will be shown that an accurate record of the heliospheric state over the past 30 years can be obtained by using spacecraft observations of the SW state in conjunction with a purely hydrodynamic model (similar to the model developed by *Fahr et al.*, 2000). The availability of such a record may prove useful in the field of cosmic ray (CR) modulation studies, as is discussed in the next few paragraphs. Furthermore, in researching the link between CR's and the terrestrial climate, knowing the dynamics of the heliosphere may prove to be important (see for example *Scherer et al.*, 2006).

The heliospheric modulation of galactic cosmic rays (GCR's) refers to processes in the heliosphere that act to alter the GCR distribution (the number of particles of a specific energy at a point in space and time) from its value outside the heliosphere to a modulated value inside it. As GCR's encounter the heliosphere modulation processes (dependent on the expanding SW and the heliospheric magnetic field embedded in it) occur. In this regard cosmic ray modulation models depend on the SW flow and the heliospheric geometry. Subsequently cosmic ray modulation models have been developed to include these two effects with increasing detail, as is discussed next.

Due to the relative motion between the Sun and the interstellar matter surrounding the solar system the heliospheric structure is not spherically symmetric. The non-spherical geometry of the heliosphere was included in the cosmic ray modulation models of *Fichtner et al.* (1996b) and *Haasbroek and Potgieter* (1998) amongst others. These studies focused on solving CR transport equations for a region in which the heliospheric geometry is pre-defined. This led to the development of so called 'hybrid' models (see *Kausch*, 1998; *Fahr et al.*, 2000; *Florinski et al.*, 2003; *Ferreira et al.*, 2004a; *Scherer and Ferreira*, 2005; *Ferreira and Scherer*, 2006; *Ferreira et al.*, 2007). In these models a self consistent solution of the SW-LISM interaction is calculated either hydrodynamically or magneto-hydrodynamically. The calculated state of the heliosphere is then used as input to a numerical cosmic ray modulation model. The benefits of the latter approach become evident in the context of time dependent CR modulation studies. In using a time dependent heliospheric model the response of CR's to time dependent variations in the

[1] The set of hydrodynamic equations coupled with the set electrodynamic equations used to solve the magnetic field are referred to as the magneto-hydrodynamic (MHD) equations.

heliosphere can be modelled accurately, as illustrated by the results from *Scherer and Ferreira* (2005) and *Ferreira and Scherer* (2006).

In this dissertation a detailed discussion regarding hydrodynamic modelling of the heliosphere will be given. Emphasis will be placed on the SW flow and the geometry of the heliosphere, as these are important parameters within the context of cosmic ray modulation. The aim is to discuss the different aspects involved in modelling the hydrodynamic heliosphere systematically. To this end the numerical scheme used in solving systems of hydrodynamical equations is discussed, whereafter increasingly complicated descriptions of the SW interaction with the LISM are presented (starting from a 'protons only' description building towards a time dependent, multi-particle model). In this regard parts of this dissertation summarises previous works by *Holzer* (1972, 1989); *Baranov and Malama* (1993); *Pauls et al.* (1995); *Pauls and Zank* (1996); *Zank et al.* (1996); *Izmodenov* (1997); *Pauls and Zank* (1997); *Pogorelov and Semenov* (1997); *Kausch* (1998) and *Fahr et al.* (2000).

Following this discussion, parameter studies will be presented in order to gauge the response of the heliosphere to different assumed states of the SW and interstellar matter. Secondly a brief discussion will be presented on the inclusion of the solar cycle dependent SW in the hydrodynamical model, corresponding to earlier works by *Belcher et al.* (1993); *Whang and Burlaga* (1993); *Karmesin et al.* (1995); *Koyama et al.* (1995); *Pauls and Zank* (1997); *Wang and Belcher* (1999); *Scherer and Fahr* (2003a,b); *Scherer and Ferreira* (2005) and *Ferreira and Scherer* (2006). It will be shown how these studies can be extended to include short term variations in the SW state, which can then be used to calculate an accurate record of the heliosphere over the past $\sim$ 30 years. Regarding the accuracy of this calculated record an estimate will be made as to when the Voyager 2 spacecraft will cross the TS. The correlation between such an estimation and the actual crossing will provide a test of the accuracy of the calculated heliospheric record. Lastly, as an application of cosmic ray modulation models, the calculated record of the heliosphere will be further constrained by using an electron modulation model (similar to the model discussed by *Ferreira et al.*, 2007) in conjunction with 10 MeV cosmic ray electron observations from both the Voyager 1 and 2 spacecraft.

The dissertation will be structured as follows:

In **Chapter 2** a review of the numerical method used to solve a system of hydrodynamic equations is given. This numerical method is used to model the SW interaction with the interstellar medium. The aim of this section is to illuminate the workings of hydrodynamical systems and subsequently provide a theoretical basis for later discussions in this work. It will be shown how a system of linear, constant coefficient hyperbolic partial differential equations can be decoupled into a set of linearly independent advection equations which are easily solvable. Advection implies the transport of a quantity without the quantity affecting the medium.

It will be shown that information propagates via advected quantities in a constant coefficient linear hyperbolic system of equations. This property will be used to solve the more complex

nonlinear, variable coefficient set of Euler equations. It will be shown how the Euler equations can be approximated as a constant coefficient linear hyperbolic system through the procedure of volume averaging. Boundaries between volumes are resolved by calculating the quasi-linear form of the Euler equations, which yields the flux Jacobian. The flux Jacobian is linearised at each cell interface and the system is subsequently evolved in time by calculating fluxes at each cell interface from the advection equations associated with the system. It is shown how the numerical scheme can be applied in a way consistent with physical entropy conditions. The chapter concludes with a discussion on corrections applied to the numerical scheme to improve its accuracy. This is done by applying an alternative solution technique (called the HLLE-solver) for cases where the numerical calculation may produce non-physical results. Secondly it is shown how the numerical scheme can be extended to be second order accurate.

Chapter 3 begins by reviewing observational evidence constraining the states of SW and interstellar matter surrounding the solar system (the latter is referred to as the local interstellar medium, or LISM). The numerical scheme from Chapter 2 is then applied to the SW-LISM interaction for the simplified case where it is assumed that both the SW and LISM consist solely of protons. Using the properties of the solution scheme in Chapter 2 it can be shown that the heliospheric structure necessarily contains two transonic shocks and a contact discontinuity in a steady state. Subsequently the main characteristics of the plasma flow in the heliosphere are discussed as it develops from the numerical solution to the SW-LISM interaction problem. The chapter concludes with a parameter study gauging the sensitivity if the 'protons only' heliospheric geometry and resulting SW plasma flow to different assumed initial states of the SW and LISM.

A more complete description of the SW-LISM interaction includes the effect of neutral atoms in the LISM on the SW-LISM interaction. In **Chapter 4** it is shown how this effect can be included within a hydrodynamical context. A comparison is presented between the heliosphere resulting from the multi-species interaction and results from Chapter 3. In doing so the effect of neutral atoms (and subsequently pick-up ions created through the interaction between SW protons and LISM neutrals) on the heliospheric structure and SW plasma flow can be shown explicitly. The chapter concludes with a parameter study investigating the response of the multi species heliosphere to different assumed initial SW and LISM states (the latter now containing an additional variable describing the neutral atom abundance).

The results presented in Chapters 3 and 4 describe the heliosphere as a steady state structure. In **Chapter 5** the heliosphere is investigated as a dynamic structure. It is shown how the solar cycle dependent SW can be included in the hydrodynamical model describing the SW-LISM interaction. Subsequently the effect of the time dependent SW on the heliosphere is presented. The study is then extended to include short term variations in the SW, as observed by a range of spacecraft. The inclusion of these short term variations as time dependent boundary conditions in the numerical scheme allows for the calculation of a record giving the heliospheric state at different times over the past $\sim$ 30 years. From this record a prediction can be made

as to when Voyager 2 will cross the TS. The correlation between Voyager 2's eventual crossing and its actual crossing will then provide an important test for the accuracy of the calculated heliospheric record. The chapter concludes with an application in cosmic ray modulation. A cosmic ray modulation model, together with 10 MeV electron observations from Voyager 1 and 2 are used to further constrain the heliospheric record calculated in this chapter.

A summary of the results presented in this work is given in **Chapter 6**.

Results from this study have appeared in poster presentations made at the 30^{th} International Cosmic Ray Conference in Mexico and the 36^{th} COSPAR scientific assembly in China (see *Snyman et al.*, 2006). Results were also presented at two annual conferences of the South African Institute of Physics held at the University of the Western Cape in 2006 and the University of the Witwatersrand in 2007.

Chapter 2

Numerics

2.1 Introduction

Systems of non-linear, partial differential equations describing real phenomena seldom present easily obtainable analytical solutions except in the very simplest of cases. Therefore, to obtain useful results numerical algorithms are used to obtain approximate solutions. The aim of this chapter is twofold. The first is to describe in necessary detail the numerical scheme used to calculate the results discussed in later chapters of this work. The second is to provide greater insight into the workings of hydrodynamic systems which are illustrated well through the considerations and physical constraints employed in the development of the numerical scheme.

This chapter starts out by investigating the simplest form of transport in a fluid called one-dimensional advection. It will be shown that ever more complicated systems can be simplified and reduced to a series of one-dimensional advection equations which are easily solvable. Specifically a numerical method using the fact that any linear, constant coefficient hyperbolic system may be decoupled into a set of independent one-dimensional advection equations will be developed. It will then be shown that for the specific case of the Euler equations it is possible to approximate the system as being linear with constant coefficients within some localized volume. The numerical scheme applying to constant coefficient linear systems may then be used to solve the Euler equations in each local volume. Lastly, details specific to the numerical scheme used in this work will be discussed, such as the extension to plane geometry, high resolution methods and entropy fixes. This chapter summarises from *Kausch* (1998) and *LeVeque* (2002).

2.2 The advection equation and linear hyperbolic systems

The study of hydrodynamics begins with the consideration of conserved quantities. Informally the conservation of mass, momentum and energy in a fluid implies that for a certain fluid volume (containing enough particles for the volume to still be considered a fluid) the mass, momentum and energy associated with such a volume may only change due to positive or

negative fluxes at the boundary surface enclosing the volume, or due to sources present within that volume. Formally this may be expressed (borrowing the notation from *LeVeque*, 2002) for some quantity q in one spatial dimension as

$$\frac{d}{dt}\int_{x_1}^{x_2} q(x,t)dx = f(q(x_1,t)) - f(q(x_2,t)) \tag{2.1}$$

here x is the position, t the time and f the flux function dependent on the quantity q at a particular point in space and time. Since Eq.(2.1) states the conservation of q in one dimension, the points x_1 and x_2 constitute the boundary of this one-dimensional volume. If one assumes q to be continuous everywhere Eq.(2.1) reduces to

$$\frac{\partial q(x,t)}{\partial t} + \frac{\partial f(q(x,t))}{\partial x} = 0. \tag{2.2}$$

A simple form of Eq.(2.2) is found for a flux function $f = vq$. v is the velocity, assumed to be constant everywhere (for all times) and independent of q. Inserting $f = vq$ into Eq.(2.2) yields the one-dimensional advection equation

$$q_t + vq_x = 0 \tag{2.3}$$

where the convention is used that subscripts indicate partial differentiation. Eq.(2.3) permits solutions of the form $q(x,t) = \hat{q}(x - vt)$. Therefore, along any trajectory for which $x - vt = C$, where C is a constant, the quantity $\hat{q}(x - vt)$ remains constant. From $x - vt = C$ it follows that the velocity with which $\hat{q}(x - vt)$ propagates is given by

$$\frac{dx}{dt} = v. \tag{2.4}$$

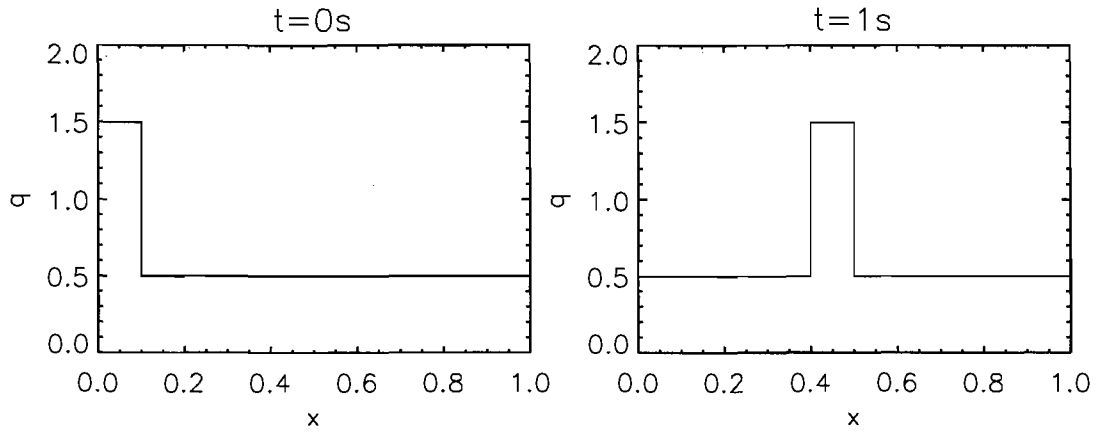

Figure 2.1: The solution to the advection equation. For a specified initial state $q(0,0)$ the state $q(0,t)$ at some later time t is merely the initial state propagated a distance vt from its initial position.

In terms of fluid dynamics this would imply some quantity being transported through the fluid without being changed by the fluid itself. Therefore, knowing the state of such a quantity at one time (say $t = 0$) over a certain domain (say $q(x, 0) = q_0$) implies that at some later time $t = 1$ the whole initial state merely propagated in the direction of the bulk fluid velocity v over a distance $v\Delta t$, where Δt is the elapsed time between the two instants as illustrated in Fig.(2.1).

The simplicity of the advection equation makes it a useful tool in finding solutions to more complex problems. For the case of a linear system of m hyperbolic partial differential equations the system can be decoupled into a set of m independent advection equations, where each independent equation can then be solved separately. From definition a constant coefficient linear system of m equations

$$q_t + Aq_x = 0 \tag{2.5}$$

where

$$q = \begin{bmatrix} q_1 \\ q_2 \\ . \\ . \\ q_m \end{bmatrix} \quad A = \begin{bmatrix} A_{11} & A_{12} & ... & A_{1m} \\ A_{21} & A_{22} & ... & A_{2m} \\ . & . & & . \\ . & . & . & . \\ A_{m1} & A_{m2} & ... & A_{mm} \end{bmatrix} \tag{2.6}$$

is hyperbolic if the $m \times m$ matrix A has real eigenvalues and is diagonalizable. Diagonalizability implies that there exists an invertible matrix R so that $R^{-1}AR$ is a diagonal matrix. Real eigenvalues imply that a set of m eigenvectors r^p exist together with m real eigenvalues λ^p so that

$$Ar^p = \lambda^p r^p \text{ for } p = 1, 2, ..., m. \tag{2.7}$$

Subsequently A is diagonalised by

$$R^{-1}AR = \Lambda \tag{2.8}$$

where

$$\Lambda = \begin{bmatrix} \lambda^1 & 0 & ... & 0 \\ 0 & \lambda^2 & ... & 0 \\ . & . & & . \\ . & . & . & . \\ 0 & 0 & ... & \lambda^m \end{bmatrix} \tag{2.9}$$

and R is the $m \times m$ matrix

$$R = [r^1|r^2|...|r^m] \tag{2.10}$$

with the set of m eigenvectors $r^p, p = 1, 2, ..., m$ of A as its columns. R^{-1} denotes the inverse of R. Eq.(2.5) can now be decoupled into m advection equations by multiplying with R^{-1} and noting that $RR^{-1} = I$, where I is the identity matrix. This yields

$$R^{-1}q_t + R^{-1}ARR^{-1}q_x = 0. \tag{2.11}$$

By letting $w = R^{-1}q$, m independent advection equations

$$w_t + \Lambda w_x = 0 \tag{2.12}$$

are obtained as long as R does not explicitly depend on either x or t. The p'th equation may be written as

$$w_t^p + \lambda^p w_x^p = 0 \text{ for } p = 1, 2, ..., m \tag{2.13}$$

where the p'th flux is given by $f^p = \lambda^p w^p$ analogous to Eq.(2.3).

Decoupling linear hyperbolic equations into independent advection equations provides a hint at developing methods for nonlinear hydrodynamics: if one can define some local fluid volume as approximately linear, a finite set of advection equations will approximately describe the dynamics within that volume. By resolving the boundaries between these volumes the problem may be solved to an arbitrary accuracy. Key to this approach is the Riemann problem, which is considered next.

2.3 The Riemann problem

The Riemann problem for a linear system consists of a hyperbolic equation such as Eq.(2.5) and initial data that is piecewise constant, separated by a jump discontinuity

$$\hat{q}(x) = \begin{cases} q_l & \text{if } x < 0, \\ q_r & \text{if } x > 0. \end{cases} \tag{2.14}$$

From

$$q(x,t) = Rw(x,t) = \left[\begin{array}{cccc} r^1| & r^2| & \ldots & |r^m \end{array} \right] \left[\begin{array}{c} w^1 \\ w^2 \\ . \\ . \\ . \\ w^m \end{array} \right] \tag{2.15}$$

it follows that $q(x,t)$ can be viewed as a superposition of the eigenvectors r^p, each weighed by the corresponding value of $w^p(x,t)$. This yields

$$q(x,t) = \sum_{p=1}^{m} w^p(x,t) r^p \tag{2.16}$$

expressing $q(x,t)$ as a superposition of m simple waves. Due to the hyperbolicity of the linear system (the fact that A in Eq.2.5 is diagonalizable) these simple waves are independent of each other. The data to the left and right of $x = 0$ in Eq.(2.14) can be decoupled analogously to Eq.(2.16) as

$$q_l = \sum_{p=1}^{m} w_l^p r^p \quad \text{and} \quad q_r = \sum_{p=1}^{m} w_r^p r^p. \tag{2.17}$$

The only true difference between the initial states to the left and right of $x = 0$ is in the values of the w_l^p's and w_r^p's since it is assumed that the eigenvectors r^p have no spatial dependence. Term for term comparison regarding the summations in Eq.(2.17) allow for the Riemann data in Eq.(2.14) to be expressed compactly as a difference in each of the w^p's as

$$\hat{w}^p(x) = \begin{cases} w_l^p & \text{if } x < 0, \\ w_r^p & \text{if } x > 0. \end{cases} \tag{2.18}$$

For an advection equation of the form

$$w_t + \lambda w_x = 0 \tag{2.19}$$

with the initial condition $w(x,0) = \hat{w}(x)$, the quantity $\hat{w}(x)$ merely advects along x with a velocity λ. For the Riemann problem this implies that the p'th discontinuity in Eq.(2.18) simply advects along x with a velocity given by the p'th eigenvalue λ^p of A. Therefore,

$$w^p(x,t) = \begin{cases} w_l^p & \text{if } x - \lambda^p t < 0, \\ w_r^p & \text{if } x - \lambda^p t > 0. \end{cases} \tag{2.20}$$

Subsequently the time dependent state $q(x,t)$ of the system initially described by Eq.(2.14) is given by

$$q(x,t) = \sum_{p:\lambda^p<x/t} w_r^p r^p + \sum_{p:\lambda^p>x/t} w_l^p r^p \tag{2.21}$$

where the summation subscripts $p : \lambda^p > x/t$ and $p : \lambda^p < x/t$ indicate values of p such that x/t is positive or negative respectively. The p'th discontinuity entails a jump in q given by

$$(w_r^p - w_l^p)r^p = \alpha^p r^p \tag{2.22}$$

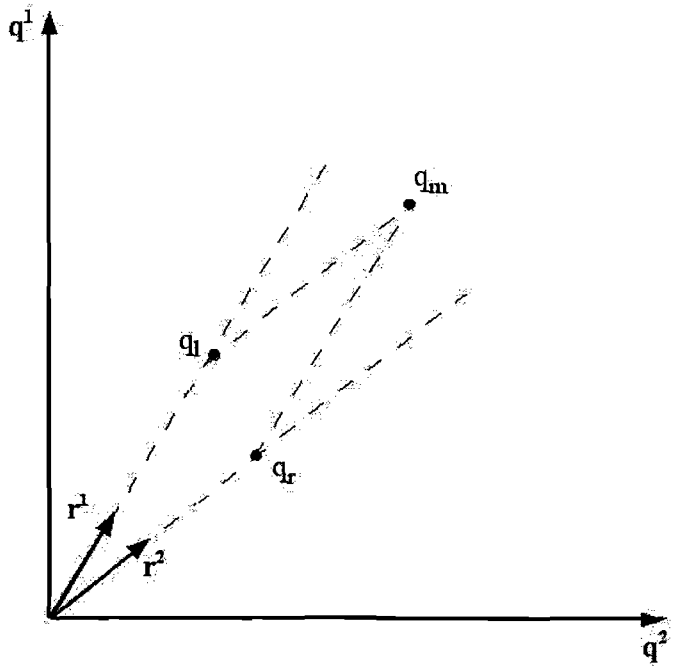

Figure 2.2: In two dimensional phase space two states (q_l and q_r) can be connected to some other state by a single propagating discontinuity if the state lies on a line parallel to either of the eigenvectors r^1 or r^2. In the case illustrated above an intermediate state is needed to connect q_l and q_r. The intermediate state lies at the intersection of two lines parallel to r^2 and r^1 drawn from q_l and q_r respectively.

This implies that all the $w_{l,r}^p$ states that can be connected by a single discontinuity lie on a loci parallel to the p'th eigenvector r^p. This has important implications for how an initially discontinuous state evolves with time.

Consider the Riemann data in Eq.(2.14). For a system where $q = (q^1, q^2)$ each state (q_l and q_r) may be expressed as points in a phase space defined by q^1 and q^2 as shown in Fig.(2.2). From Eq.(2.17) q_l and q_r may be written as

$$q_l = w_l^1 r^1 + w_l^2 r^2 \quad q_r = w_r^1 r^1 + w_r^2 r^2 \tag{2.23}$$

where

$$w_l^1 - w_r^1 = \alpha^1 \quad w_l^2 - w_r^2 = \alpha^2. \tag{2.24}$$

Momentarily consider the case where $\alpha^2 = 0$. For such a case the discontinuity between q_l and q_r is described completely by a discontinuity in the w^1's. Since all the w^1-values that can be connected by a single discontinuity lie on a line in phase space parallel to r^1 it implies that q_l and q_r can be connected by a single discontinuity and that q_l and q_r lie on the same line parallel to r^1. The solution to the Riemann problem for such a case will contain a single discontinuity connecting two different states similar to q_l and q_r at all times.

For the case shown in Fig.(2.2) $\alpha^1, \alpha^2 \neq 0$. The system evolves with time through quantities propagating parallel to the eigenvectors r^1 and r^2 in phase space. In configuration space this implies that waves propagate away from the initial discontinuity at $x = 0$ changing the states to the left and right of $x = 0$. Since these quantities propagate at finite velocities a solution at any time will contain undisturbed regions along x which resemble the initial states q_l and q_r. Between these undisturbed states an intermediate state forms due to the waves propagating away from $x = 0$. In phase space this implies that an intermediate state q_m forms at the intersection of the loci parallel to r^2 and r^1 (from q_l and q_r respectively) as shown in Fig.(2.2).

In m-dimensional phase space multiple intersections are possible and subsequently the time evolution of a system initially described by Eq.(2.14) may contain up to $m - 1$ intermediate states. Using the above mentioned analyses it is, therefore, possible to determine the structure of the solution to the Riemann problem at different times. In section 3.3 the above analyses will be used to show that in the context of hydrodynamics the solution to the Riemann problem consists of two transonic waves and a contact discontinuity. However, before such an application can be considered a numerical method using linear advection equations to obtain a solution to a set linear hyperbolic equations is described.

2.4 Finite volume methods for linear systems

In many nonlinear hyperbolic differential problems, even though initial data may be continuous, shock waves and contact discontinuities may form at later times. If this is the case, the conservation equation (Eq.2.2) cannot hold since it assumes a continuous state $q(x,t)$ for all x and t. However, the integral form of this conservation equation (Eq.2.1) makes no such assumption regarding continuity. Therefore, in developing numerical methods using finite volumes (based on Eq.2.1) issues of continuity are sidestepped.

The first step in implementing finite volume methods is to subdivide the domain over which the initial data extends into several cells (or volumes) and average the data within each cell. In one dimension the i'th cell C_i is centred around x_i with boundaries at $x_i - \frac{1}{2}$ and $x_i + \frac{1}{2}$. In the lowest order approximation the state $q(x, t_n)$ at time $t = t_n$ in each cell is averaged according to

$$Q_i^n = \frac{1}{\Delta x} \int_{C_i} q(x, t_n) dx \tag{2.25}$$

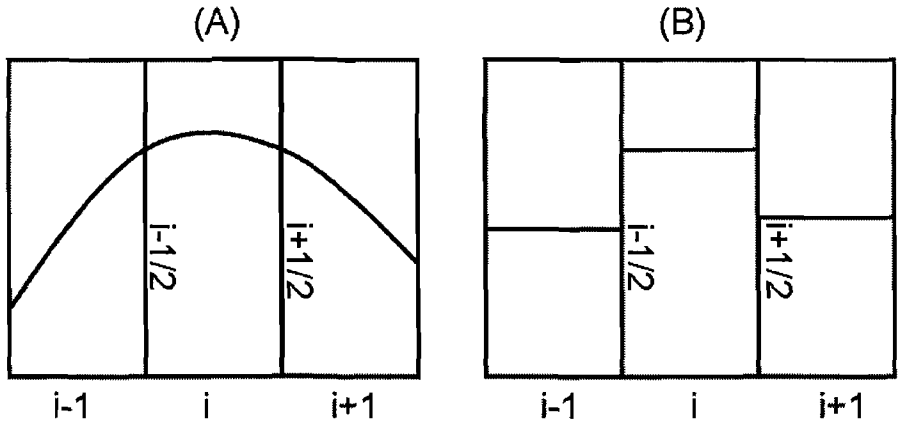

Figure 2.3: Continuous initial data (A) and volume averaged discrete data (B).

where Δx is the cell dimension and integration over the volume C_i implies integration over the range Δx. In the limit $\Delta x \to 0$, $Q_i^n \to q(x_i, t_n)$. The process of cell-averaging is illustrated in Fig.(2.3) where some quantity in (A) is averaged according to Eq.(2.25) to obtain piecewise constant data (B). This effectively reduces the problem to finding solutions to the various Riemann problems at each cell interface. For constant coefficient linear problems (such as Eq.2.5) the Riemann problem is easily solvable using the formalism developed in sections 2.2 and 2.3. Substituting Q_i^n and Q_{i-1}^n for $q(x,t)$ in Eq.(2.16) and using Eq.(2.22) the difference between Q_i and Q_{i-1} may be expressed as

$$Q_i^n - Q_{i-1}^n = \sum_{p=1}^{m} (w_i^p - w_{i-1}^p) r^p = \sum_{p=1}^{m} \alpha_{i-1/2}^p r^p. \tag{2.26}$$

The j'th discontinuity $\alpha_{i-1/2}^j r^j$ propagates with a velocity of magnitude λ^j, which is the eigenvalue of A (in Eq.2.5) corresponding to the j'th eigenvector r^j of A. Implicit to Eq.(2.26) is that a form of A defined over a domain containing the discontinuity between Q_i and Q_{i-1} is used. In section 2.6 it will be shown how this form is obtained for the specific case of the Euler-equations. For the rest of this section it is assumed that λ^j (and therefore A) exists. Assume that λ^j is positive. Therefore, during a time step Δt it propagates a distance $\Delta t \lambda^j$ into cell C_i and affects the average Q_i^n by the amount

$$-\frac{\Delta t \lambda^j}{\Delta x} \alpha_{i-1/2}^j r^j. \tag{2.27}$$

Note that if $w_{i-1}^j < w_i^j$ one would expect the cell average Q_i^n to decrease due to a flux from C_i into C_{i-1}. This is the reason for the minus in Eq.(2.27). It is also noted that Q_i^n is affected by all right going quantities from the boundary at $i - \frac{1}{2}$ and all left going quantities from the boundary at $i + \frac{1}{2}$. Defining $(\lambda^p)^+ = \max(0, \lambda^p)$ and $(\lambda^p)^- = \min(0, \lambda^p)$ (from *Kausch*, 1998) the effect over one time step on Q_i^n may be written as

$$Q_i^{n+1} = Q_i^n - \frac{\Delta t}{\Delta x}\left[\sum_{p=1}^{m}(\lambda^p)^+\alpha_{i-1/2}^p r^p + \sum_{p=1}^{m}(\lambda^p)^-\alpha_{i+1/2}^p r^p\right]. \tag{2.28}$$

The integral form of the conservation equation (Eq.2.1) states that a quantity within some volume (in this case the averaged quantity in C_i) may only change due to fluxes at the volume boundary, or sources being present within the volume. Therefore, the second term on the right side of Eq.(2.28) should be an approximation of the fluxes affecting cell C_i. In the context of Eq.(2.25) the fluxes at the boundaries at $i-\frac{1}{2}$ and $i+\frac{1}{2}$ are given by

$$\frac{d}{dt}Q_i^n = \frac{1}{\Delta x}\frac{d}{dt}\int_{C_i} q(x,t_n)dx = f(q(x_{i-1/2},t)) - f(q(x_{i+1/2},t)). \tag{2.29}$$

By integrating over one time step ($t_{n+1} = t_n + \Delta t$) one obtains

$$Q_i^{n+1} = Q_i^n - \frac{\Delta t}{\Delta x}(F_{i+1/2}^n - F_{i-1/2}^n) \tag{2.30}$$

where

$$F_{i\pm1/2}^n = \frac{1}{\Delta t}\int_{t_n}^{t_{n+1}} f(q(x_{i\pm1/2},t))dt. \tag{2.31}$$

Comparing Eq.(2.31) with Eq.(2.28) it is seen that

$$F_{i+1/2}^n = \textstyle\sum_{p=1}^m(\lambda^p)^-\alpha_{i+1/2}^p r^p \quad F_{i-1/2}^n = -\sum_{p=1}^m(\lambda^p)^+\alpha_{i-1/2}^p r^p. \tag{2.32}$$

Explicitly this relation can be shown to hold for constant coefficient linear systems by noting the following: in decoupling a specific Riemann problem at some interface $i-\frac{1}{2}$ into a set of advection equations the dynamics of the system are reduced to a set of discontinuities advecting to the left and right of the interface at $i-\frac{1}{2}$. This implies that the value immediately to the left of the boundary at $i-\frac{1}{2}$ after some small time increase $\xi << \Delta t$ is given by

$$Q_{i-1/2,l} = Q_{i-1} + \sum_{p:\lambda^p<0}^{m} \alpha_{i-1/2}^p r^p \tag{2.33}$$

where the summation subscript indicates summation over all values of p for which λ^p is negative (therefore taking into account all the discontinuities that propagate into cell C_{i-1} from the interface $i-\frac{1}{2}$). For constant coefficient linear systems the flux function at some point x and time t is (from Eq.2.5) $Aq(x,t)$. Using average quantities the flux at $i-\frac{1}{2}$ is approximately

$$F_{i-1/2}^n = AQ_{i-1/2,l} = AQ_{i-1} + A\sum_{p:\lambda^p<0}^{m} \alpha_{i-1/2}^p r^p = AQ_{i-1} + \sum_{p:\lambda^p<0}^{m} \alpha_{i-1/2}^p Ar^p. \tag{2.34}$$

Since $Ar^p = \lambda^p r^p$

$$F^n_{i-1/2} = AQ_{i-1} + \sum_{p=1}^{m} (\lambda^p)^- \alpha^p_{i-1/2} r^p. \tag{2.35}$$

Alternatively using values immediately to the right of $i - \frac{1}{2}$

$$F^n_{i-1/2} = AQ_i - \sum_{p=1}^{m} (\lambda^p)^+ \alpha^p_{i-1/2} r^p. \tag{2.36}$$

Similarly the flux at $i + \frac{1}{2}$ is found to be

$$F^n_{i+1/2} = AQ_i + \sum_{p=1}^{m} (\lambda^p)^- \alpha^p_{i+1/2} r^p \tag{2.37}$$

and

$$F^n_{i+1/2} = AQ_{i+1} - \sum_{p=1}^{m} (\lambda^p)^+ \alpha^p_{i+1/2} r^p. \tag{2.38}$$

By substituting Eqs.(2.36) and (2.37) into Eq.(2.30) an expression identical to Eq.(2.28) is obtained. A useful expression for the flux at a specific boundary is obtained by combining Eqs.(2.35) and (2.36) as

$$F^n_{i-1/2} = \frac{1}{2} \left[AQ_{i-1} + AQ_i - \sum_{p=1}^{m} |\lambda^p| \alpha^p_{i-1/2} r^p \right]. \tag{2.39}$$

By using Eq.(2.39) in Eq.(2.30) a time marching algorithm is obtained. Initial data are made piecewise constant through the cell averaging procedure in Eq.(2.25) which yields a series of Riemann problems at each cell interface. The Riemann problem is then solved at each interface for a time step Δt small enough so that

$$\frac{\lambda^{max} \Delta t}{\Delta x} < 1 \tag{2.40}$$

where λ^{max} is the largest eigenvalue of A over all x during a specific time step. This ensures that information cannot propogate further than one cell dimension within each timestep. Therefore, information from cell C_i can only affect cells C_{i-1} and C_{i+1} during each timestep. This is known as the CFL-condition (see *LeVeque*, 2002).

The method described above is valid for linear, constant coefficient systems. However, the problems discussed in this work will deal primarily with nonlinear systems such as the Euler equations (discussed next). It will be shown in section 2.6 that it is possible to approximate

such a system as being a constant coefficient, linear system within some local volume and in doing so the formalism developed in this section can be applied to obtain numerical solutions.

2.5 The one-dimensional Euler equations

Generally the one-dimensional Euler equations are expressed as

$$\begin{bmatrix} \rho \\ \rho v \\ E \end{bmatrix}_t + \begin{bmatrix} \rho v \\ \rho v^2 + P \\ (E+P)v \end{bmatrix}_x = 0 \tag{2.41}$$

where ρ is the density, v the bulk velocity, P the pressure and E the energy associated with the fluid at a point in space and time. Subscripts indicate partial differentiation as before. The system is nonlinear since the quantities ρ, v, P and E are interdependent. However, a few simplifications may be made considering an equation of state that links the above mentioned quantities in some way. For an ideal gas the equation of state is

$$P = R\rho T \tag{2.42}$$

where R is the universal gas constant divided by the molecular weight of the gas. If it is assumed that the internal energy of the fluid is only dependent on the fluid temperature (implying that the fluid is polytropic), the relation

$$e = c_v T \tag{2.43}$$

holds where e is the internal energy of the fluid and c_v the specific heat at constant volume. If it is assumed that the fluid is also monatomic, i.e. the particles that constitute the fluid have only three translational degrees of freedom, then from the equipartition of energy it follows that

$$e = \frac{3}{2} nkT. \tag{2.44}$$

With $nk = R$ it follows that

$$c_v = \frac{3}{2} R. \tag{2.45}$$

Since the relation between the specific heats at constant volume and at constant pressure is

$$c_p - c_v = R \tag{2.46}$$

it follows that

$$c_p = \frac{5}{2}R. \tag{2.47}$$

The ratio of specific heats are

$$\gamma = \frac{c_p}{c_v} = \frac{5}{3}. \tag{2.48}$$

From Eq.(2.43) using $T = P/R\rho$ the internal energy is expressed as

$$e = \frac{c_v}{R}\frac{P}{\rho} = \frac{P}{(\gamma - 1)\rho} \tag{2.49}$$

The total energy of the fluid is given by the sum of the internal energy of each particle and the kinetic energy of the fluid. Therefore,

$$E = \rho e + \frac{1}{2}\rho v^2 = \frac{P}{\gamma - 1} + \frac{1}{2}\rho v^2. \tag{2.50}$$

The equation of state allows for the expression of the total energy in terms of ρ and P. Using this expression for the total energy the Euler equations for a polytropic, monatomic, ideal gas are (from *LeVeque*, 2002)

$$\begin{bmatrix} \rho \\ \rho v \\ E \end{bmatrix}_t + \begin{bmatrix} \rho v \\ \rho v^2 + P \\ (\frac{\gamma}{\gamma - 1}P + \frac{1}{2}\rho v^2)v \end{bmatrix}_x = 0. \tag{2.51}$$

Regarding the discussion in section 2.4 it is preferable to obtain a form of the Euler equations similar to Eq.(2.5). In general a nonlinear system such as $q(x,t)_t + f(q(x,t))_x$ can be written in the so called quasi-linear form given by

$$q_t + f'(q)q_x = 0 \tag{2.52}$$

where the notation $\frac{df}{dq} = f'(q)$ is used. $f'(q)$ is called the flux Jacobian of the system. For

$$q = \begin{bmatrix} \rho \\ \rho v \\ E \end{bmatrix} \tag{2.53}$$

$f'(q)$ is computed as (from *LeVeque*, 2002)

$$f'(q) = \begin{bmatrix} 0 & 1 & 0 \\ \frac{1}{2}(\gamma-3)v^2 & (3-\gamma)v & \gamma-1 \\ \frac{1}{2}(\gamma-1)v^3 - vH & H-(\gamma-1)v^2 & \gamma v \end{bmatrix} \tag{2.54}$$

where $H = \frac{E+P}{\rho}$ is the total specific enthalpy (the calculation of $f'(q)$ for a two dimensional system is explicitly shown in section 2.7). The eigenvalues of $f'(q)$ are (see *LeVeque*, 2002)

$$\lambda^1 = v - c \quad \lambda^2 = v \quad \lambda^3 = v + c \tag{2.55}$$

where c is the local speed of sound, defined as

$$c = \sqrt{\frac{\gamma P}{\rho}} = \sqrt{(\gamma-1)\left(H - \frac{1}{2}v^2\right)}. \tag{2.56}$$

The three eigenvalues in Eq.(2.55) correspond to three eigenvectors

$$r^1 = \begin{bmatrix} 1 \\ v-c \\ H-vc \end{bmatrix}; \quad r^2 = \begin{bmatrix} 1 \\ v \\ \frac{1}{2}v^2 \end{bmatrix}; \quad r^3 = \begin{bmatrix} 1 \\ v+c \\ H+vc \end{bmatrix}. \tag{2.57}$$

Using the eigenvalues and eigenvectors of the flux Jacobian allows for a numerical solution to the Euler equations based on the finite volume method discussed in the previous section. By subdividing initial data into cell averaged quantities it is ensured that the values of ρ, ρv and E are constant within each cell during a time step Δt. Therefore, the flux within each cell is also constant over the same interval implying that the Euler equations within each cell may be approximated as a constant coefficient, linear system. All that remains is finding a suitable form of the flux Jacobian at each cell interface. This is done in the next section.

2.6 Godunov's method for one-dimensional nonlinear systems

Using the integral form of a conservation equation (as shown in Eq.2.1) implies that the quantity within a certain volume can only change due to fluxes at the edges of such a volume. Determining these fluxes for piecewise constant data requires determining the value of A in Eq.(2.5) at each cell interface $i \pm \frac{1}{2}$. Comparing Eqs.(2.5) and (2.52) shows that the flux Jacobian calculated for the Euler-equations has the same role as the A in Eq.(2.5). This implies that the flux Jacobian must be known at each cell interface for the system to be evolved in time. In order to obtain an approximate solution the flux Jacobian is linearised around the cell interface at $i \pm \frac{1}{2}$. The advantage of this method is that it yields linearised eigenvalues and eigenvectors at each cell interface which can be used in Eq.(2.39).

In order for such a method to be consistent with the original nonlinear problem the linearised matrix at $i \pm \frac{1}{2}$ should be diagonalisable with real eigenvalues and approximate $f'(\overline{q})$ as the cell averages $Q_i, Q_{i-1} \rightarrow \overline{q}$.

The matrix $f'(q)$ is linearised by integrating along a path in phase space connecting Q_i and Q_{i-1}. The specific details of this integration was proposed by Roe (see *LeVeque*, 2002, p.319 for reference). An invertible parameter vector $z(q)$ is introduced mapping the cell averages Q_i and Q_{i-1} to new quantities Z_i and Z_{i-1}. Integration is done along a path parameterised by

$$z(\xi) = Z_{i-1} + (Z_i - Z_{i-1})\xi \tag{2.58}$$

where $0 \leq \xi \leq 1$. Therefore, the resulting flux between Q_i and Q_{i-1} for some interval Δt can be written as

$$f(Q_i) - f(Q_{i-1}) = \int_0^1 \frac{df(z(\xi))}{d\xi} d\xi = \int_0^1 \frac{df(z(\xi))}{dz} z'(\xi) d\xi. \tag{2.59}$$

Since Q_i and Q_{i-1} are constant over the interval Δt it implies that $Z_i - Z_{i-1}$ is also constant over this interval. Since $z'(\xi) = Z_i - Z_{i-1}$ it follows that

$$f(Q_i) - f(Q_{i-1}) = \left[\int_0^1 \frac{df(z(\xi))}{dz} d\xi\right] (Z_i - Z_{i-1}). \tag{2.60}$$

For $Q_i - Q_{i-1}$ this yields

$$Q_i - Q_{i-1} = \int_0^1 \frac{dq(z(\xi))}{d\xi} d\xi = \int_0^1 \frac{dq(z(\xi))}{dz} z'(\xi) d\xi \tag{2.61}$$

and as before this leads to

$$Q_i - Q_{i-1} = \left[\int_0^1 \frac{dq(z(\xi))}{dz} d\xi\right] (Z_i - Z_{i-1}). \tag{2.62}$$

Let

$$\hat{C}_{i-1/2} = \int_0^1 \frac{df(z(\xi))}{dz} d\xi \tag{2.63}$$

and

$$\hat{B}_{i-1/2} = \int_0^1 \frac{dq(z(\xi))}{dz} d\xi. \tag{2.64}$$

This implies that

$$f(Q_i) - f(Q_{i-1}) = \hat{C}_{i-1/2}\hat{B}^{-1}_{i-1/2}(Q_i - Q_{i-1}) \tag{2.65}$$

For $\hat{C}_{i-1/2}\hat{B}^{-1}_{i-1/2} = \hat{A}_{i-1/2}$ the matrix $\hat{A}_{i-1/2}$ from Eq.(2.65) defines a linear matrix approximating $f'(q)$ since Eq.(2.65) divided by $Q_i - Q_{i-1}$ reduces to $f'(q)$ as $\Delta x \to 0$. For the one-dimensional Euler equations an appropriate choice of z is $z = \rho^{-1/2}q$ (see *LeVeque*, 2002). This implies that for

$$q = \begin{bmatrix} \rho \\ \rho v \\ E \end{bmatrix} = \begin{bmatrix} q_1 \\ q_2 \\ q_3 \end{bmatrix} \quad \text{and} \quad f(q) = \begin{bmatrix} \rho v \\ \rho v^2 + P \\ \left(\frac{\gamma P}{\gamma - 1} + \frac{1}{2}\rho v^2\right) v \end{bmatrix} \tag{2.66}$$

z may be expressed as

$$z = \begin{bmatrix} \sqrt{\rho} \\ \sqrt{\rho} v \\ \frac{E}{\sqrt{\rho}} \end{bmatrix} = \begin{bmatrix} z_1 \\ z_2 \\ z_3 \end{bmatrix}. \tag{2.67}$$

q and $f(q)$ are written in terms of z as

$$q(z) = \begin{bmatrix} z_1^2 \\ z_1 z_2 \\ z_1 z_3 \end{bmatrix} \quad \text{and} \quad f(q(z)) = \begin{bmatrix} z_1 z_2 \\ \frac{1}{2}z_2^2 + (\gamma - 1) z_1 z_3 \\ z_2 z_3 + \frac{1}{2}\frac{\gamma - 2}{\gamma - 1}\frac{z_2^3}{z_1} \end{bmatrix}. \tag{2.68}$$

Subsequently

$$\frac{dq}{dz} = \begin{bmatrix} 2z_1 & 0 & 0 \\ z_2 & z_1 & 0 \\ z_3 & 0 & z_1 \end{bmatrix} \quad \text{and} \quad \frac{df}{dz} = \begin{bmatrix} z_2 & z_1 & 0 \\ (\gamma - 1) z_3 & z_2 & (\gamma - 1) z_1 \\ -\frac{1}{2}\frac{\gamma - 2}{\gamma - 1}\frac{z_2^3}{z_1^2} & z_3 + \frac{3}{2}\frac{\gamma - 2}{\gamma - 1}\frac{z_2^2}{z_1} & z_2 \end{bmatrix}. \tag{2.69}$$

Setting

$$z = Z_{i-1} + (Z_i - Z_{i-1})\xi = \begin{bmatrix} z_1 \\ z_2 \\ z_3 \end{bmatrix} = \begin{bmatrix} \sqrt{\rho_{i-1}} - (\sqrt{\rho_i} - \sqrt{\rho_{i-1}})\xi \\ \sqrt{\rho_{i-1}} v_{i-1} - (\sqrt{\rho_i} v_i - \sqrt{\rho_{i-1}} v_{i-1})\xi \\ \frac{E_{i-1}}{\sqrt{\rho_{i-1}}} - (\frac{E_i}{\sqrt{\rho_i}} - \frac{E_{i-1}}{\sqrt{\rho_{i-1}}})\xi \end{bmatrix} \tag{2.70}$$

each element in Eq.(2.69) can be integrated to obtain $\hat{C}_{i-1/2}$ and $\hat{B}_{i-1/2}$ in Eq.(2.65). By inverting $\hat{B}_{i-1/2}$ it is found (from *LeVeque*, 2002) that for the Euler equations

$$\hat{A}_{i-1/2} = \begin{bmatrix} 0 & 1 & 0 \\ \frac{1}{2}(\gamma - 3)\hat{v}^2 & (3 - \gamma)\hat{v} & \gamma - 1 \\ \frac{1}{2}(\gamma - 1)v^3 - \hat{v}\hat{H} & \hat{H} - (\gamma - 1)\hat{v}^2 & \gamma \hat{v} \end{bmatrix} \tag{2.71}$$

where the Roe averages $\hat{v}$ and $\hat{H}$ are (from *LeVeque*, 2002)

$$\hat{v} = \frac{\sqrt{\rho_{i-1}}v_{i-1} + \sqrt{\rho_i}v_i}{\sqrt{\rho_{i-1}} + \sqrt{\rho_i}} \quad \hat{H} = \frac{(E_{i-1} + p_{i-1})/\sqrt{\rho_{i-1}} + (E_i + p_i)/\sqrt{\rho_i}}{\sqrt{\rho_{i-1}} + \sqrt{\rho_i}}. \tag{2.72}$$

The eigenvalues in Eq.(2.55) become

$$\hat{\lambda}^1 = \hat{v} - \hat{c} \quad \hat{\lambda}^2 = \hat{v} \quad \hat{\lambda}^3 = \hat{v} + \hat{c} \tag{2.73}$$

where the Roe average of the local sound speed is

$$\hat{c} = \sqrt{(\gamma - 1)\left(\hat{H} - \frac{1}{2}\hat{v}^2\right)}. \tag{2.74}$$

The eigenvectors from Eq.(2.57) are now given by

$$\hat{r}^1 = \begin{bmatrix} 1 \\ \hat{v} - \hat{c} \\ \hat{H} - \hat{v}\hat{c} \end{bmatrix} \quad \hat{r}^2 = \begin{bmatrix} 1 \\ \hat{v} \\ \frac{1}{2}\hat{v}^2 \end{bmatrix} \quad \hat{r}^3 = \begin{bmatrix} 1 \\ \hat{v} + \hat{c} \\ \hat{H} + \hat{v}\hat{c} \end{bmatrix}. \tag{2.75}$$

Using the Roe averaged values and the fact that the fluxes within each cell are constant Eq.(2.39) becomes

$$F^n_{i-1/2} = \frac{1}{2}\left[f(Q^n_{i-1}) + f(Q^n_i) - \sum_{p=1}^{3} |\hat{\lambda}^p| \alpha^p_{i-1/2} \hat{r}^p\right] \tag{2.76}$$

where

$$f(Q^n_i) = \begin{bmatrix} \rho^n_i v^n_i \\ \rho^n_i (v^n_i)^2 + P^n_i \\ (\frac{\gamma}{\gamma - 1} P^n_i + \frac{1}{2}\rho (v^n_i)^n) v^n_i \end{bmatrix} \tag{2.77}$$

and ρ^n_i, v^n_i and P^n_i are cell averaged quantities during time interval t_n. All that remains is calculating the values of the $\alpha^p_{i-1/2}$ in Eq.(2.76). From Eq.(2.15) it follows that

$$\begin{bmatrix} w(x,t)^1 \\ w(x,t)^2 \\ w(x,t)^3 \end{bmatrix} = R^{-1} \begin{bmatrix} q^1(x,t) \\ q^2(x,t) \\ q^3(x,t) \end{bmatrix} \tag{2.78}$$

where R^{-1} is the inverse of the matrix R and R has the three eigenvectors r^1, r^2 and r^3 as its column vectors. Since R^{-1} has no explicit time or spatial dependence within each cell over

the time step Δt the above can be used to express the difference between two states within adjacent cells as

$$\begin{bmatrix} w_i^1 - w_{i-1}^1 \\ w_i^2 - w_{i-1}^2 \\ w_i^3 - w_{i-1}^3 \end{bmatrix} = \begin{bmatrix} \alpha_{i-1/2}^1 \\ \alpha_{i-1/2}^2 \\ \alpha_{i-1/2}^3 \end{bmatrix} = R^{-1} \begin{bmatrix} \rho_i^n - \rho_{i-1}^n \\ \rho_i^n v_i^n - \rho_{i-1}^n v_{i-1}^n \\ E_i^n - E_{i-1}^n \end{bmatrix} \tag{2.79}$$

here

$$Q_i^n - Q_{i-1}^n = \begin{bmatrix} \rho_i^n - \rho_{i-1}^n \\ \rho_i^n v_i^n - \rho_{i-1}^n v_{i-1}^n \\ E_i^n - E_{i-1}^n \end{bmatrix} \tag{2.80}$$

and ρ_i^n, v_i^n and E_i^n are the cell averaged density, velocity and energy in cell C_i at time t_n. Since the value of R (and subsequently R^{-1}) must be constant for the two adjacent cells C_i and C_{i-1}, an appropriate form to use for R is obtained from the Roe averaged eigenvectors in Eq.(2.75) as

$$\hat{R} = \begin{bmatrix} 1 & 1 & 1 \\ \hat{v} - \hat{c} & \hat{v} & \hat{v} + \hat{c} \\ \hat{H} - \hat{v}\hat{c} & \frac{1}{2}\hat{v}^2 & \hat{H} + \hat{v}\hat{c} \end{bmatrix}. \tag{2.81}$$

The inverse of $\hat{R}$ is calculated to be

$$\hat{R}^{-1} = \begin{bmatrix} -\frac{1}{2} + \frac{\hat{v}}{2\hat{c}} + \frac{\hat{H}(\gamma-1)}{2\hat{c}^2} & -\frac{1}{2\hat{c}} - \frac{\hat{v}(\gamma-1)}{2\hat{c}^2} & \frac{(\gamma-1)}{2\hat{c}^2} \\ 2 - \frac{\hat{H}(\gamma-1)}{\hat{c}^2} & \frac{\hat{v}(\gamma-1)}{\hat{c}^2} & -\frac{(\gamma-1)}{\hat{c}^2} \\ -\frac{1}{2} - \frac{\hat{v}}{2\hat{c}} + \frac{\hat{H}(\gamma-1)}{2\hat{c}^2} & \frac{1}{2\hat{c}} - \frac{\hat{v}(\gamma-1)}{2\hat{c}^2} & \frac{(\gamma-1)}{2\hat{c}^2} \end{bmatrix}. \tag{2.82}$$

Eq.(2.79) is now used to calculated the $\alpha_{i-1/2}^p$ values. For the differences $\rho_i - \rho_{i-1}$, $\rho_i v_i - \rho_{i-1} v_{i-1}$ and $E_i - E_{i-1}$ (dropping the n-superscripts) it is assumed that

$$\begin{aligned} &\rho_i - \rho_{i-1} = \Delta\rho \\ &v_i - v_{i-1} = \Delta v \\ &\rho_i v_i - \rho_{i-1} v_{i-1} = \rho_i \Delta v + v_{i+1} \Delta\rho \approx \hat{\rho}\Delta v + \hat{v}\Delta\rho \\ &P_i - P_{i-1} = \Delta P \\ &E_i - E_{i-1} = \tfrac{\Delta P}{\gamma-1} + \tfrac{1}{2} v_i^2 \Delta\rho + \tfrac{1}{2}\rho_{i-1}\Delta(v^2) \approx \tfrac{\Delta P}{\gamma-1} + \tfrac{1}{2}\hat{v}\Delta\rho + \tfrac{1}{2}\hat{\rho}\Delta(v^2) \\ &\Delta(v^2) \approx 2\hat{v}\Delta v \end{aligned} \tag{2.83}$$

with

$$\hat{\rho} = \sqrt{\rho_i \rho_{i-1}}. \tag{2.84}$$

Substituting the values from Eq.(2.83) and $\hat{R}^{-1}$ from Eq.(2.82) into Eq.(2.79) yields for the $\alpha^p_{i-1/2}$

$$\alpha^1_{i-1/2} = \frac{\Delta p - \hat{\rho}\hat{c}\Delta v}{2\hat{c}^2} \quad \alpha^2_{i-1/2} = \frac{\Delta\rho\hat{c} - \Delta p}{\hat{c}^2} \quad \alpha^3_{i-1/2} = \frac{\Delta p + \hat{\rho}\hat{c}\Delta v}{2\hat{c}^2}. \tag{2.85}$$

Knowing the values of the $\alpha^p_{i-1/2}$'s the flux at a specific boundary (Eq.2.76) can be calculated and used in Eq.(2.30) to complete the time marching algorithm. The above method applies to one-dimensional systems. However, for the results discussed in this work the Euler equations are solved in two dimensions using plane polar geometry. The extension of the above method to two dimensional systems in plane polar geometry is discussed next.

2.7 Extension to plane geometry and source terms

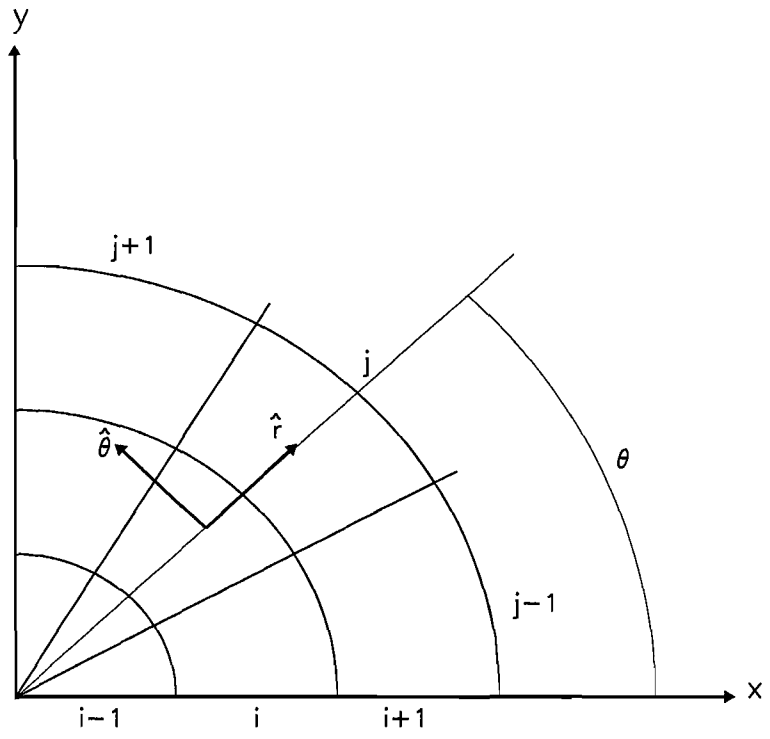

Figure 2.4: The Euler equations are solved in a plane polar grid. $\hat{r}$ denotes a unit vector in the radial direction at an angle θ to the positive x-axis. θ extends over the range $[0, \pi]$. $\hat{\theta}$ denotes a unit vector in the tangential direction.

The extension to plane polar geometry implies that at each cell (shown in Fig.2.4) fluxes in both the radial and tangential directions (the directions being indicated by $\hat{r}$ and $\hat{\theta}$ respectively) may change the magnitude of some quantity in the cell. This implies that Eqs.(2.30) and (2.31) should be rewritten as

$$Q_{ij}^{n+1} = Q_{ij}^{n} - \Delta t \left(\frac{1}{\Delta r_i}(F_{i+1/2,j}^{n} - F_{i-1/2,j}^{n}) + \frac{1}{r_i \Delta \theta_j}(F_{i,j+1/2}^{n} - F_{i,j-1/2}^{n}) \right) \tag{2.86}$$

where

$$F_{i\pm1/2,j}^{n} = \frac{1}{\Delta t} \int_{t_n}^{t_{n+1}} f(q(r_{i\pm1/2}, \theta_j, t))dt \tag{2.87}$$

defines the flux through interface $i \pm 1/2$ in the radial direction at a tangential position j. Similarly

$$F_{i,j\pm1/2}^{n} = \frac{1}{\Delta t} \int_{t_n}^{t_{n+1}} f(q(r_i, \theta_{j\pm1/2}, t))dt \tag{2.88}$$

defines the flux through the $j \pm 1/2$ interfaces at a radial position i. The cell average Q_{ij}^{n+1} is calculated in three steps (see *Kausch*, 1998). An intermediate cell average is calculated according to

$$Q_{ij}^{*n+1} = Q_{ij}^{n} - \Delta t \frac{1}{\Delta r_i}(F_{i+1/2,j}^{n} - F_{i-1/2,j}^{n}). \tag{2.89}$$

The next intermediate state is calculated by incorporating the flux along θ through

$$Q_{ij}^{**n+1} = Q_{ij}^{*n+1} - \Delta t \frac{1}{r_i \Delta \theta_j}(F_{i,j+1/2}^{n} - F_{i,j-1/2}^{n}). \tag{2.90}$$

Lastly any source terms appearing to the right of Eq.(2.2) are taken into account in the third step as

$$Q_{ij}^{n+1} = Q_{ij}^{**n+1} + \Delta t S_{ij}^{n}. \tag{2.91}$$

The first two steps each reduces to solving the Riemann problem for nonlinear systems at each cell interface and the method discussed in sections 2.6 and 2.4 may be used. However, it should be noted that the Euler equations in two or more dimensions are different from the simple one-dimensional case discussed previously. The three dimensional Euler equations for a monatomic, polytropic, ideal gas are given by

$$\frac{\partial \rho}{\partial t} + \nabla \cdot (\rho \mathbf{v}) = 0 \tag{2.92}$$

$$\frac{\partial}{\partial t}(\rho \mathbf{v}) + \nabla \cdot (\rho \mathbf{v} \otimes \mathbf{v}) + \nabla P = 0 \tag{2.93}$$

$$\frac{\partial E}{\partial t} + \nabla \cdot \left(\mathbf{v} \left(\frac{\gamma P}{\gamma - 1} + \frac{1}{2} \rho v^2 \right) \right) = 0 \tag{2.94}$$

where all symbols have the same meanings as before. In plane polar geometry ,however, v is now the velocity vector expressible as the sum of radial and tangential components

$$\mathbf{v} = v_r\hat{r} + v_\theta\hat{\theta}. \tag{2.95}$$

Since the method developed for nonlinear equations assumes that the system consists of scalar quantities being transported along one direction it is necessary to split the system of Euler equations into two parts when plane polar geometry is assumed with each part describing transport along a separate direction. The method developed in the previous section may then be used to calculate solutions along these separate directions respectively.

The flux functions for Eqs.(2.92), (2.93) and (2.94) are described by the terms in parenthesis to the right of the divergence operator. Using Eq.(2.95) the flux functions from Eqs.(2.92) and (2.94) can be easily split into radial and tangential parts. For the flux function in Eq.(2.93) it follows that

$$\rho\mathbf{v}\otimes\mathbf{v} = \begin{bmatrix} \rho v_r^2 & \rho v_r v_\theta \\ \rho v_r v_\theta & \rho v_\theta^2 \end{bmatrix}. \tag{2.96}$$

Eq.(2.96) implies that two quantities are being transported in a particular direction at any one time. These are the momenta ρv_r and ρv_θ. For transport in the radial direction both these quantities are transported at the radial velocity v_r yielding the two radial flux terms ρv_r^2 and $\rho v_\theta v_r$. In the tangential direction these quantities are transported with the tangential velocity v_θ yielding the two tangential fluxes ρv_θ^2 and $\rho v_r v_\theta$. From the above it follows that a natural choice of two flux tensors describing transport along the radial and tangential directions respectively are

$$\vec{F}_r = \begin{bmatrix} \rho v_r \\ \rho v_r^2 + P \\ \rho v_\theta u_r \\ v_r(E+P) \end{bmatrix} \quad \vec{F}_\theta = \begin{bmatrix} \rho v_\theta \\ \rho v_\theta^2 + P \\ \rho v_r v_\theta \\ v_\theta(E+P) \end{bmatrix}. \tag{2.97}$$

Using $\vec{F}_r$ and $\vec{F}_\theta$ for

$$q = \begin{bmatrix} \rho \\ \rho v_r \\ \rho v_\theta \\ E \end{bmatrix} = \begin{bmatrix} q_1 \\ q_2 \\ q_3 \\ q_4 \end{bmatrix} \tag{2.98}$$

the Euler equations are rewritten as

$$\frac{\partial \vec{q}}{\partial t} + \frac{\partial \vec{F}_r}{\partial r} + \frac{1}{r}\frac{\partial \vec{F}_\theta}{\partial \theta} = \vec{S}. \tag{2.99}$$

The form of Eq.(2.99) allows for the separate treatment of transport along the radial and tangential directions. $\vec{S}$ in Eq.(2.99) takes into account geometrical source terms that arises as a consequence of the divergence taken in Eqs.(2.92), (2.93) and (2.94) and writing the subsequent equations in the form of Eq.(2.99). From *Kausch* (1998) the geometrical source term $\vec{S}$ acquired in Eq.(2.99) is given by

$$\vec{S} = -\frac{2v_r + \cot\theta v_\theta}{r}\begin{bmatrix} \rho \\ \rho v_r \\ \rho v_\theta \\ (E+P) \end{bmatrix} + \frac{1}{r}\begin{bmatrix} 0 \\ \rho v_\theta^2 \\ -\rho v_r v_\theta \\ 0 \end{bmatrix}. \tag{2.100}$$

The array element f_{ij} of the flux Jacobian $\vec{F}_r'(q)$ is given by

$$f_{ij} = \frac{\partial F_i}{\partial q_j} \tag{2.101}$$

where F_i is the i'th element of $\vec{F}_r$ and q_j is the j'th element of q. Rewriting $\vec{F}_r$ as

$$\vec{F}_r = \begin{bmatrix} q_2 \\ \frac{q_2^2}{q_1} + P \\ \frac{q_3 q_2}{q_1} \\ \frac{q_2 q_4}{q_1} + \frac{q_2}{q_1}P \end{bmatrix} \tag{2.102}$$

and noting that $\frac{\partial q_i}{\partial q_j} = 0$ if $i \neq j$ $\vec{F}_r'(q)$ is calculated to be

$$\vec{F}_r'(q) = \begin{bmatrix} 0 & 1 & 0 & 0 \\ \frac{\gamma-1}{2}\left(v_r^2 + v_\theta^2\right) - v_r^2 & v_r - (\gamma-2)\,v_r & -(\gamma-1)\,v_\theta & \gamma - 1 \\ -v_\theta v_r & v_\theta & v_r & 0 \\ \frac{\gamma-1}{2}\left(v_r^2 + v_\theta^2\right) v_r - H v_r & H - (\gamma-1)\,v_r^2 & -(\gamma-1) v_r v_\theta & \gamma v_r \end{bmatrix} \tag{2.103}$$

where $P = (\gamma-1)q_4 - \frac{\gamma-1}{2}\frac{q_2^2+q_3^2}{q_1}$ is used. Similarly the flux Jacobian $\vec{F}_\theta'(q)$ is calculated to be

$$\vec{F}_\theta'(q) = \begin{bmatrix} 0 & 0 & 1 & 0 \\ -v_r v_\theta & v_\theta & v_r & 0 \\ \frac{\gamma-1}{2}\left(v_r^2 + v_\theta^2\right) - v_\theta^2 & -(\gamma-1)\,v_r & v_\theta - (\gamma-2)\,v_\theta & \gamma - 1 \\ \frac{\gamma-1}{2}\left(v_r^2 + v_\theta^2\right) v_\theta - H v_\theta & -(\gamma-1)\,v_r v_\theta & H - (\gamma-1)\,v_\theta^2 & \gamma v_\theta \end{bmatrix}. \tag{2.104}$$

From *Kausch* (1998) the eigenvalues of $\vec{F}_r'(q)$ are

$$\lambda^1 = v_r - c \quad \lambda^2 = v_r \quad \lambda^3 = v_r \quad \lambda^4 = v_r + c. \tag{2.105}$$

By substituting v_θ for v_r in the above yields the eigenvalues for $\vec{F}'_\theta(q)$. Subsequently the eigenvectors of $\vec{F}'_r(q)$ are

$$r_r^1 = \begin{bmatrix} 1 \\ v_r - c \\ v_\theta \\ H - v_r c \end{bmatrix} \quad r_r^2 = \begin{bmatrix} 0 \\ 0 \\ 1 \\ v_\theta \end{bmatrix} \quad r_r^3 = \begin{bmatrix} 1 \\ v_r \\ v_\theta \\ \frac{1}{2}\left(v_r^2 + v_\theta^2\right) \end{bmatrix} \quad r_r^4 = \begin{bmatrix} 1 \\ v_r + c \\ v_\theta \\ H + v_r c \end{bmatrix}. \tag{2.106}$$

Similarly the eigenvectors of $\vec{F}'_\theta(q)$ are

$$r_r^1 = \begin{bmatrix} 1 \\ v_r \\ v_\theta + c \\ H - v_\theta c \end{bmatrix} \quad r_r^2 = \begin{bmatrix} 0 \\ 1 \\ 0 \\ v_r \end{bmatrix} \quad r_r^3 = \begin{bmatrix} 1 \\ v_r \\ v_\theta \\ \frac{1}{2}\left(v_r^2 + v_\theta^2\right) \end{bmatrix} \quad r_r^4 = \begin{bmatrix} 1 \\ v_r \\ v_\theta + c \\ H + v_\theta c \end{bmatrix}. \tag{2.107}$$

To diagonalise $\vec{F}'_r(q)$ the inverse of the matrix

$$R = \begin{bmatrix} 1 & 0 & 1 & 1 \\ v_r - c & 0 & v_r & v_r + c \\ v_\theta & 1 & v_\theta & v_\theta \\ H - v_r c & v_\theta & \frac{1}{2}\left(v_r^2 + v_\theta^2\right) & H + v_r c \end{bmatrix} \tag{2.108}$$

is calculated to be

$$R^{-1} = \begin{bmatrix} -\frac{1}{2} + \frac{v_r}{2c} + \frac{(\gamma-1)H}{2c^2} & -\frac{1}{2c} - \frac{(\gamma-1)v_r}{2c^2} & -\frac{(\gamma-1)v_\theta}{2c^2} & \frac{\gamma-1}{2c^2} \\ -v_\theta & 0 & 1 & 0 \\ 2 - \frac{(\gamma-1)H}{c^2} & \frac{(\gamma-1)v_r}{c^2} & \frac{(\gamma-1)v_\theta}{c^2} & -\frac{\gamma-1}{c^2} \\ -\frac{1}{2} - \frac{v_r}{2c} + \frac{(\gamma-1)H}{2c^2} & \frac{1}{2c} - \frac{(\gamma-1)v_r}{2c^2} & -\frac{(\gamma-1)v_\theta}{2c^2} & \frac{\gamma-1}{2c^2} \end{bmatrix}. \tag{2.109}$$

For the three dimensional Euler equations Eq.(2.79) becomes

$$\begin{bmatrix} w_{i,j}^1 - w_{i-1,j}^1 \\ w_{i,j}^2 - w_{i-1,j}^2 \\ w_{i,j}^3 - w_{i-1,j}^3 \\ w_{i,j}^4 - w_{i-1,j}^4 \end{bmatrix} = \begin{bmatrix} \alpha_{i-1/2,j}^1 \\ \alpha_{i-1/2,j}^2 \\ \alpha_{i-1/2,j}^3 \\ \alpha_{i-1/2,j}^4 \end{bmatrix} = \hat{R}^{-1} \begin{bmatrix} \rho_{i,j}^n - \rho_{i-1,j}^n \\ \rho_{i,j}^n v_{r,i,j}^n - \rho_{i-1,j}^n v_{r,i-1,j}^n \\ \rho_{i,j}^n v_{\theta,i,j}^n - \rho_{i-1,j}^n v_{\theta,i-1,j}^n \\ E_{i,j}^n - E_{i-1,j}^n \end{bmatrix} \tag{2.110}$$

where $\hat{R}^{-1}$ denotes R^{-1} where all quantities are replaced by their Roe averages. Substituting $\hat{R}^{-1}$ from Eq.(2.109) into Eq.(2.110) the values for the $\alpha^p_{i-1/2}$'s needed to solve the Riemann problem along the radial direction are obtained as

$$\begin{array}{ll} \alpha^1_{i-1/2,j} = \frac{\Delta P - \hat{\rho}\Delta v_r \hat{c}}{2\hat{c}^2} & \alpha^2_{i-1/2,j} = \hat{\rho}\Delta v_\theta \\ \alpha^3_{i-1/2,j} = \frac{\hat{c}^2\Delta\rho - \Delta P}{\hat{c}^2} & \alpha^4_{i-1/2,j} = \frac{\Delta P + \hat{\rho}\Delta v_r \hat{c}}{2\hat{c}^2}. \end{array} \tag{2.111}$$

By interchanging v_r and v_θ in Eq.(2.111) the values for $\alpha^p_{i,j-1/2}$'s needed to solve the Riemann problem along the tangential direction are obtained. This implies that Eqs.(2.87) and (2.88) can be rewritten analogously to Eq.(2.76) as

$$F^n_{i+1/2,j} = \frac{1}{2}\left[f(Q^n_{i-1,j}) + f(Q^n_{i,j}) - \sum_{p=1}^{4} |\hat{\lambda}^p| \alpha^p_{i-1/2,j} \hat{r}^p_r\right] \tag{2.112}$$

$$F^n_{i,j+1/2} = \frac{1}{2}\left[f(Q^n_{i,j-1}) + f(Q^n_{i,j}) - \sum_{p=1}^{4} |\hat{\lambda}^p| \alpha^p_{i,j-1/2} \hat{r}^p_\theta\right]. \tag{2.113}$$

The method discussed above uses the solution to the Riemann problem together with Roe linearisation to calculate the state of a hydrodyamical system numerically. In the next section it is shown that using Roe linearisation to solve the Riemann problem may lead to a violation of physical entropy conditions. It is shown how this problem can easily be overcome by ensuring that the amount of numerical viscosity implicit to the method never drops below a certain threshold.

2.8 Entropy

From Eq.(2.65) it is seen that in applying Roe linearisation the approximated flux Jacobian $\hat{A}_{i-1/2,j}$ between two cells $C_{i,j}$ and $C_{i-1,j}$ can be expressed as

$$\hat{A}_{i-1/2,j} = \frac{f(Q_{i,j}) - f(Q_{i-1,j})}{Q_{i,j} - Q_{i-1,j}} \tag{2.114}$$

which is also the expression for the speed of a shock (or discontinuity) connecting two states given by $Q_{i,j}$ and $Q_{i-1,j}$ (see *LeVeque*, 2002, p.213). This implies that in using Roe linearisation to approximate the flux at a certain boundary the subsequent solution to the Riemann problem will correspond to a case where all the waves propagating away from a certain interface will be shock-like discontinuities. It can be shown that the true solution to the Riemann problem for the Euler equations always consists of a contact discontinuity and two other waves which may both be shocks, rarefactions or a combination of the two (see *LeVeque*, 2002). All these possibilities define a set of weak solutions to a specific Riemann problem (see *LeVeque*, 2002,

for more details on weak solutions). However, Eq.(2.114) implies that using Roe linearisation to solve the Riemann problem produces a solution in which all the waves travelling away from a certain interface propagate as if they are shocks. Roe linearisation, therefore, automatically leads to using the all-shock weak solution to the Riemann problem, which may violate physical constraints on the entropy of the system.

The entropy s of a fluid is defined as

$$s = c_v \ln\left(\frac{P}{\rho^\gamma}\right) + C \tag{2.115}$$

where c_v is the specific heat at constant volume and C is a constant. In any real hydrodynamic system it is expected that s must be non-decreasing with time. Furthermore, for a fluid that contains no discontinuities it can be shown that the entropy is constant (see *LeVeque*, 2002, p.296). Now consider two fluid states q_l and q_r separated by a single shock wave where

$$\begin{aligned} \rho_l &> \rho_r \\ v_l &< v_r \\ v_l &< c_l \\ v_r &> c_r. \end{aligned} \tag{2.116}$$

Both velocities v_l and v_r are taken to be positive from left to right. c_l and c_r are the sonic velocities associated with the states q_l and q_r respectively. From the assumed state in Eq.(2.116) it can be seen that if the system evolves with time the shock will rarefy the region of higher density to its left. The one-dimensional steady state Rankine-Hugoniot relations (see for example *Holzer and Axford*, 1970) describing mass and momentum conservation across a stationary shock in a polytropic monatomic ideal gas are

$$\begin{aligned} \rho_l v_l &= \rho_r v_r \\ \rho_l v_l^2 + P_l &= \rho_r v_r^2 + P_r. \end{aligned} \tag{2.117}$$

In the rest frame of the shock the Rankine-Hugoniot relations relate the states either side of the shock as

$$\begin{aligned} \frac{\rho_r}{\rho_l} &= \frac{(\gamma+1)M^2}{2+(\gamma-1)M^2} \\ \frac{P_r}{P_l} &= \frac{2\gamma M^2-(\gamma-1)}{\gamma+1} \end{aligned} \tag{2.118}$$

where M is the upstream Mach number.

The shock acts to rarefy the region to its left. In a reference frame in which the shock is not in rest it, therefore, moves into the region to its left 'converting' q_l to q_r in that region. For such a

case it is required that $s_l < s_r$ for the entropy to be non-decreasing with time. Subsequently it must hold for the density and pressure either side of the shock that

$$\frac{P_r}{P_l}\left(\frac{\rho_l}{\rho_r}\right)^{\gamma} \geq 1. \tag{2.119}$$

Using Eq.(2.118) in Eq.(2.119) non-decreasing entropy implies

$$\left(\frac{6+2M^2}{8M^2}\right)^{\frac{5}{3}} \frac{10M^2-2}{8} \geq 1 \tag{2.120}$$

where it was assumed that $\gamma = \frac{5}{3}$. Eq.(2.120) is greater than or equal to one if $M \geq 1$. However, from Eq.(2.116) $\rho_l > \rho_r$. This implies that $M < 1$ in Eq.(2.118) which in turn implies that Eq.(2.120) is less than one, violating the condition that entropy must be non-decreasing. The true solution to the Riemann problem described by the state in Eq.(2.116) corresponds to a transonic rarefaction. In using Roe linearisation this rarefaction is approximated as a shock which leads to the entropy condition being violated.

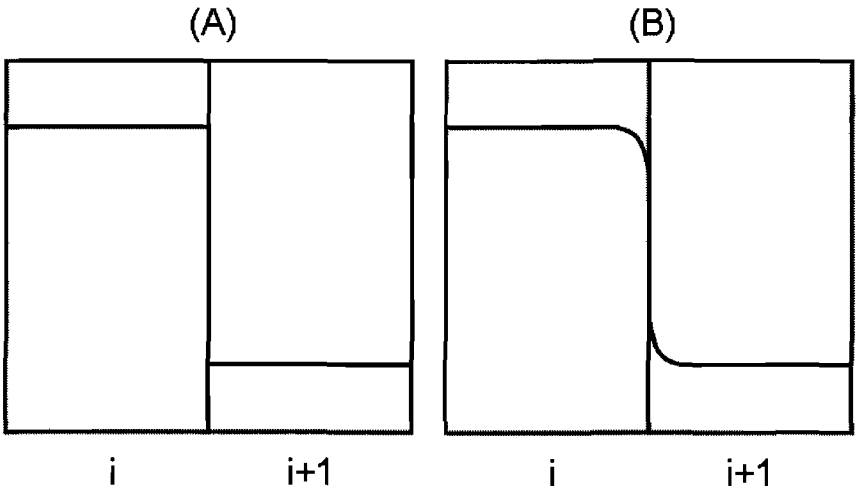

Figure 2.5: Piecewise constant data (A) and smoothed out data (B).

The violation of the entropy condition can be solved by recalling that for smooth flows the entropy is constant in time and, therefore, the entropy condition is automatically satisfied. Assume that the interface at $i+\frac{1}{2}$ in Fig.(2.5) is at x. The Taylor expansion of some general flux $f(q)$ about a point just to the left of x (say $x-\delta x$) is

$$f(q(x,t)) = f(q(x-\delta x,t)) + f'(q(x-\delta x,t))(q(x,t)-q(x-\delta x)) + ... \tag{2.121}$$

so that

$$f(q(x,t)) \approx f(q(x-\delta x,t)) + f'(q(x-\delta x,t))(q(x,t)-q(x-\delta x,t)). \tag{2.122}$$

Similarly at a point $x + \delta x$ the flux $f(q)$ may be approximated as

$$f(q(x,t)) \approx f(q(x+\delta x,t)) + f'(q(x+\delta x,t))(q(x,t) - q(x+\delta x,t)). \tag{2.123}$$

Using Eqs.(2.122 and 2.123) yields

$$f(q) \approx \frac{1}{2}(f(x+\delta x) + f(x-\delta x)) + \frac{1}{2}(f'(x+\delta x)(q(x) - q(x+\delta x)) + f'(x-\delta x)(q(x) - q(x-\delta x))) \tag{2.124}$$

Regarding the piecewise constant case (illustrated in the panel labelled (A) in Fig.2.5), for $\Delta x >> \delta x > 0$ (where Δx is the cell dimension) the terms containing the first derivatives in Eq.(2.124) are exactly zero and the approximated flux is just the average of the fluxes to the left and right of the cell interface. Regarding the smooth data (illustrated in the panel labelled (B) in Fig.2.5), if $\Delta x >> \delta x > 0$ arbitrarily close to x the terms containing first derivatives are non-zero. Alternatively it follows that for a flux $f(q(r,\theta,t))$ the average flux (in the radial direction denoted by the i indexes) at the interface between cells $C_{i,j}$ and $C_{i+1,j}$ is given by

$$\bar{f}(q) = \frac{1}{2}(f(Q_{i,j}) + f(Q_{i+1,j})) \tag{2.125}$$

where $Q_{i,j}$ indicates a cell averaged quantity. If $\bar{f}(q)$ is modified by a correction term $\eta(r,\theta)$ so that

$$\bar{f}'(q) = \frac{1}{2}(f'(Q_{i,j}) + f(Q_{i+1,j})) + \eta(r,\theta), \tag{2.126}$$

it can be seen from Eq.(2.124) that $\bar{f}(q)$ now describes the flux for the smoothed out case (illustrated in panel (B) in Fig.2.5) approximating the piecewise constant case shown in panel (A) of Fig.(2.5). Comparison between Eqs.(2.39) and (2.126) show that Eqs.(2.39) is just the average flux between two cells with the summation term having the same effect as $\eta(r,\theta)$ in Eq.(2.126). Therefore, Eq.(2.39) describes the approximated flux for 'smoothed out' data, which in turn approximates the piecewise constant data to the left and right of some cell interface. Since Eq.(2.39) approximates the flux for smoothed out data it will automatically satisfy the entropy condition provided that the summation term never falls below a certain threshold.

This is achieved by modifying the Roe averaged eigenvalues $\lambda^p_{i+1/2,j}$ according to the ansatz of Leer et al. (see *Kausch*, 1998, for reference).

A threshold is defined as

$$\Delta = 4\left(\lambda^p_{i+1,j} - \lambda^p_{i,j}\right). \tag{2.127}$$

If $\lambda^p_{i+1,j} > \lambda^p_{i,j}$ the Roe averaged eigenvalues $\hat{\lambda}^p_{i+1/2,j}$ are replaced by modified values $\hat{\lambda}^{p,*}_{i+1/2,j}$ which are calculated as

$$\hat{\lambda}^{p,*}_{i+1/2,j} = \begin{cases} \frac{\left(\hat{\lambda}^p_{i+1/2,j}\right)^2}{\Delta} + \frac{\Delta}{4} & \text{for} \quad |\hat{\lambda}^p_{i+1/2,j}| < \frac{\Delta}{2} \\ \hat{\lambda}^p_{i+1/2,j} & \text{otherwise.} \end{cases} \tag{2.128}$$

Using Eq.(2.128) ensures that the method of Roe linearisation produces solutions to the Riemann problem at any interface that will always satisfy physical entropy constraints. However, Roe linearisation may lead to other non-physical solutions such as states leading to negative densities or pressures. To ensure that this does not happen an alternative solution to the Riemann problem is presented in the next section which ensures positive densities and pressures.

2.9 The HLLE-solver

Recall from Fig.(2.2) that for two initial states q_l and q_r that cannot be connected by a single discontinuity an intermediate state forms as the system evolves with time. This intermediate state is described by the point of intersection in phase space between lines parallel to the eigenvectors r^1 and r^2 respectively. Fig.(2.2) shows the case for a linear system. Since the eigenvectors r^1 and r^2 do not depend on the local value of q their orientation in phase space is the same at every point in phase space. For nonlinear systems, however, the eigenvectors do depend on the local state of q and subsequently the orientation of a specific eigenvector changes through phase space depending on the state of q at a specific point in phase space. Where the loci parallel to the eigenvectors are straight lines in the linear case, these loci now become curves in the nonlinear case as shown by the dashed lines in Fig.(2.6).

Fig.(2.6) shows the case for two states q_l and q_r in phase space for a system governed by the Euler equations where it is assumed that q_l and q_r have the same energy. Analogous to the discussion in section 2.3 it can be seen that as the system evolves in time an intermediate state q'_m forms between q_l and q_r at the intersection of the loci parallel to the eigenvectors r^1 and r^2. For the nonlinear case shown in Fig.(2.6) these loci are now curves (as shown by the dashed lines) with the property that at any point on the curve the curve is parallel to the eigenvector defined at that point (as indicated by the short arrows in Fig.2.6).

Recall from section 2.6 that the Roe averaged flux Jacobian $\hat{A}_{i-1/2}$ is obtained by integrating along a path in phase space (connecting q_l and q_r) traced out as ξ in Eq.(2.58) varies between 0 and 1. Since the trajectory is linear in ξ Roe averaging, therefore, approximates the transition between q_l and q_r by calculating an intermediate state q_m at the intersection of two straight lines from q_l and q_r parallel to the Roe averaged eigenvectors defined in terms of q_l and q_r as shown by the dotted lines in Fig.(2.6). As shown in Fig.(2.6) this may lead to unphysical solutions as the state q_m at the intersection of the dotted lines corresponds to a state with negative density.

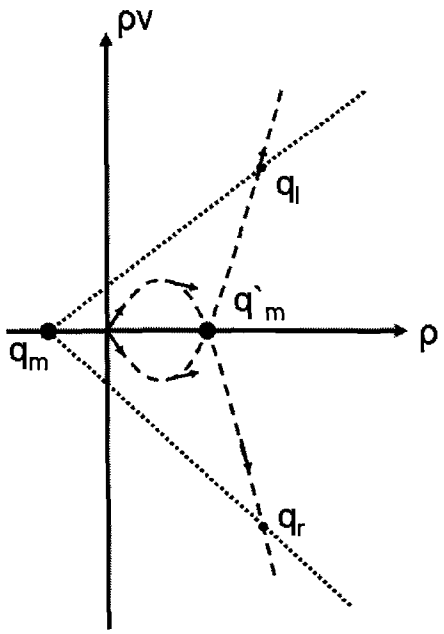

Figure 2.6: The Hugoniot loci (dashed curves) in phase space through two initial states q_l and q_r. At a point in phase space on the Hugoniot locus associated with eigenvector r^1 the eigenvector r^1 is parallel to the locus at that point. In the exact solution to the Riemann problem between q_l and q_r an intermediate state q'_m is formed at the intersection of the Hugoniot loci. In using Roe averages to obtain an approximate solution an intermediate state q_m is calculated at the intersection of two straight lines shown by the dotted lines, each parallel to a Roe averaged eigenvector defined in terms of q_l and q_r. This may lead to unphysical results such as negative densities and pressures characterising the state q_m.

This problem is overcome by using an alternative solution to the Riemann problem where negative density and pressure values are expected to occur. For such a case the flux at the interface (say at $i+1/2, j$) between two cells is replaced an alternative flux (from *Kausch*, 1998)

$$F^{HLLE}_{i+1/2} = \frac{b^+_{i+1/2} f(Q^n_i) - b^-_{i+1/2} f(Q^n_{i+1})}{b^+_{i+1/2} + b^-_{i+1/2}} + \frac{b^+_{i+1/2} b^-_{i+1/2} (Q_{i+1} - Q_i)}{b^+_{i+1/2} + b^-_{i+1/2}} \tag{2.129}$$

where the j subscript is dropped. $b^{\pm}_{i+1/2}$ is calculated as

$$b^-_{i+1/2} = \min(b^l_{i+1/2}, 0) \quad \text{and} \quad b^+_{i+1/2} = \max(b^r_{i+1/2}, 0) \tag{2.130}$$

where

$$b^l_{i+1/2} = \min(\hat{\lambda}^1_{i+1/2}, v_{r,i} - c_i) \quad \text{and} \quad b^r_{i+1/2} = \max(\hat{\lambda}^4_{i+1/2}, v_{r,i+1} + c_{i+1}) \tag{2.131}$$

with

$$\hat{\lambda}^1_{i+1/2} = \hat{v}_r - \hat{c} \quad \text{and} \quad \hat{\lambda}^4_{i+1/2} = \hat{v}_r + \hat{c}. \tag{2.132}$$

In Eq.(2.132) $\hat{v}_r$ and $\hat{c}$ are defined according to the Roe averaging formulas in section 2.6. $f(Q_i^n)$ in Eq.(2.129) is given in terms of the cell averaged density ρ_i,cell averaged radial and tangential momenta ($\rho_i v_{r,i}$ and $\rho_i v_{\theta,i}$) and cell averaged energy E_i (where the n superscript is neglected as in section 2.6) as

$$f(Q_i^n) = \begin{bmatrix} \rho_i v_{r,i} \\ \rho_i v_{r,i}^2 + P_i \\ \rho_i v_{\theta,i} v_{r,i} \\ v_{r,i}(E_i + P_i) \end{bmatrix} \tag{2.133}$$

The numerical method using either the Roe or HLLE solutions to the Riemann problem is only first order accurate, as can be seen from the cell averaging in Eq.(2.25). Furthermore, the entropy fix from section 2.8 ensures that a certain amount of non-vanishing artificial viscosity is always present in the system which leads to increased dissipative effects. Since the Euler-equations are non-dissipative excessive 'numerical dissipation' may lead to poor results. This problem is overcome by using a higher order method discussed in the next section.

2.10 Higher order corrections

The cell-averaging procedure in Eq.(2.25) implies that a certain quantity $q(x,t)$ is approximated to be constant within a certain volume Δx (over a certain time step Δt) and is, therefore, the lowest order approximation that can be made. The advantage of such a lowest order approximation is that no assumptions regarding the continuity of $q(x,t)$ within the volume Δx is made. Alternatively if it is assumed that $q(x,t)$ is continuous over a certain range Δx, a Taylor expansion of $q(x,t)$ can be made around a certain point and any number of higher order terms can be used in the approximation. Therefore, for some initial state q_0 it is preferable to use a higher order approximation for regions in which q_0 is smooth while the first order accurate method from Eq.(2.25) is retained close to discontinuities.

In the context of the method described in section 2.6 this implies that higher order terms are taken into account in the calculation of the flux at a certain interface if the data is approximately smooth, while the first order accurate method is used if the data is approximately discontinuous. This is done by using the function (see *Kausch*, 1998, for reference)

$$\Phi(x,y) = \frac{(x^2+\epsilon^2)y + (y^2+\epsilon^2)x}{x^2+y^2+2\epsilon^2} \tag{2.134}$$

where ϵ is a small number. Usually $\epsilon \approx 0$ (depending on the problem considered). $\Phi(x,y)$ has the properties that for $xy > 0$

$$\begin{aligned} \Phi &\simeq y \quad \text{if} \quad x >> y \\ \Phi &\simeq x \quad \text{if} \quad y >> x \\ \Phi &\simeq \tfrac{1}{2}(x+y) \quad \text{if} \quad x \simeq y. \end{aligned} \tag{2.135}$$

Assume that the cell averaged quantities $Q^n_{i-1,j} \simeq Q^n_{i,j} \simeq Q^n_{i+1,j}$. The gradients in the radial direction (associated with the i indexes) at the cell interfaces $i \pm 1/2$ are approximated as

$$\left.\frac{\partial q}{\partial r}\right|_{i-1/2} \simeq \frac{Q^n_{i,j} - Q^n_{i-1,j}}{r_{i,j} - r_{i-1,j}} \tag{2.136}$$

$$\left.\frac{\partial q}{\partial r}\right|_{i+1/2} \simeq \frac{Q^n_{i+1,j} - Q^n_{i,j}}{r_{i+1,j} - r_{i,j}} \tag{2.137}$$

where $r_{i,j}$ is the radial position associated with the centre of cell $C_{i,j}$. The cell averages to the left and right of the interface at $i + 1/2$ are now adjusted according to

$$Q^n_{i+1/2,j,L} = Q^n_{i,j} - \frac{1}{2}\Phi\left(\frac{Q^n_{i,j} - Q^n_{i-1,j}}{r_{i,j} - r_{i-1,j}}, \frac{Q^n_{i+1,j} - Q^n_{i,j}}{r_{i+1,j} - r_{i,j}}\right)\Delta r. \tag{2.138}$$

$$Q^n_{i+1/2,j,R} = Q^n_{i,j} + \frac{1}{2}\Phi\left(\frac{Q^n_{i,j} - Q^n_{i-1,j}}{r_{i,j} - r_{i-1,j}}, \frac{Q^n_{i+1,j} - Q^n_{i,j}}{r_{i+1,j} - r_{i,j}}\right)\Delta r \tag{2.139}$$

where Δr is the radial cell dimension. If either of the approximated gradients in Eqs.(2.136) and (2.137) are large (as would be expected close to a discontinuity) it can be seen from Eq.(2.135) that Φ will approach the value of the smaller approximate gradient (if both approximate gradients have the same sign). This in turn leads to

$$Q^n_{i+1/2,j,L} \simeq Q^n_{i,j} \quad \text{and} \quad Q^n_{i+1/2,j,R} \simeq Q^n_{i+1,j} \tag{2.140}$$

yielding a first order accurate approximation. Similarly if both approximate gradients in Eqs.(2.136) and (2.137) are of the same order but with opposite signs Eq.(2.141) is again obtained. If Eqs.(2.136) and (2.137) yield approximate gradients of the same order and sign it implies that the data are approximately continuous over the interface at $i + 1/2$. From Eq.(2.135) a second order accurate approximation is now obtained as

$$Q^n_{i+1/2,j,L} \simeq Q^n_{i,j} - \tfrac{1}{2}\frac{\partial \overline{Q}^n_{i,j}}{\partial r}\Delta r \quad \text{and} \quad Q^n_{i+1/2,j,R} \simeq Q^n_{i+1,j} + \tfrac{1}{2}\frac{\partial \overline{Q}^n_{i,j}}{\partial r}\Delta r \tag{2.141}$$

where

$$\frac{\partial \overline{Q}^n_{i,j}}{\partial r} = \frac{1}{2}\left(\frac{Q^n_{i+1,j} - Q^n_{i,j}}{r_{i+1,j} - r_{i,j}} + \frac{Q^n_{i,j} - Q^n_{i-1,j}}{r_{i,j} - r_{i-1,j}}\right) \tag{2.142}$$

is the approximated cell averaged radial gradient of cell $C_{i,j}$.

2.11 Summary

Using the solution to the one-dimensional advection equation a numerical method for solving the multi-dimensional Euler-equations (Eqs.2.92,2.93 and 2.94) can be obtained. This method depends on subdividing the initial state of a specific problem into finite volumes and approximating the state of the system within each volume as an average calculated over the extent of that volume. The system can now be approximated as a constant coefficient linear hyperbolic system. This is done by rewriting the Euler-equations as a quasi-linear system (Eq.2.52) and linearising the resulting flux Jacobian at the border of each volume (each cell interface). Since an m-dimensional constant coefficient linear hyperbolic system can be described in terms of m independent advection equations the properties of the advection equation can now be used to solve the Euler-equations numerically by providing fluxes at each cell interface which affects the averaged quantity within each volume (cell).

The method described in this chapter is now applied to the specific problem of the solar wind (SW) and local interstellar medium (LISM) interaction. The SW-LISM interaction problem is the topic of the next (and subsequent) chapters.

Chapter 3

The heliosphere I

3.1 Introduction

The immediate interstellar volume around the Sun is not empty. Instead the Sun is immersed in a cloud cluster called the cluster of local interstellar clouds (CLIC). The CLIC consists of several cloudlets. The Sun is currently moving through one such cloudlet called the local interstellar cloud (LIC). The CLIC itself is immersed in a low density region (on the scale of $\sim$ 100 pc) called the Local Bubble (see *Frisch and Slavin*, 2006; *Frisch*, 2007; *Slavin and Frisch*, 2007). In the heliocentric rest frame the motion between the Sun and LIC can be modelled as an interstellar wind (LIC particles) 'blowing over' the heliocentric system. In this work the interstellar wind will be referred to as the local interstellar medium (LISM).

The Sun also adds particles to the heliocentric system. These particles, known as the solar wind (SW), originate in the solar corona and propagate away from the Sun into interplanetary space. At some distance away from the Sun the SW and LISM interact with each other. Following *Baranov and Malama* (1993); *Pauls et al.* (1995); *Pogorelov* (1995); *Pauls and Zank* (1996); *Zank et al.* (1996); *Izmodenov* (1997); *Pauls and Zank* (1997); *Pogorelov and Semenov* (1997); *Kausch* (1998); *Zank* (1999) and *Fahr et al.* (2000) it will be assumed that this interaction can be described (at least in part) hydrodynamically implying that the SW-LISM interaction can be described as a relaxation towards a steady state connecting two distinct fluids. This implies that as the SW-LISM interaction reaches a steady state, standing waves form which separates regions with different flow characteristics. These standing waves give rise to a structure called the heliosphere.

Understanding the heliosphere is important considering that it affects particle intensities (such as cosmic rays) at Earth through various means, broadly called the modulation of cosmic rays (CR's). Modulation of CR's depends on, among other things, the position and geometry of two interfaces called the termination shock (TS) and heliopause (HP) (see *Ferreira et al.*, 2004a; *Potgieter and Langner*, 2004; *Langner and Potgieter*, 2005; *Potgieter and Langner*, 2005) which form as a consequence of the SW-LISM interaction relaxing towards pressure equilibrium. Historically the HP serves as a modulation boundary, implying that the heliospheric modulation of

galactic cosmic rays is confined to the region between the Sun and HP. In a steady state, the TS is a stationary shock at which the SW undergoes a transition from a supersonic to a subsonic flow. It is, therefore, essential to understand the heliosphere in order to understand the greater cosmic medium outside the immediate solar vicinity. Understanding the heliosphere as it is affected by different processes inherent to the SW and LISM is the focus of this and the next chapter.

In this chapter it will be assumed that the SW and LISM contain only protons. The proton interaction between the SW and LISM is the dominant effect in establishing the characteristic structure of the heliosphere and provides a useful foundation from which to analyse the basic properties of the heliosphere. In the next chapter the mutual effects of other particle species on the heliosphere will be discussed and compared to the 'protons only' case presented here in order to illuminate the effect these other particle species have on the heliospheric structure.

In this chapter the numerical formalism described in the previous chapter will be used as a foundation to analyse the formation of the heliosphere and its subsequent geometry in a steady state. However, for this to be possible the state of the two mediums causing the formation of the heliosphere (namely the SW and LISM) needs to be established since the state of the SW (close to the Sun) and the LISM (at large heliocentric distances) provide the necessary boundary conditions from which the SW-LISM interaction is calculated. A brief review of the state and composition of the SW and LISM follows after which the formation of the heliosphere and its subsequent characteristics in a steady state will be examined for the 'protons only' case.

3.2 The solar wind and local interstellar medium

The realisation that the SW exists can be traced back to the study of ionic comet tails as comets come close to the Sun. *Biermann* (1951, 1957) suggested that the orientation of these tails is due to the interaction with 'solar corpuscular radiation'. Building on this initial work, *Parker* (1958) investigated the dynamics of the solar corona (the solar atmosphere) and concluded that it was impossible for the corona to be in hydrostatic equilibrium with the surrounding interstellar matter. Rather particles are continuously escaping from the corona into interplanetary space. These particles came to be known as the SW.

Observations of the SW have been made by several spacecraft and of special use are those observations from the Ulysses spacecraft because it provides SW observations over a range of solar latitudes as shown in Fig.(3.1). Implicit to describing the SW in terms of a bulk velocity magnitude v, density n and temperature T is the assumption that the SW may be treated hydrodynamically. This implies that the SW velocity distribution is Maxwellian. Observations of the SW velocity distribution verifies this assumption for the bulk of the SW particles, although the presence of a high energy tail in the SW velocity distribution may be dynamically important (see *Gloeckler et al.*, 1992; *Fisk and Gloeckler*, 2006).

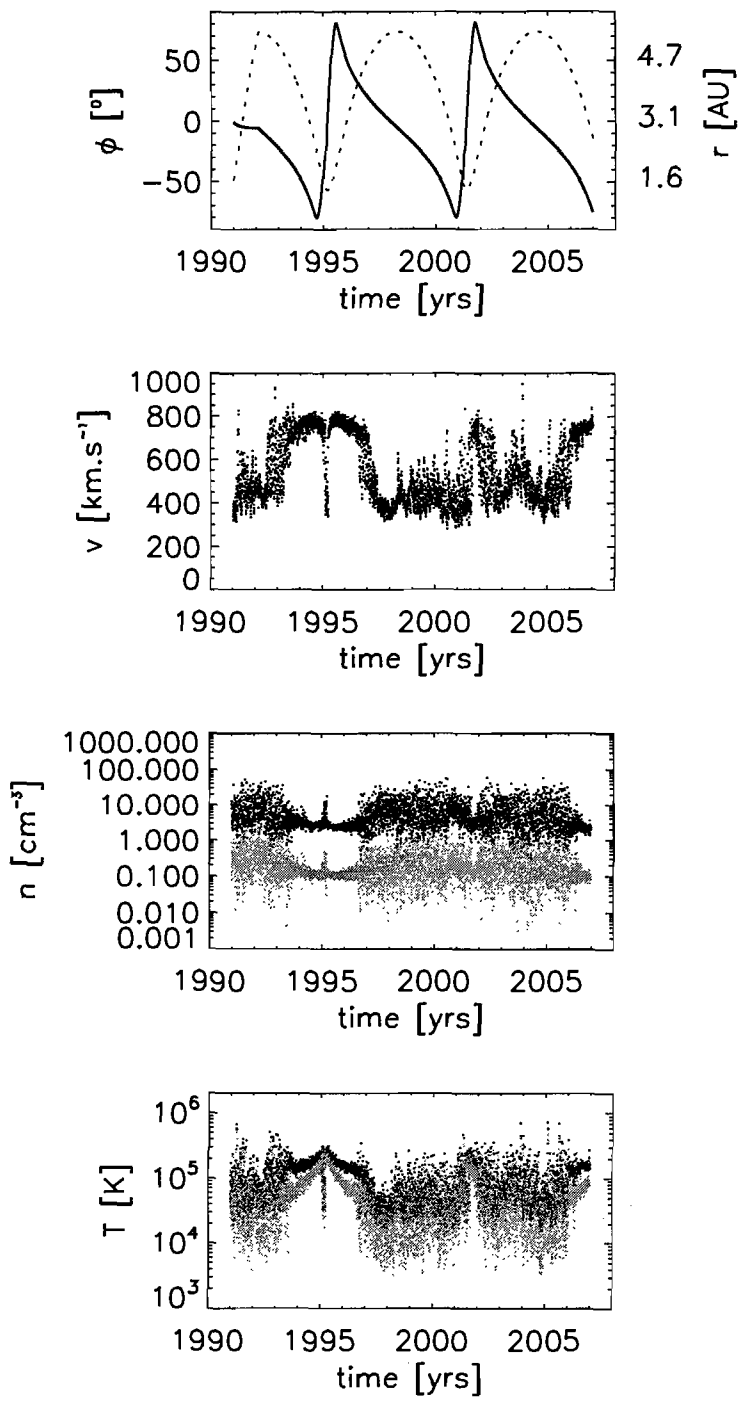

Figure 3.1: The heliocentric radial (r, dotted line) and latitudinal (ϕ, solid black line) position of the Ulysses spacecraft with time (top panel) and the corresponding observed values of the SW velocity v (second panel from top) , density n (third panel from top) and temperature T (bottom panel). Shown in the third panel from the top is the SW proton density (black data points) together with the alpha particle (He^{2+}) density (grey data points). The density is normalized to 1 AU by assuming $n \propto r^{-2}$. The bottom showing the SW temperature has two data sets (black and grey) describing the SW temperature. Data provided courtesy of http://cohoweb.gsfc.nasa.gov. See this website for further details regarding the difference between the two temperature data sets.

From Fig.(3.1) the SW properties can be summarized as follows: the SW consists mainly of protons and alpha particles (He^{2+}). Trace amounts of heavier ions are also present (see *Gloeckler et al.*, 1992). At low latitudes the SW is a slow, dense plasma stream (called the slow SW) characterised by a bulk velocity and proton density in the range of $300 - 450$ km.s^{-1} and $2.5 - 7.5$ cm^{-3} (here and in the rest of this work cm^{-3} implies particles per cubic centimetre). The temperature is of the order of 10^5 K.

The SW is affected by a 11-year solar cycle in which solar activity, characterised by sunspots and solar magnetic field activity (see for example the introduction by *Ngobeni*, 2006), periodically changes from minimal activity to a period in which solar activity is greatly increased, and back again. Periods in which the Sun exhibits the least activity are called solar minimum periods while periods during which the Sun is most active are referred to as solar maximum periods. At higher latitudes during solar minimum conditions the SW is characterised by high velocities and low densities. This plasma stream is referred to as the fast SW, and characterised by a bulk velocity in the range of $750 - 800$ km.s^{-1} and a proton density close to 2.5 cm^{-3}. The fast SW disappears as solar activity progresses to solar maximum. During solar maximum the SW exhibits (to a good approximation) the characteristics of the slow SW over all latitudes.

The parameters describing the LISM are less well constrained since no direct measurement of LISM properties is currently possible. All known properties of the LISM, therefore, need to be inferred either from line of sight measurements over several parsecs or by using local measurements in conjunction with a theoretical understanding of the processes that might attenuate whatever property is being measured and thereby compensate for them.

A method illustrating the latter is the use of particle properties from anomalous cosmic rays (ACR's) and pick-up ions (PUI's). A certain amount of neutral particles can propagate into the heliosphere unhindered. Some of these neutrals are ionized and 'picked up' by the ionized solar wind (hence the name 'pick-up' ions). See *Holzer* (1989); *Zank* (1999) and *Fichtner* (2001) for comprehensive reviews on the interaction between protons, hydrogen and subsequently pick-up ions in the SW and LISM. At the TS these PUI's are accelerated to higher energies to form the anomalous component observed in the cosmic ray energy spectrum (see for example *Fisk et al.*, 1974; *Dworsky and Fahr*, 2000; *Fichtner*, 2001; *Scherer and Ferreira*, 2005; *Ferreira and Scherer*, 2006). Therefore, the characteristics of ACR's and PUI's are tied up with the abundance of neutral atoms and the ionization state of the LISM and can be used to infer the properties of these regions.

Line of sight measurements provide a more direct way of calculating characteristics like particle abundances, temperature and ionization fractions but also require a lot of assumptions to be made as to what is happening in a region of space usually extending over several parsecs. Furthermore, since line of sight observations supply information integrated along a certain path it is useful to obtain average values over large distances but insufficient when information about matter directly outside the heliosphere (within a couple of hundred AU) is needed.

Using observations of backscattered radiation from neutral Helium in the outer heliosphere together with direct measurements of inflowing He atoms and PUI data *Frisch* (1998) calculates the relative velocity (in a heliocentric frame of reference) between the Sun and the LISM to be $\sim$ 26 km.s^{-1}. Although these measurements are all taken inside the heliosphere they show good correlation between values inferred from line of sight measurements to nearby stars yielding a relative velocity of the same magnitude. This value also corresponds to values found by *Piskunov et al.* (1997) and more recently *Möbius et al.* (2004) who used a range of spacecraft data to establish a mean value of 26.24 ± 0.45 km.s^{-1}. Most recently *Müller et al.* (2006) and *Slavin and Frisch* (2007) established the magnitude of the relative velocity between the Sun and LISM as 28.1 ± 4.6 km.s^{-1}.

Using the line-of-sight approach *Anderson et al.* (1978) inferred a mean neutral hydrogen density $n_H \simeq 0.1$ cm^{-3} by investigating the Lynman-α emission line of cooler type stars within about 10 parsecs of the Sun. Recent discussions (see *Müller et al.*, 2006; *Slavin and Frisch*, 2007) propose a neutral hydrogen density immediately outside the heliosphere of $0.19 - 0.21$ cm^{-3}. *Gry and Jenkins* (2001), following the line-of-sight approach, found that the neutral hydrogen density of the LISM is approximately 0.1 cm^{-3}. Using a model based on cosmic ray transport and comparing the model results with Voyager and Wind spacecraft data, *Cummings et al.* (2002) calculated the neutral hydrogen density to be 0.097 ± 0.015 cm^{-3}. A lower bound on the neutral density was calculated by *Chassefiere et al.* (1986) who found the neutral hydrogen density at large heliocentric distances to be $n_H = 0.051 \pm 0.017$ cm^{-3}.

The results from *Chassefiere et al.* (1986) depend on observations made by the Venera 11 and 12 spacecraft which are processed by taking into account several variables altering the particle counts picked up by instruments on these two spacecraft. By assuming that not all the neutrals converging on the heliosphere pass into it, the conclusion is reached that the total hydrogen density outside the heliosphere is $0.05 - 0.15$ cm^{-3}. Taking all these results into consideration a realistic range for the hydrogen density in the LISM is $0.05 - 0.20$ cm^{-3}.

From radiative transfer models (see *Müller et al.*, 2006; *Slavin and Frisch*, 2007) it is suggested that the proton density at the heliospheric boundary is $\sim$ 0.1 cm^{-3}. This is consistent with earlier estimates (see *Frisch*, 1994) that the LISM has particle densities of the order of ~ 0.1 cm^{-3} and that neutral hydrogen and proton densities are of the same order in the LISM. Therefore, it will be assumed that the proton density in the LISM has the same possible range as the hydrogen density mentioned above.

The temperature of the LISM can be calculated from the width of Lynman-α line spectra. This is done by *Gry and Jenkins* (2001) who find the LISM temperature to be between 5700 K and 8200 K. This corresponds to work done by previous authors (see *Chassefiere et al.*, 1986; *Frisch*, 1994; *Piskunov et al.*, 1997; *Frisch*, 1998) where the temperature was found to be essentially in the same range with the exception of *Chassefiere et al.* (1986) establishing the upper limit of the temperature at 9000 K.

Parameter	Value
SW proton density (low latitudes) $n_{p,SW}$	$2.5 - 7.5$ cm^{-3}
SW proton velocity (low latitudes) $v_{p,SW}$	$300 - 450$ km.s^{-1}
SW proton temperature (all latitudes) $T_{p,SW}$	$\sim 1 \times 10^5$ K
LISM proton density $n_{p,LISM}$	$0.05 - 0.20$ cm^{-3}
LISM hydrogen density $n_{H,LISM}$	$0.05 - 0.20$ cm^{-3}
LISM proton velocity $v_{p,LISM}$	$23 - 33$ km.s^{-1}
LISM hydrogen velocity $v_{H,LISM}$	$23 - 33$ km.s^{-1}
LISM proton temperature $T_{p,LISM}$	$5000 - 9000$ K
LISM hydrogen temperature $T_{H,LISM}$	$5000 - 9000$ K

Table 3.1: Possible ranges in parameters describing the bulk SW and LISM states.

In the rest of this work it will be assumed that the LISM state is the same in all directions and constant on timescales relevant to the results presented. For the rest of this chapter it will be assumed that the LISM protons may be treated hydrodynamically. This assumption forms the basis of most numerical models describing the SW-LISM interaction (see *Baranov and Malama*, 1993; *Pauls et al.*, 1995; *Pogorelov*, 1995; *Pauls and Zank*, 1996; *Zank et al.*, 1996; *Izmodenov*, 1997; *Pogorelov and Semenov*, 1997; *Pauls and Zank*, 1997; *Kausch*, 1998; *Zank*, 1999; *Fahr et al.*, 2000). It needs to be noted though that as soon as the SW-LISM interaction is extended to include other particles (such as neutral hydrogen and PUI's) subtle differences exist between the pure hydrodynamic approach where all particle species are modelled hydrodynamically (see *Fahr et al.*, 2000) and where additional particle species are treated kinetically (see *Baranov and Malama*, 1993).

To summarise, possible ranges in different SW and LISM parameters are taken from the above mentioned results and shown in Table 3.1. In a later section a parameter study is presented which gauges the sensitivity of the SW-LISM interaction to different assumed SW and LISM states (within the ranges noted in Table 3.1) at the respective boundaries close to the Sun and at large heliocentric distances.

3.3 The formation of the heliosphere in one dimension

In order to examine the formation of the heliosphere the following assumptions are made regarding the SW-LISM interaction: the interaction is limited to one dimension corresponding to a radial path assumed to be anti-parallel to the inflow direction of the LISM in a heliocentric frame of reference. Both the SW and LISM are assumed to consist of protons alone. These assumptions represent the simplest possible case of the SW-LISM interaction (more complex descriptions of the SW-LISM interaction will be discussed in later sections) but are useful in determining the expected structure of the heliosphere. In order to set up an initial state the SW is allowed to expand radially and adiabatically away from the Sun until it encounters the LISM at some distance r_d. Adiabatic expansion implies that

$$PV^{\gamma} = constant \tag{3.1}$$

where γ is the ratio of specific heats defined in Eq.(2.48) and that the expansion is isentropic. Here V denotes volume. From the definition of entropy s in Eq.(2.115) it follows that the pressure P can be expressed in terms of the density ρ as

$$P = C_s \rho^{\gamma} \tag{3.2}$$

where is C_s is constant since the expansion is isentropic. This implies that Eq.(3.1) may be expressed as

$$\rho V = constant. \tag{3.3}$$

Note that the density ρ may also be expressed in terms of the number density n as $\rho = mn$ where m is the mass of a single particle. Imagine that some density ρ_1 is associated with thin, spherical shell like volume dV_1 with thickness dr where

$$dV_1 = 4\pi r_1^2 dr. \tag{3.4}$$

If the system expands adiabatically at some later time the density ρ_2 will be associated with the volume dV_2 given by

$$dV_2 = 4\pi r_2^2 dr. \tag{3.5}$$

From Eq.(3.3) it follows that

$$\rho_2 = \frac{\rho_1 r_1^2}{r_2^2} \tag{3.6}$$

which implies that for an adiabatic expansion $\rho \propto r^{-2}$. From the conservation of mass equation

$$\frac{\partial \rho}{\partial t} + \nabla \cdot (\rho \mathbf{v}) = 0 \tag{3.7}$$

it follows for a steady state that

$$v \frac{\partial \rho}{\partial r} + \frac{\rho}{r^2} \frac{\partial}{\partial r} \left(r^2 v \right) = 0 \tag{3.8}$$

where v is the radial component of the velocity $\mathbf{v}$ since the analyses is restricted to one (radial) dimension. For $\rho \propto r^{-2}$ it follows that v is constant. Lastly from Eq.(3.2) it follows that $P \propto r^{-10/3}$ for an adiabatic expansion with $\gamma = 5/3$.

Using these relations the initial condition for the SW-LISM interaction is calculated, as shown in the top panel of Fig.(3.2). The initial condition consists of a discontinuous interface between the undisturbed LISM (flowing in from 400 AU towards the point at 0 AU in Fig.3.2) and the outward flowing SW (flowing away from the point at 0 AU in Fig.3.2). Arbitrarily close to this discontinuity the initial condition may be viewed as a single Riemann problem for the system of Euler equations, the solution of which is calculated using the discussion from section 2.6.

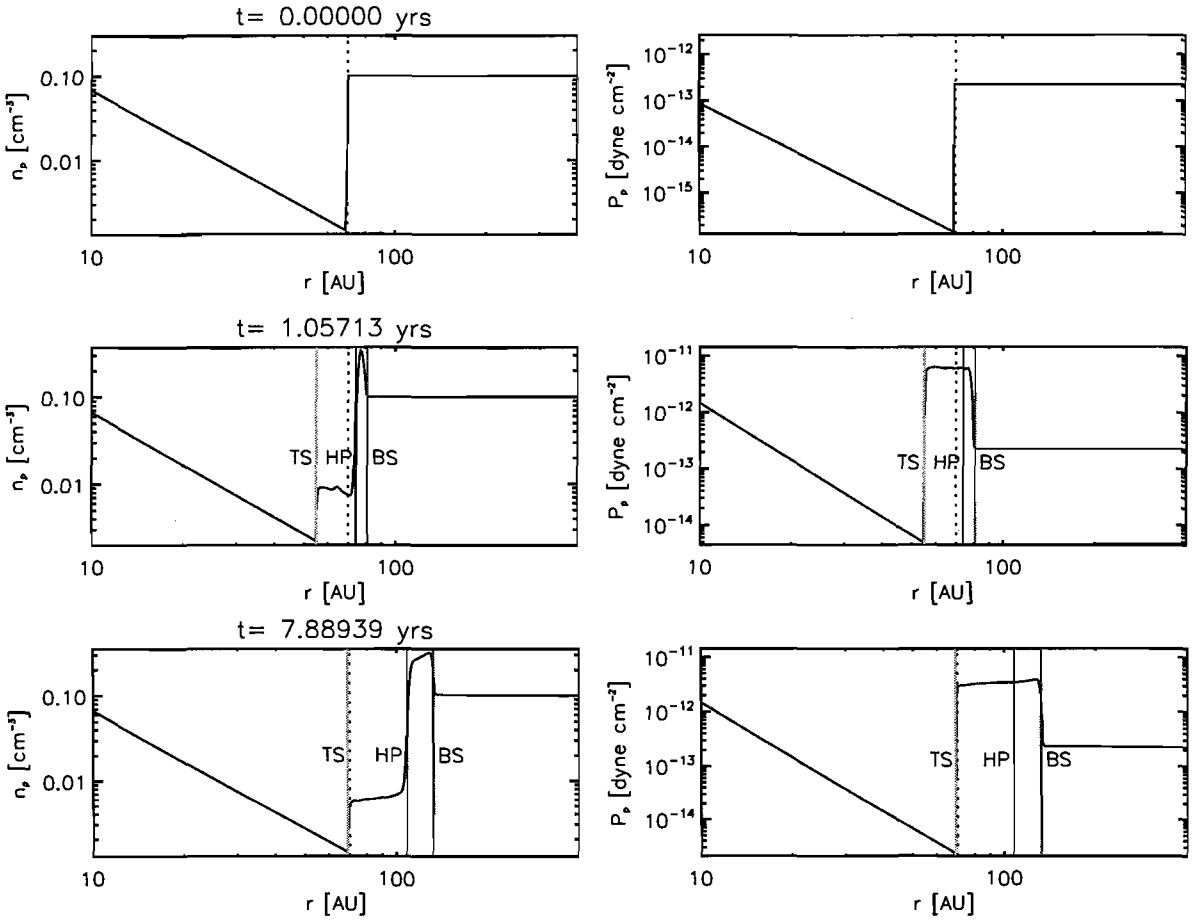

Figure 3.2: The formation of the heliosphere. Left panels show the proton density while right panels show the proton pressure, both along a one-dimensional radial path aligned anti-parallel to the LISM inflow direction. Initially the SW is allowed to expand adiabatically to a position r_d (indicated by the vertical dashed line) where the LISM is encountered. This encounter creates an interface over which density, velocity and pressure are discontinuous. The subsequent time evolution of the system results in three waves propagating away from r_d. The waves propagating furthest to the left and right (visible as jumps in density and pressure) are both shock waves (denoted by TS and BS) while the middle wave (denoted by HP, visible as a jump in density only) forms a contact discontinuity.

Recall from section 2.6 that the solution to the one-dimensional Riemann problem consisted of three simple waves propagating away from an initial discontinuity with velocities

$$\lambda^1 = v - c \quad \lambda^2 = v \quad \lambda^3 = v + c. \tag{3.9}$$

The states q_l and q_r immediately to the left and right of the discontinuous interface at $r = r_d$ in the top panel of Fig.(3.2) are now approximated by a function

$$q(r) = q_l + \eta(r) \tag{3.10}$$

where $\eta(r)$ is a continuous function subject to the condition that

$$\eta(r_d - \delta r) = 0 \quad \text{and} \quad \eta(r_d + \delta r) = q_r - q_l. \tag{3.11}$$

Two points $r_d - \delta r$ and $r_d + \delta r$ arbitrarily close to r_d are now chosen and the Roe-averaged velocity (from section 2.6) is defined in terms of $v_l = v(r - \delta r)$ and $v_r = v(r + \delta r)$ as

$$\hat{v} = \frac{\sqrt{\rho_l} v_l + \sqrt{\rho_r} v_r}{\sqrt{\rho_l} + \sqrt{\rho_r}} \tag{3.12}$$

where $\rho_l = \rho(r - \delta r)$ and $\rho_r = \rho(r + \delta r)$. Because of the approximation in Eq.(3.10) the limit where $\delta r \to 0$ exists. In theory the approximation in Eq.(3.10) can be made to an arbitrary degree of accuracy. From section 2.8 it follows that using a continuous function to approximate a discontinuity implies that a certain amount of artificial viscosity will be present in any subsequent solution. However, since the approximation can be made to an arbitrary degree of accuracy the amount of artificial viscosity will decrease for increased accuracy. With no further limitations on $\eta(r)$ in Eq.(3.11) it is, therefore, possible to make the amount of artificial viscosity go to zero. This property is used in the approximations that follow to define points arbitrarily close to r_d.

In section 2.4 the Riemann problem at a certain interface was solved by decoupling the set of nonlinear Euler equations into a set of independent linear advection equations. This method implies that a set of waves advect away from the initial discontinuity into the adjacent cells. The velocity with which these quantities are advected are the respective eigenvalues in Eq.(3.9) which depend on the bulk and sound velocities within each cell (both of which are constant over one cell dimension and one time step). However, if the piecewise constant data is approximated by a function such as Eq.(3.10), and the values to the left and right of some point r_d (corresponding to the position of the initial discontinuity) are arbitrarily close it follows for the Roe-averaged velocity $\hat{v}$ that

$$\hat{v} \approx v(r_d). \tag{3.13}$$

Therefore, if a wave propagates away from the position of the initial discontinuity at a velocity $\hat{\lambda}^2 = \hat{v} \approx v$ from Eq.(3.12) its velocity will be zero if

$$\sqrt{\rho_l} v_l = \sqrt{\rho_r} v_r \tag{3.14}$$

which implies that a steady state is reached for

$$v_l = v_r = 0 \quad \text{or} \quad \frac{v_l}{v_r} = \frac{\sqrt{\rho_r}}{\sqrt{\rho_l}}. \tag{3.15}$$

However, for a steady state $\rho v \propto r^{-2}$. Therefore, at a point $r - \delta r$ it follows that

$$\rho_l v_l \propto (r - \delta r)^{-2} \tag{3.16}$$

and similarly at $r + \delta r$

$$\rho_r v_r \propto (r + \delta r)^{-2}. \tag{3.17}$$

In the limit $\delta r \to 0$

$$\rho_l v_l = \rho_r v_r \tag{3.18}$$

which implies that the second possibility in Eq.(3.15) can only hold for trivial case where $\rho_l = \rho_r$ and $v_l = v_r$. The steady state corresponding to $v_l = v_r = 0$ defines a contact discontinuity. This can be seen from

$$\frac{\partial}{\partial t}(\rho v) + \frac{1}{r^2}\frac{\partial}{\partial r}\left[r^2\left(\rho v^2 + P\right)\right] = 0 \tag{3.19}$$

which implies for a steady state with $v_l = v_r = 0$ that

$$P_l \propto (r - \delta r)^{-2} \quad \text{and} \quad P_r \propto (r + \delta r)^{-2} \tag{3.20}$$

which yields $P_l = P_r$ if $\delta r \to 0$. Therefore, P is continuous across the wave propagating with velocity $\hat{v} \simeq v$. Since $v_l = v_r = 0$ and $P_l = P_r$ either side of this wave there can be no mass transfer across it which implies that it has to be a contact discontinuity. In the middle panel of Fig.(3.2) the contact discontinuity (denoted by HP) can be seen to correspond to a jump in density while pressure remains continuous.

The use of Roe averages to resolve discontinuities, therefore, naturally leads to a contact discontinuity being associated with λ^2 in Eq.(3.9). It can be shown that this is not a unique characteristic of using Roe averages but rather a natural occurrence in any hydrodynamical system. The phase space gradient of λ^2 is given by

$$\nabla\lambda^2 = \begin{bmatrix} \frac{\partial v}{\partial \rho} \\ \frac{\partial v}{\partial (\rho v)} \\ \frac{\partial v}{\partial E} \end{bmatrix}. \tag{3.21}$$

Since ρ, ρv and E are rectangular axis in phase space the partial derivatives $\frac{\partial(\rho v)}{\partial \rho} = \frac{\partial(\rho v)}{\partial E} = \frac{\partial \rho}{\partial E} = 0$. Therefore

$$\frac{\partial v}{\partial \rho} = \frac{1}{\rho}\frac{\partial(\rho v)}{\partial \rho} - \frac{v}{\rho} = -\frac{v}{\rho} \tag{3.22}$$

$$\frac{\partial v}{\partial(\rho v)} = \frac{\partial}{\partial(\rho v)}\left[\frac{\rho v}{\rho}\right] = \frac{1}{\rho} - \frac{1}{\rho^2}\frac{\partial \rho}{\partial(\rho v)} = \frac{1}{\rho} \tag{3.23}$$

$$\frac{\partial v}{\partial E} = \frac{\partial}{\partial E}\left[\frac{\rho v}{\rho}\right] = \frac{1}{\rho}\frac{\partial(\rho v)}{\partial e} - \frac{v}{\rho}\frac{\partial \rho}{\partial E} = 0 \tag{3.24}$$

Using r^2 from Eq.(2.57) it follows that

$$\nabla \lambda^2 \cdot r^2 = 0. \tag{3.25}$$

Recall from sections 2.3 and 2.9 that r^2 maps out the phase space trajectory of the wave travelling with velocity λ^2. In the general nonlinear case this trajectory is not a straight line. However, any two points along this trajectory can be connected by a single wave travelling at velocity λ^2. Eq.(3.25) implies that $\nabla\lambda^2$ is perpendicular to r^2 everywhere in phase space. Therefore, it follows that any adjacent points on the trajectory mapped out by r^2 will have the same value for λ^2 which in turn implies that v is continuous across such a wave. From Eqs.(3.18) and (3.19) it then follows (taking the limit $\delta r \to 0$) that P must be continuous across any wave associated with λ^2. Therefore, the wave travelling at a velocity equal to λ^2 must be a contact discontinuity.

The two other waves propagating away from the initial discontinuity at $r = r_d$ in Fig.(3.2) (denoted by TS and BS) have velocities given by

$$\hat{\lambda}^1 = \hat{v} - \hat{c} \quad \text{and} \quad \hat{\lambda}^3 = \hat{v} + \hat{c} \tag{3.26}$$

where the Roe averaged sound speed $\hat{c}$ has been defined analogously to Eqs.(2.74) and (3.12) in terms of quantities at arbitrarily close points. From Eq.(3.26) it follows that a steady state is reached for

$$\hat{v} = \pm \hat{c} \tag{3.27}$$

which defines a sonic point. Therefore, each of the two waves with velocities $\hat{\lambda}^{1/3} = \hat{v} \pm \hat{c}$ propagating away from the initial discontinuity are either a shock or a transonic rarefaction. Since the assumed SW and LISM initial states are supersonic, the above implies that at some time two stationary shocks will form at the sonic point. In this case a transonic rarefaction is not possible as a steady state solution since it is clear from Fig.(3.2) that in transiting the TS and BS both the SW and LISM density increases.

From the above analyses it can be seen that the structure of the heliosphere will consist of three interfaces. The first is a shockwave where the initially supersonic SW makes the transition to a subsonic flow. This shockwave is called the termination shock (TS). Secondly the incoming LISM (which is also supersonic) undergoes the same transition at the outer shockwave known as the bow shock (BS). Lastly a contact discontinuity known as the heliopause (HP) separates the two subsonic flow regions.

This structure describes the one-dimensional case exactly. A more general description of the SW-LISM interaction is to assume axial symmetry which necessitates that the interaction be described in two dimensions.

3.4 The one particle species heliosphere

The interaction between SW and LISM protons dominates the geometry of the heliosphere. This statement will be justified in later sections but first the heliosphere as it forms from the interaction between the SW and LISM where both mediums are still assumed to consist only of protons is discussed. The focus of this section will be on the geometry and structure of the heliosphere in two dimensions. However, it is insightful to examine the simple one-dimensional case from the previous section in order to gain insight into the numerical results that will be presented.

In the previous section it was shown that three waves propagate away from the initial point of contact between the LISM and SW along the radial path on which the directions of the SW and LISM velocities are exactly opposed. The two outermost waves form standing waves (the TS and BS) at sonic points. Because these waves become stationary they propagate a finite distance into the SW and LISM respectively. Therefore, it is expected that any steady state solution obtained for the SW-LISM interaction will contain a region in which the SW expands adiabatically between the Sun and the TS and a region where the LISM is undisturbed (outside the BS).

Since both the TS and BS become stationary at sonic points it is expected that the region between the TS and BS will be characterised by subsonic flow velocities. Furthermore, it was shown in the previous section that a contact discontinuity forms between the TS and BS called the HP. The HP becomes stationary where the velocity either side of it goes to zero. Therefore, if the proton velocity just after the TS is subsonic and greater than zero it has to decrease as the HP is approached. Similarly if the protons just inside of the BS have a finite, non zero subsonic velocity it too must decrease as the HP is approached.

Therefore, for the one-dimensional case it is expected that

$$\frac{\partial v_r}{\partial r} < 0 \quad \text{for} \quad r_{TS} < r < r_{HP} \tag{3.28}$$

$$\frac{\partial v_r}{\partial r} > 0 \quad \text{for} \quad r_{HP} < r < r_{BS} \tag{3.29}$$

where v_r now denotes the radial component of the velocity $\mathbf{v}$ and r_{TS}, r_{HP} and r_{BS} are the radial distances from the Sun to the TS, HP and BS respectively. The radial direction away from the Sun is taken as positive.

Furthermore, if the region between the TS and BS is largely characterised by subsonic flow it is expected that the density and pressure should both be approximately constant over short radial distances in the steady state solution. If the contrary applies it would imply pressure waves propagating through the subsonic region. Since these waves cannot become stationary (there is no sonic point so long as the perturbed fluid remains subsonic) these waves cannot exist in a steady state solution.

If the density is assumed to be constant over some range $[r, r+\delta r]$ where $r_{TS} < r + \delta r < r_{HP}$ and $r_{TS} < r < r_{HP}$ it follows from the conservation of mass that

$$\nabla \cdot \mathbf{v} = 0 \tag{3.30}$$

for a steady state. Furthermore,

$$\nabla \cdot \mathbf{v} = \frac{1}{r^2}\frac{\partial}{\partial r}(r^2 v_r) = 0. \tag{3.31}$$

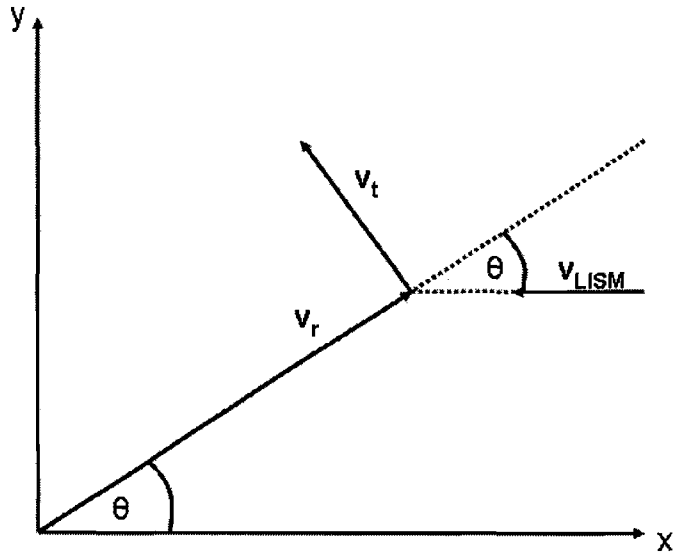

Figure 3.3: Heliocentric coordinate system for the SW-LISM interaction. The x-axis is aligned anti-parallel to the LISM inflow direction. The SW expands radially away from the origin. Along a particular radial line (defined by the angle θ with the positive x-axis) the interaction produces a tangential velocity component v_t perpendicular to the radial velocity component v_r.

Therefore, if the density is constant over some range $[r, r+\delta r]$ then $v_r \propto r^{-2}$ which is consistent with the arguments leading up to Eq.(3.28). A heliocentric coordinate system is now defined

in such a way that the x-axis lies in the solar equatorial plane directed anti-parallel to the LISM inflow as shown in Fig.(3.3). Assume that the velocity may also possess a tangential component but that the analyses is restricted to a radial path at some small angle θ to the positive x-axis extending away from the Sun. If θ is sufficiently small the initial LISM and SW velocities are to a good approximation oppositely directed. The analyses for small angles θ limited to a single radial path constitute a quasi-one-dimensional state.

From Eq.(3.31) it follows that

$$\nabla \cdot \mathbf{v} = \frac{1}{r^2}\frac{\partial}{\partial r}(r^2 v_r) + \frac{1}{r\sin\theta}\frac{\partial}{\partial \theta}(\sin\theta v_t) = 0 \tag{3.32}$$

where v_t denotes the tangential component of the velocity $\mathbf{v}$. The tangential direction is taken to be perpendicular to the radial direction pointing towards increasing values of θ as shown in Fig.(3.3). Expanding Eq.(3.32) yields

$$\frac{2v_r}{r} + \frac{\partial v_r}{\partial r} + \frac{v_t \cot\theta}{r} = 0 \tag{3.33}$$

where it was assumed that

$$\frac{\partial v_t}{\partial \theta} = 0 \tag{3.34}$$

which is consistent with analysing the SW-LISM interaction along a single radial path. Eq.(3.33) can be rewritten as

$$\frac{\partial v_r}{\partial r} = -\left[\frac{v_t \cot\theta}{r} + \frac{2v_r}{r}\right]. \tag{3.35}$$

If the left side of Eq.(3.35) is less than zero (as is expected from Eq.3.28) it implies that the right hand side of Eq.3.35 must be greater than zero. If it is further assumed that

$$\frac{\partial v_r}{\partial r} = constant \quad \text{and} \quad \frac{\partial v_r}{\partial r} < 0 \tag{3.36}$$

over some infinitesimal range $[r, r+\delta r]$ it follows that

$$\left[\frac{v_t \cot\theta}{r} + \frac{2v_r}{r}\right] = \left[\frac{v_t^* \cot\theta}{r+\delta r} + \frac{2v_r^*}{r+\delta r}\right] \tag{3.37}$$

where v_t^* and v_r^* denote values taken at $r+\delta r$. v_t and v_r denote values at r. However, since Eq.(3.28) implies $v_r^* < v_r$ it follows that $v_t^* > v_t$. Therefore, as the radial velocity decreases between the TS and the HP the tangential velocity increases which in turn implies that the protons obtain non-zero tangential velocities between the TS and HP. The same applies for the

region between the HP and BS. The simplified analyses presented above provides a context within which to examine the fully two dimensional results shown next.

The fully two dimensional solution to the SW-LISM interaction is calculated numerically. The solution is calculated on a grid similar to the one shown in Fig.(2.4) describing a plane with the Sun at the origin. The x-axis is directed anti-parallel to the LISM inflow intersecting the solar equator similar to the case shown in Fig.(3.3). A plane polar coordinate system is defined by the heliocentric radial position r and the angle θ with the positive x-axis, the former measured counter-clockwise from the positive x-direction. It is further assumed that the SW velocity close to the Sun is the same for all θ. The state of the SW at the grid points $(i, j) = (0, j)$ is specified and constitutes an inner boundary condition. Here cell index $i = 0$ referes to all cells bordering the origin (for any index of j). The state of the LISM at grid points $(i, j) = (i_{max}, j)$ (where i_{max} is the largest possible radial cell index) is also specified and constitutes an outer boundary condition. The numerical scheme used is based on the algorithm discussed in Chapter 2 and developed into a numerical model by *Fahr et al.* (2000).

The SW-LISM interaction is calculated in terms of three hydrodynamic quantities. Shown in Fig.(3.4) is the number density (top) and pressure (bottom) of the proton particle species in the plane defined above. It is assumed that the interaction is symmetric about the x-axis in Fig.(2.4). Fig.(3.5) shows the radial velocity (top) and tangential velocity (bottom) in the same plane. Note that in the bottom halves of Figs.(3.4) and (3.5) the angle θ is measured clockwise from the positive x-direction while in the top halves θ is measured counter clockwise from the positive x-direction. Fig.(3.6) shows the same quantities as in Figs.(3.4) and (3.5) along different radial paths.

Immediately visible in all three figures is that the TS encloses a region in which the SW expands radially and adiabatically as is expected from the analyses in section 3.3. The geometry of this region differs from the spherical symmetry implicit in the one-dimensional cases discussed previously. Figs.(3.4) and (3.5) clearly show that the heliocentric position of the TS exhibits a definite dependence on θ. Beyond the TS and most visible in the nose region of the heliosphere (here defined to be the region $0 < \theta < \frac{\pi}{4}$) is the HP. While the HP is still visible in the polar regions (here taken to be the region in the sector $\frac{\pi}{4} < \theta < \frac{3\pi}{4}$) as a smooth transition it completely disappears in the tail (taken to be the region $\frac{3\pi}{4} < \theta < \pi$). Lastly the BS is visible as the outermost discontinuity only in the nose and lower polar regions. The radial position of both the HP and BS also exhibit a dependence on the angle θ.

The region between the TS and the BS is called the heliosheath, subdivided into the inner heliosheath (between the TS and HP) and the outer heliosheath (between the HP and BS). As shown in Fig.(3.7) the heliosheath is primarily a region of subsonic flow except for areas in the polar region. From Figs.(3.4) and (3.6) it can be seen that the radial component of the pressure gradient throughout the heliosheath is almost zero (justifying the previous assumption that the respective densities in the inner and outer heliosheath should be approximately constant along a radial path). However, along the three different radial paths shown in Fig.(3.6) the

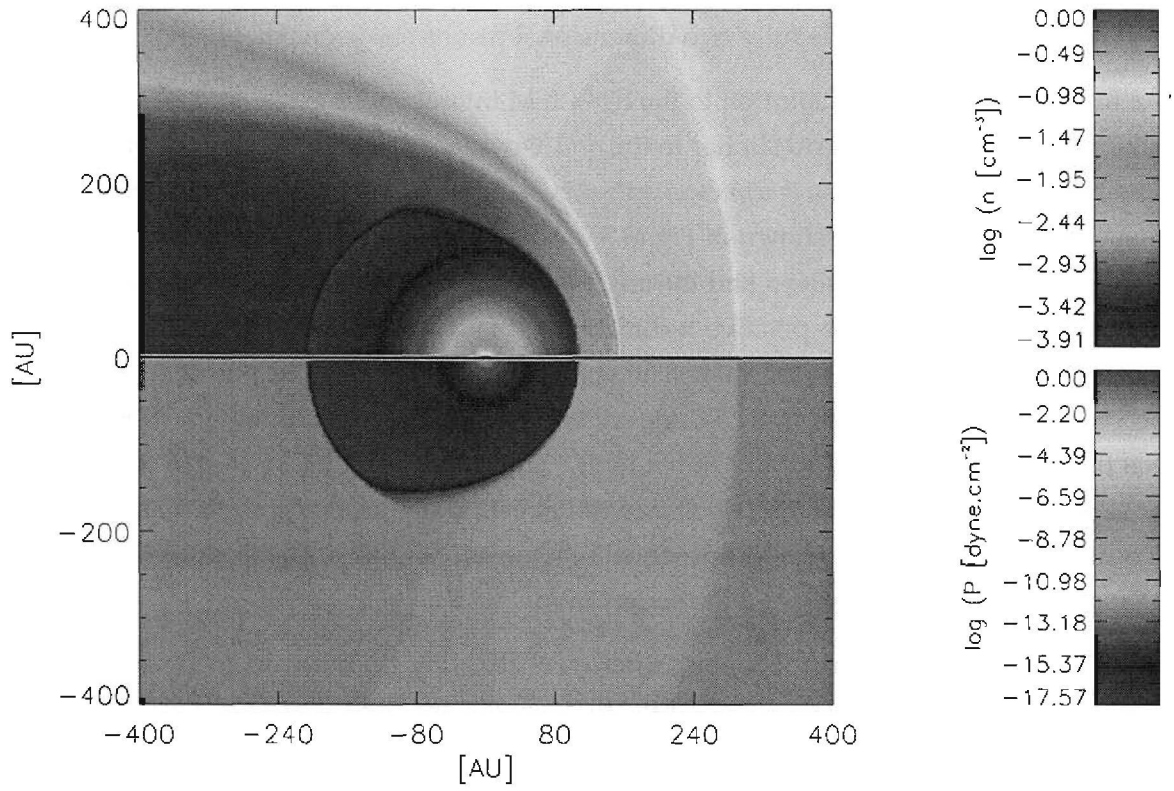

Figure 3.4: The proton particle number density (top) and pressure (bottom) in a plane parallel to the LISM inflow containing the Sun at the origin. Clearly visible are the three interfaces that form as a consequence of the SW-LISM interaction. These are the TS, HP and BS. The TS is vissible as the bullet shaped structure above corresponding to a jump in the density and pressure of the SW protons. The HP forms beyond the TS as a contact discontinuity between the SW and LISM and is only visible in density. The BS is the interface forming furthest away from the Sun corresponding to a jump in density and pressure of the LISM protons.

pressure has a different radially constant value. This implies that the pressure has a definite tangential gradient.

A tangential pressure gradient is consistent with a non-zero tangential velocity (the latter expected from the analyses shown previously in this section). The proton velocity acquires a tangential component in the heliosheath causing the subsonic SW and LISM proton species to flow around the inner heliosphere either side of the HP. It can be shown that this would also imply acceleration.

Assume that

$$\frac{\partial \rho}{\partial \theta} < 0 \tag{3.38}$$

and that over an infinitesimal interval $(\theta, \theta + \delta\theta)$

$$\frac{\partial \rho}{\partial \theta} \approx constant. \tag{3.39}$$

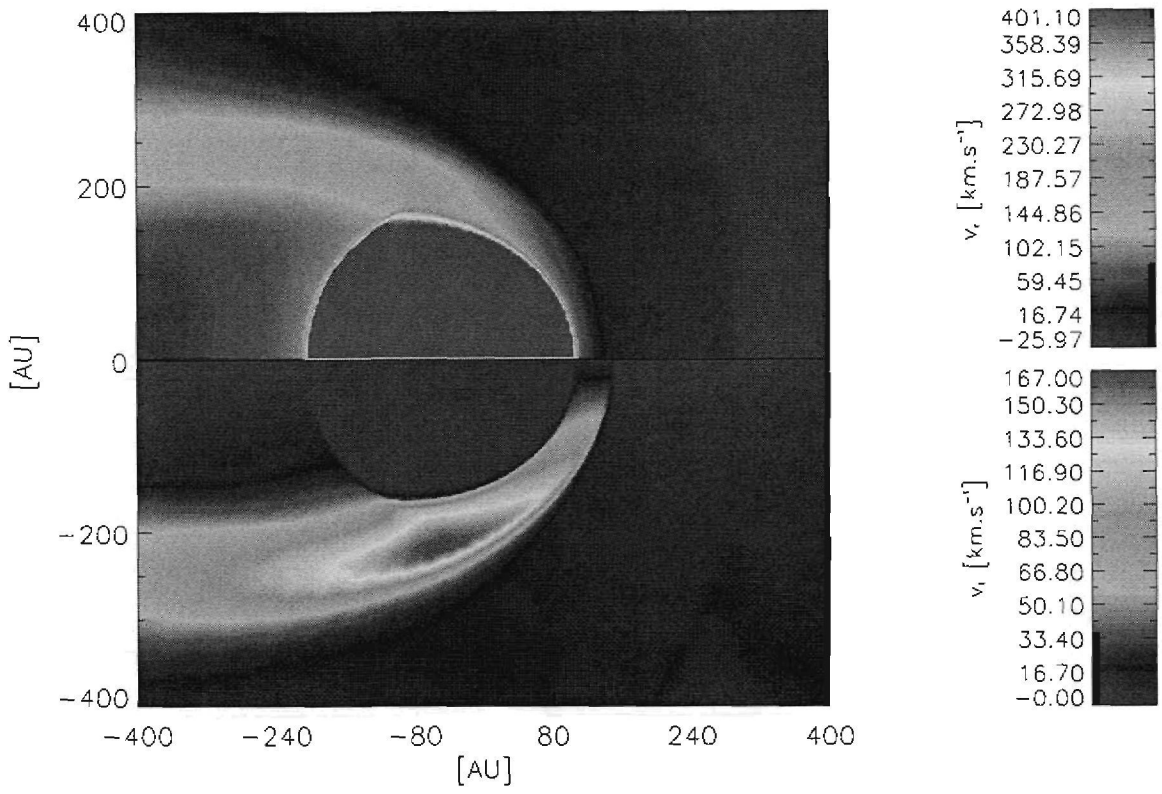

Figure 3.5: The proton radial (top) and tangential velocity (bottom) in a heliocentric plane parallel to the LISM inflow. The TS is vissible as the bullet shaped structure at which the SW radial velocity decreases almost discontiniously. The region between the TS and HP is clearly defined as a region in which the tangential velocity increases appreciably. The BS is faintly vissible as a decrease in the incomming LISM velocity.

This restricts the analyses to regions where the density decreases gradually with increasing θ. From Fig. (3.4) it can be seen that this assumption approximates conditions in the nose region fairly well. Furthermore, assume that

$$v_r(\theta) \approx v_r(\theta + \delta\theta) \tag{3.40}$$

which is also consistent with conditions in the nose region. From the conservation of mass it follows for a steady state that

$$\nabla \cdot (\rho \mathbf{v}) = 0 \tag{3.41}$$

which is expanded to

$$\mathbf{v} \cdot \nabla \rho + \rho \nabla \cdot \mathbf{v} = 0 \tag{3.42}$$

which leads to

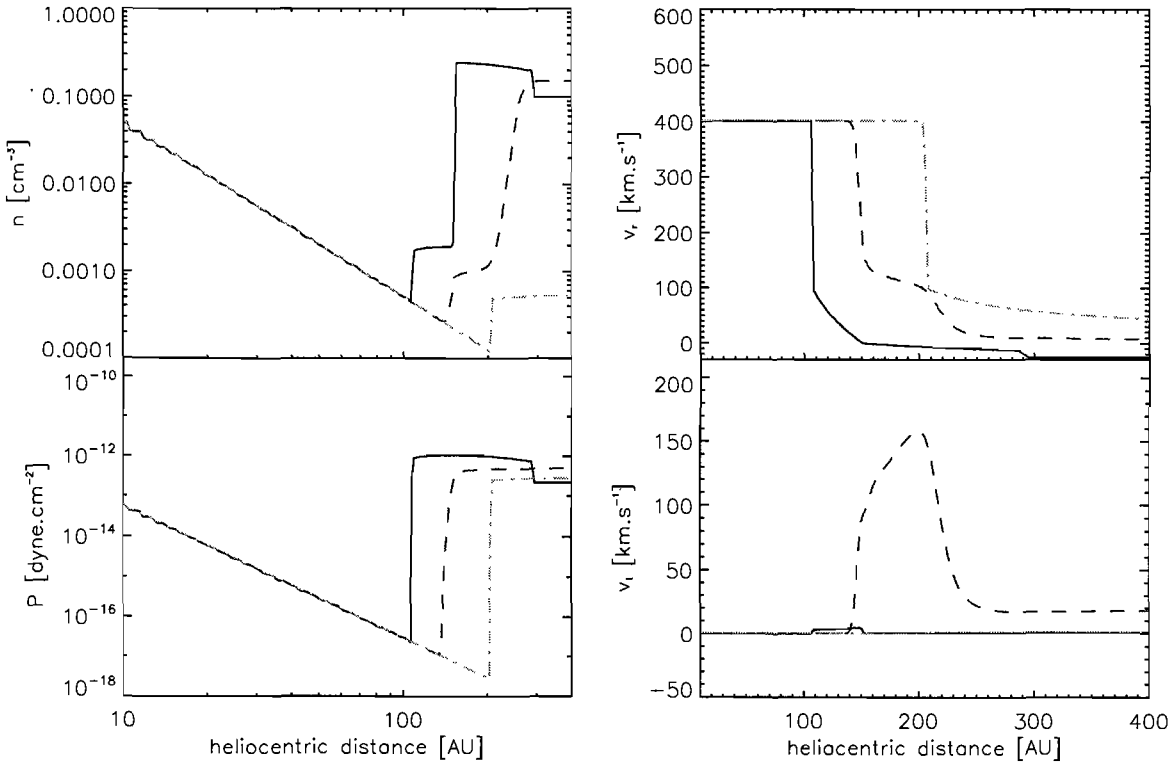

Figure 3.6: The proton particle density (top left), pressure (bottom left), radial velocity (top right) and tangential velocity (bottom right) along radial paths in the nose (solid black line), polar (blue dashed line) and tail (yellow dash-dotted line) regions.

$$v_r \frac{\partial \rho}{\partial r} + \frac{v_t}{r} \frac{\partial \rho}{\partial \theta} + \rho \left[\frac{1}{r^2} \frac{\partial}{\partial r} \left(r^2 v_r \right) + \frac{1}{r \sin \theta} \frac{\partial}{\partial \theta} \left(\sin \theta v_t \right) \right] = 0. \tag{3.43}$$

Restricting the analyses to a path of constant radius (implying that $\frac{\partial \rho}{\partial r} = 0$ and $\frac{\partial v_r}{\partial r} = 0$) yields

$$\frac{v_t}{r} \frac{\partial \rho}{\partial \theta} + \rho \left[\frac{2 v_r}{r} + \frac{v_t \cot \theta}{r} + \frac{1}{r} \frac{\partial v_t}{\partial \theta} \right] = 0 \tag{3.44}$$

which can be rewritten as

$$\frac{\partial \rho}{\partial \theta} = -\frac{\rho r}{v_t} \left[\frac{2 v_r}{r} + \frac{v_t \cot \theta}{r} + \frac{1}{r} \frac{\partial v_t}{\partial \theta} \right]. \tag{3.45}$$

If $v_t > 0$ the above implies that

$$\frac{2 v_r}{r} + \frac{v_t \cot \theta}{r} + \frac{1}{r} \frac{\partial v_t}{\partial \theta} > 0. \tag{3.46}$$

For the range $\theta \in (0, \pi)$ it follows that

$$\frac{\partial v_t}{\partial \theta} > 0 \tag{3.47}$$

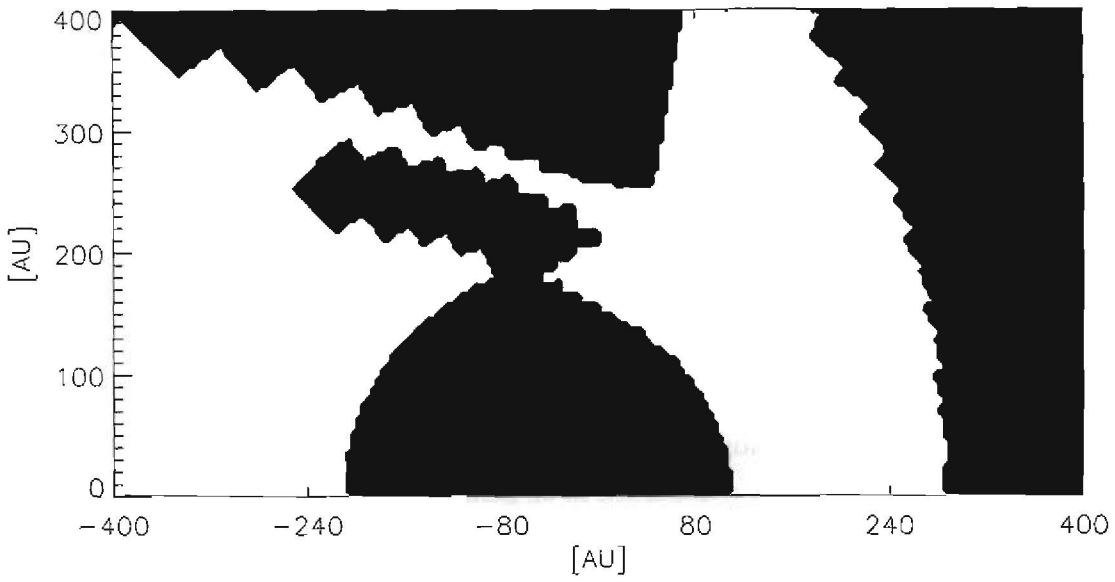

Figure 3.7: Regions of supersonic (black) and subsonic (white) flow in the heliosphere. The inner heliosphere and undisturbed LISM are characterised by supersonic velocities. The flow between the TS and BS in the nose the region (and beyond the TS in the tail) is subsonic while a region of supersonic flow exists between the TS and HP in the polar region. Beyond the HP in the polar region the flow is again supersonic.

which implies that not only is the SW 'turned' to flow around the inner heliosphere but that it accelerates in the tangential direction. From Fig.(3.7) it can be seen that this acceleration is effective enough to produce supersonic velocities in the polar regions of the heliosheath, and that the supersonic region in the heliosheath is not spatially distinct from the supersonic flow region between the Sun and TS. This result corresponds to earlier work by *Pauls and Zank* (1996) where it is noted that the negative pressure gradient in the heliosheath (called the $-\nabla P$-force) accelerates the SW to supersonic velocities in the heliosheath. The authors noted the existence of a triple point at the confluence of the two supersonic regions (between the Sun and TS and in the heliosheath) and the subsonic flow region in the tail (beyond the TS) causing the 'bullet-shaped' geometry observed in Figs.(3.4) and (3.5).

Another feature that is visible in Figs.(3.4), (3.5) and (3.6) is that the HP, while being clearly visible as a discontinuity in the nose, becomes 'smoothed out' for $\theta > 0$. Therefore, at regions above the radial path defined by $\theta = 0$ the HP stops existing as a contact discontinuity but becomes a narrow transition region between the SW and LISM. The reason for this can be seen from the following argument:

Recall from section 3.3 that the heliosphere forms due to waves travelling away from the initial point of contact between the SW and LISM. In two dimensions this implies waves travelling in both the tangential and radial directions. A characteristic time $\tau_r \propto \lambda_{r,max}^{-1}$ is defined where $\lambda_{r,max}$ is the velocity of the fastest wave travelling along the radial direction. τ_r is an indication of the time it takes for all radial waves arising from the initial point of contact between the SW and LISM to slow down significantly or dissipate. Let the characteristic time for all waves

forming along the tangential direction be defined similarly as $\tau_t \propto \lambda_{t,max}^{-1}$ where $\lambda_{t,max}$ is the velocity of the fastest wave travelling along the tangential direction at any given time.

Assume that $\tau_r << \tau_t$ for short times after initial contact between the SW and LISM. This implies that some intermediate state is reached before the formation of a complete steady state within which the radial waves have slowed down significantly (forming a quasi-steady state) but in which the tangential waves are still present moving very slowly compared to typical radial velocities.

To a good approximation this quasi-steady state should resemble the one-dimensional case discussed in the previous section i.e. initial adiabatic expansion towards the TS, $v_r \propto r^{-2}$ between the TS and the HP and v_t assumed to be zero everywhere. Therefore, arbitrarily close to the HP at some radial position r_{HP}, $v_t = v_r = 0$ and $P(r_{HP} - \delta r) = P(r_{HP} + \delta r)$.

At some later time the developing tangential velocity component will have a noticeable influence on this quasi-steady state changing the state close to the HP as $v_t \neq 0$ and $v_r = 0$. If it is assumed that the tangential velocity acquired on the solar side of the HP is much larger than the tangential velocity acquired by the LISM on the other side it implies that the density decreases (due to the net tangential flux outward) causing $P(r_{HP} - \delta r) < P(r_{HP} + \delta r)$. Therefore, where the HP existed as a contact discontinuity in the quasi-steady state there now exists a pressure gradient across it causing mass flow across the position where the HP once was. Subsequently this mass flow reestablishes pressure equilibrium.

The influence of the tangential component acquired by SW and LISM protons either side of the HP causes the contact discontinuity to devolve into a transition region. The thickness of this transition region increases with increasing θ with a true contact discontinuity existing only along the radial path $\theta = 0$ as seen in Figs.(3.4), (3.5) and (3.6).

The structure of the heliosphere as it forms due to the interaction between the SW and LISM can, therefore, be summarised as consisting of three interfaces called the TS, HP and BS. The TS encloses a region in which the SW expands supersonically, adiabatically and radially. At the TS the SW undergoes a transition to a subsonic flow. Similarly the BS separates a region of unperturbed supersonic LISM protons from a region in which the LISM is subsonic. The region between the TS and BS contains a third interface (called the HP) which separates the subsonic SW and LISM protons. In the heliosheath the SW and LISM protons obtain pronounced tangential velocities causing the two species to flow around the 'supersonic bubble' encapsulated by the TS.

Having established the basic structure and characteristics of the heliosphere the sensitivity of this structure and its characteristics to different boundary conditions are investigated in the next section.

Model	$n_{p,SW}$ (cm^{-3})	$v_{p,SW}$ ($km.s^{-1}$)	$T_{p,SW}$ (K)	$n_{p,LISM}$ (cm^{-3})	$v_{p,LISM}$ ($km.s^{-1}$)	$T_{p,LISM}$ (K)
1	5.0	400.0	10^5	0.10	26.0	8000
2	2.5	400.0	10^5	0.10	26.0	8000
3	7.5	400.0	10^5	0.10	26.0	8000
4	5.0	300.0	10^5	0.10	26.0	8000
5	5.0	450.0	10^5	0.10	26.0	8000
6	5.0	400.0	5×10^4	0.10	26.0	8000
7	5.0	400.0	2×10^5	0.10	26.0	8000
8	5.0	400.0	10^5	0.05	26.0	8000
9	5.0	400.0	10^5	0.20	26.0	8000
10	5.0	400.0	10^5	0.10	25.0	8000
11	5.0	400.0	10^5	0.10	27.0	8000
12	5.0	400.0	10^5	0.10	26.0	6000
13	5.0	400.0	10^5	0.10	26.0	9000

Table 3.2: Parameters used to calculate different instances of the SW-LISM interaction.

3.5 Heliospheric sensitivity to SW and LISM parameters

In section 3.4 the structure and characteristics of the heliosphere are investigated assuming a certain state for the SW and LISM at the inner and outer boundaries of the grid in Fig.(2.4) respectively. In this section the dependence of the heliospheric structure and its associated characteristics on the assumed state of both the SW and LISM at the aforementioned boundaries are investigated. As mentioned in section 3.2 the state of both the SW close to the Sun and LISM at large heliocentric distances are not defined in absolute terms. Rather a plausible range of parameters exist describing the aforementioned states. In this section a parameter study is presented to gauge the sensitivity of the heliosphere to different plausible states assumed for the SW and LISM. The SW and LISM are still assumed to consist of protons alone. It is important to note that the inclusion of neutral atoms and PUI's in the SW interaction will influence the results presented here. A parameter study including these effects is presented in the next chapter.

Listed in Table 3.2 are the different boundary conditions for which the heliosphere is calculated. Model 1 is taken as a reference model. It is assumed that the SW has the same velocity, density and temperature for all angles θ in Fig.(3.3) and that the y-axis in Fig.(3.3) correspond to the solar axis of rotation.

Shown in Fig.(3.8) are the radial position of the TS, HP and BS for $\theta \in [0^0, 180^0]$ calculated for the different models listed in Table 3.2. θ is taken as the angle between a radial line and the positive x-axis, as shown in Fig.(3.3). From Fig.(3.8) it is immediately visible that the position of the TS, HP and BS is sensitive to the dynamic pressure (defined as ρv^2 where v is the magnitude of the total velocity) of the SW and LISM. Increasing either the density or the velocity of the SW (or LISM) causes the TS, HP and BS to form at larger (or smaller in the case of LISM increases) heliocentric distances compared to the reference model. Decreasing either the density or velocity of the SW (or LISM) causes the opposite effect.

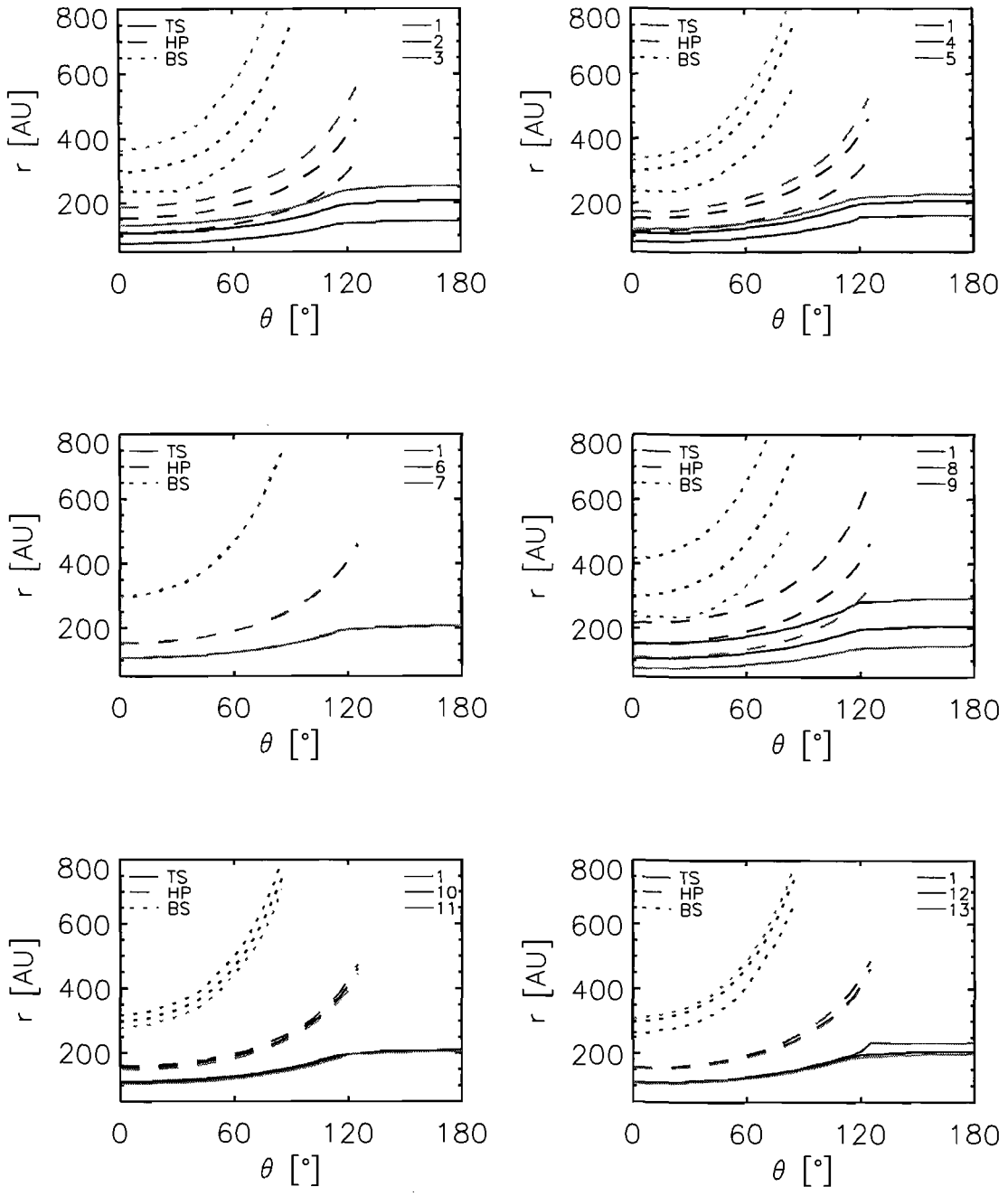

Figure 3.8: The heliocentric radial position of the TS (solid line), HP (dashed line) and BS (dotted line) for $\theta \in [0^0, 180^0]$ calculated from different boundary conditions, as listed in Table 3.2. Numbers 1-13 in the graphs correspond to the same numbers in Table 3.2.

Specifically it is seen that a 50% reduction in the SW density (from 5.0 cm^{-3} to 2.5 cm^{-3}) at the inner boundary causes the TS, HP and BS to form at radial distances in the nose which are $\sim$ 28% less than the same positions for the reference model. A 50% increase in the same parameter (from 5.0 cm^{-3} to 7.5 cm^{-3}) causes the radial positions of the TS, HP and BS in the nose to increase by $\sim$ 24%. Reducing the SW velocity by 25% (from 400 $km.s^{-1}$ to 300 $km.s^{-1}$) leads to the TS, HP and BS being $\sim$ 25% closer in the nose while increasing the SW velocity by 12.5% (from 400 $km.s^{-1}$ to 450 $km.s^{-1}$) causes the radial positions of the same three interfaces to increase by $\sim$ 15% in the nose.

From Fig.(3.8) it can be seen that altering the SW temperature by 50% (from 10^5 K to both 5×10^4 K and 2×10^5 K) does not affect the formation of either the TS, HP or BS visibly. Due to the supersonic nature of the SW between the Sun and the TS its dynamics are dominated by the ρv^2 contribution to the amount of energy per unit volume. For a typical SW velocity of $\sim$ 400 $km.s^{-1}$ and a SW density of $\sim$ 5 cm^{-3} the energy associated with the ρv^2 term is $\sim 10^{-9}$ $erg.cm^{-3}$. The thermal contribution (for an assumed temperature of $\sim 10^5$K and typical density of 5 cm^{-3}) is of the order $\sim 10^{-12}$ $erg.cm^{-3}$. Furthermore, due to the adiabatic expansion of the SW between the Sun and the TS, the thermal pressure (which is a measure of the amount of thermal energy per unit volume) decreases more with increasing radial distance than does the ρv^2 contribution.

From Fig.(3.6) it is visible that the TS corresponds to a discontinuous increase in density and thermal pressure, while velocity decreases discontinuously. Since the thermal pressure is a measure of the amount of thermal energy per unit volume this implies that some of the kinetic energy of the SW (associated with ρv^2) has been converted to thermal energy. The thermal energy of the SW, therefore, plays a larger role in the heliosheath (where the velocity is subsonic).

However, from Fig.(3.8) it can be seen that increasing the temperature of the SW at the inner boundary does not alter the volume of the inner heliosheath at all, even though the volume of the inner heliosheath should be in part dependent on the thermal properties of the SW. This apparent contradiction can be resolved by noting that the thermal energy of the SW in the heliosheath depends on the amount of kinetic energy that is converted to thermal energy at the TS. Since the amount of kinetic energy of the supersonic SW before the TS is dominated by the ρv^2 term, it implies that the thermal energy (and subsequent temperature) of the SW in the heliosheath does not depend on the SW temperature at the inner boundary (as long as the SW is supersonic at this boundary).

Evident from Fig.(3.8) is that an increase in the density or heliocentric velocity of the LISM causes the TS, HP and BS to form at distances closer to the Sun. The opposite applies for decreases in the density or velocity associated with the LISM. Specifically a 50% increase in the LISM density (from 0.1 cm^{-3} to 0.2 cm^{-3}) leads to the TS, HP and BS forming $\sim$ 30% closer to the Sun in the nose region. Decreasing the LISM density by 50% (from 0.1 cm^{-3} to 0.05 cm^{-3}) causes the same three interfaces to form at distances $\sim$ 43% farther away from the Sun in the nose. A 4% increase in the LISM heliocentric velocity (from 26 $km.s^{-1}$ to 27 $km.s^{-1}$) leads to

the TS, HP and BS forming $\sim 4\%$ closer to the Sun while a 4% decrease in the same parameter (from 26 km.s^{-1} to 25 km.s^{-1}) causes the three interfaces to form at positions which are $\sim 4\%$ further out in the nose region.

From Fig.(3.8) it can be seen that the position of the TS, HP and BS depend slightly on the assumed LISM temperature at the outer boundary. Specifically a 12.5% increase in the LISM temperature (from 8000 K to 9000 K) leads to the TS and HP forming slightly closer to the Sun, with the effect only being truly visible in the polar and tail regions. The same increase, however, causes the BS to form $\sim 4\%$ further away from the Sun in the nose than was the case for the reference model. This implies that an increase in the LISM temperature acts to increase the volume of the outer heliosheath slightly.

Lastly it can be seen that decreasing the LISM temperature at the outer boundary by 25% (from 8000 K to 6000 K) causes the BS to move inward by $\sim 10\%$ while the HP and TS form at slightly larger heliocentric distances. Interestingly such a reduction of the LISM temperature at the outer boundary significantly influences the TS geometry in the tail regions, where it is seen that the TS becomes spherical for $\theta > 120^0$.

3.6 Summary

The numerical scheme discussed in Chapter 2 is used in this chapter to show how the heliosphere forms, what its characteristic structure and properties are and how sensitive it is to assumed boundary conditions for a case where only protons are considered.

Specifically it is shown that the heliosphere forms as three waves propagate away from the initial point of contact between the SW and LISM. As these waves become stationary (forming two stationary transonic shocks and a contact discontinuity) the heliosphere forms. The heliosphere is characterised by three regions, two being the unperturbed SW and LISM plasmas and the third (called the heliosheath) forming where the former two supersonic fluids undergo transitions to subsonic flows. The heliosheath is characterised by high densities, high thermal pressures, radial deceleration and tangential acceleration. The positions of the two stationary shocks and the contact discontinuity depend on the assumed states of the SW (close to the Sun) and the LISM (at large heliocentric distances). Specifically the dynamic pressure of either the SW or the LISM influences the structure of the heliosphere greatly. In the next chapter this will be shown to hold for the case where other particles (such as hydrogen and pick-up ions) are considered. In the penultimate chapter of this work this result will be used in determining the time dependent state of the heliosphere from a range of spacecraft data.

The 'protons only' case discussed in this chapter dominates the structure of the heliosphere in the sense that, even as more particle species are considered the heliosphere retains its two shock structure (as long as the SW and LISM remain supersonic). The influence of other particles (such as hydrogen and PUI's) are important though and is the topic of the next chapter.

Chapter 4

The heliosphere II

4.1 Introduction

In Chapter 3 the SW-LISM interaction is described for the simplified case where it is assumed that the SW and LISM consist solely of protons. Apart from protons, the LISM also contains a significant number of neutral hydrogen atoms, the abundance of which is roughly of the same order as the LISM proton component. In this chapter it will be shown that the addition of neutral atoms to the SW-LISM interaction requires that the neutral atom population be treated separately (due to the differences in the proton-proton, proton-hydrogen and hydrogen-hydrogen interaction cross sections). Specifically the separate hydrodynamical treatment of the neutral hydrogen population is formulated and the subsequent effect on the SW-LISM interaction is studied.

In order to understand the effect of neutral atoms on the SW-LISM interaction the various mutual interactions between hydrogen atoms and protons are investigated and different theoretical approaches to modelling these interactions are briefly discussed. Of specific interest is the hydrodynamical approach, where it is assumed that the dynamics of the neutral hydrogen species is described by a set of Euler equations. This approach couples the neutral hydrogen and proton species through various source terms describing the exchange of mass, momentum and energy. These source terms are listed explicitly in this chapter.

Results from a hydrodynamical model that include the effect of neutral hydrogen atoms on the SW-LISM interaction are presented. These results are then compared to similar results calculated for the 'protons only' case. The chapter concludes with a parameter study which is compared to the results from section 3.5 explicitly showing the effect neutral atoms have on the heliosphere forming from different assumed SW and LISM states. The results from the parameter study are also compared to calculations from *Müller et al.* (2006), who used an alternative hydrodynamical formulation describing the SW-LISM interaction.

4.2 Hydrogen and PUI's in the heliosphere

The presence of neutral atoms in the LISM (see section 3.2) necessitates that different types of particle interactions must be considered in any description of the SW-LISM interaction. Implicit to the 'protons only' case discussed in Chapter 3 is that protons interact via long range electromagnetic fields in such a way that the proton velocity distributions of both the SW and LISM relax towards Maxwellian distributions centred on their respective bulk velocities. In the context of hydrodynamics the distribution function of an ordinary isolated fluid relaxes to a Maxwellian distribution if left to itself, through collisions between particles in the fluid. The dynamics of such a fluid can be calculated from the Euler-equations (given in Chapter 2), which contains no information about specific particles or the collisions between them. For the SW and LISM a Maxwellian distribution implies that the electromagnetic interactions between protons can be approximated as collisions between 'ordinary' particles, where the long range Coulomb interaction between two protons is contained in an appropriate collision cross section. Subsequently the SW-LISM proton interaction can be calculated from the Euler-equations. Modelling the proton population hydrodynamically, therefore, implies that these Coulomb interactions are efficient enough to keep the proton velocity distribution Maxwellian.

The presence of neutral atoms in the LISM increases the number of interactions that may occur. A complete list of such interactions is given by *Zank* (1999). Of these the most important are the Coulomb interactions between protons (acting to keep the respective proton species in equilibrium), collisions between hydrogen atoms themselves, charge exchange interactions between hydrogen atoms and protons, electron impact ionisation between hydrogen atoms and sufficiently energetic electrons, and photoionisation.

Collisions between similar particles (Coulomb collisions in the case of protons and collisions between different hydrogen atoms) act to produce a Maxwellian velocity distribution. Alternatively interactions between dissimilar particle species may induce departures from a Maxwellian velocity distribution in either (or both) of the respective particle velocity distributions. This is illustrated best by considering charge exchange. Charge exchange between a proton and hydrogen atom implies that after the interaction the two particles swap charge without transferring momentum (see *Holzer*, 1989; *Zank*, 1999). Therefore, a proton created in a charge exchange interaction retains the kinetic properties of its parent hydrogen atom.

Now assume that some volume contains a number of protons and hydrogen atoms that interact via charge exchange and that the proton and hydrogen species can be described by separate Maxwellian distributions centred on different bulk velocities (for the sake of argument assume that the hydrogen bulk velocity is less than the proton bulk velocity).

The number of collisions η occurring per unit time per unit volume is proportional to the relevant collision cross section σ, the relative velocity v_{rel} between the two particle species and the densities n_1 and n_2 of both species. Therefore,

$$\eta \propto \sigma v_{rel} n_1 n_2. \tag{4.1}$$

In general σ depends on v_{rel}. Assume that some optimal relative velocity exists (say for $v_H = x$ m.s^{-1} and $v_p = y$ m.s^{-1}) so that η is maximal. This implies that charge exchange between protons and hydrogen atoms adds appreciable numbers of protons with velocity x m.s^{-1} to the proton velocity distribution, while removing the same number of protons with velocity y m.s^{-1} from it (the opposite happens for the hydrogen species). If collisions between protons themselves do not occur with sufficient frequency (approximately equal to the frequency of charge exchange) the net effect of charge exchange interactions is to cause an asymmetric departure from the initial Maxwellian proton velocity distribution function. The same goes for the hydrogen distribution function.

Similar asymmetries occur for electron impact and photoionisation. For electron impact or photoionisation to occur an electron or photon (possessing enough energy to ionise a hydrogen atom) collides with a neutral hydrogen atom stripping it of one electron. Electron impact and photoionisation, therefore, act to increase the number of protons with a certain velocity (while decreasing the number of hydrogen atoms) which may cause departures from an initial Maxwellian velocity distribution if proton-proton (and hydrogen-hydrogen) collisions do not occur at a sufficient rate.

In the context of a purely hydrodynamical formulation these interactions can be problematic since such a formulation requires that all the particle species velocity distributions are Maxwellian. It will be shown, however, that in the context of the heliosphere a purely hydrodynamical formulation of the SW-LISM interaction (with the latter containing both protons and hydrogen atoms) is possible and yields accurate results.

The first assumption made is that the proton interaction in the SW and LISM can still be described hydrodynamically, similar to the case in Chapter 3. Secondly it is assumed that the heliosphere still forms with approximately the same characteristics as shown in Figs.(3.4) and (3.5) even if neutral atoms affect the SW-LISM interaction. This implies that proton-proton collisions remain the dominant process characterising the heliosphere. This will be shown to hold in section 4.4 where the SW-LISM interaction is calculated self-consistently. From these assumptions it follows that neutrals from the LISM enter the heliosphere by propogating accross the BS.

From the results in section 3.4 it follows that LISM protons (in nose region of the heliosphere) traversing the BS experience deceleration as the HP is approached and acquire appreciable tangential velocities as the proton species is forced by the SW to flow around the HP. As this is a result of the proton-proton interaction between the SW and LISM the hydrogen atoms do not experience a similar change in state. Outside the BS it is expected that the relative velocity between the LISM protons and neutral atoms is small. Since it is assumed that the bulk motion of the LISM protons and hydrogen atoms is aligned, the relative velocity between a proton and hydrogen atom is entirely due to thermal motion. Beyond the BS the proton component is

heated, compressed, decelerated and 'turned'. This implies that both the relative thermal and bulk velocities between protons and hydrogen atoms should increase as the BS is traversed.

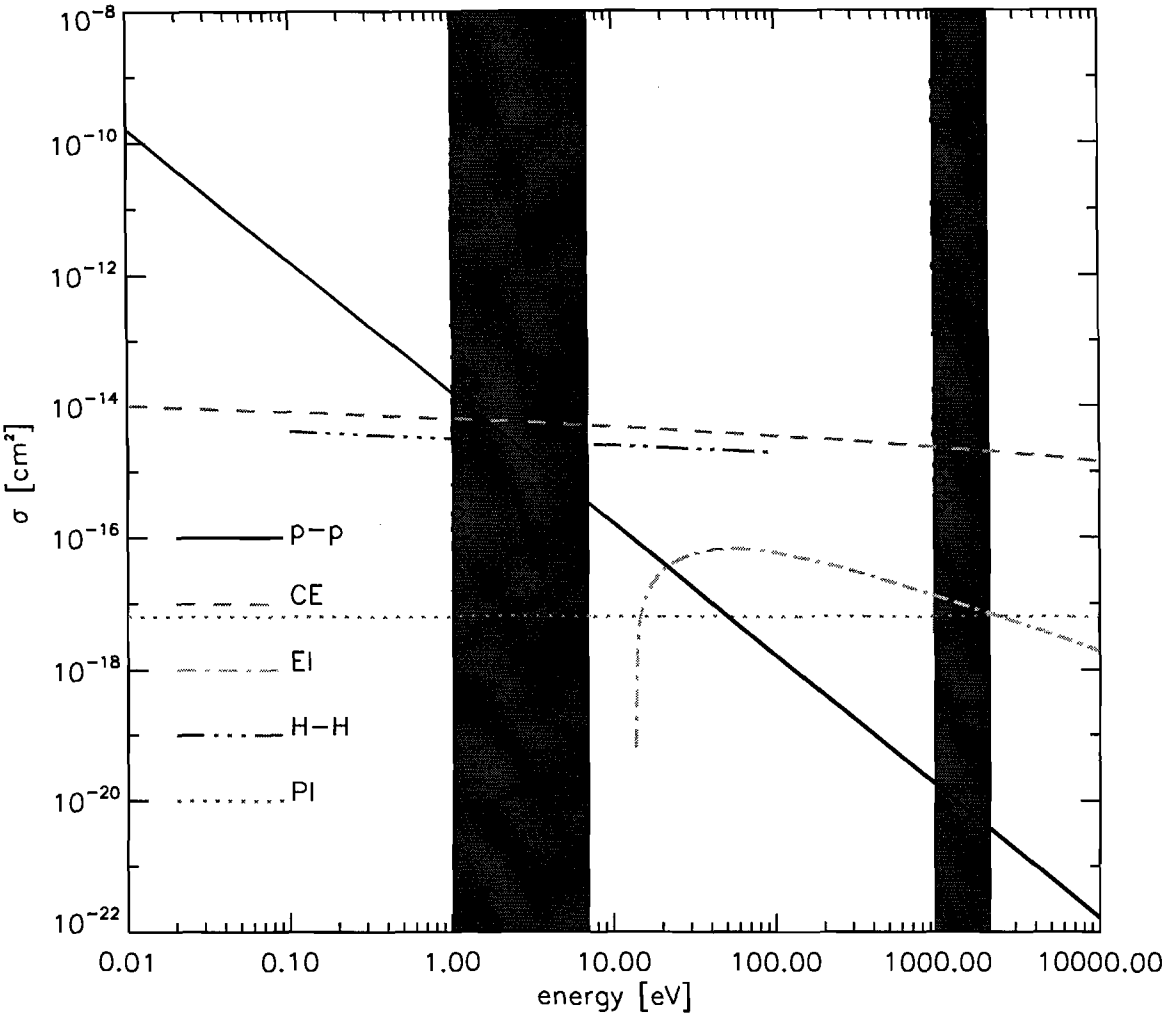

Figure 4.1: Charge exchange (CE), photoionisation (PI) and electron-impact ionization (EI) cross sections for different interaction energies. The cross sections are taken from *Fite et al.* (1962); *Allen* (1973) and *Lotz* (1967) respectively. Also shown are the hydrogen-hydrogen (H-H) collision cross section (see *Zank*, 1999, for reference), and the Coulomb cross section (p-p) for protons (from *Chen*, 1974). The filled areas represent the energy ranges of LISM particles (both outside the BS and inside the outer heliosheath) and SW particles (both in the inner heliosphere and inner heliosheath). More recent 'best fit' cross section data is obtained by *Lindsay and Stebbings* (2005). See also *Fahr et al.* (2007).

To quantify this change the relevant cross sections are shown in Fig.(4.1). From Fig.(4.1) it can be seen that particle energies in the LISM and outer heliosphere are not sufficient to induce electron impact ionisation (EI) and due to the large distance from the Sun photoionisation (PI) can be neglected in this region (see *Zank*, 1999; *Fahr et al.*, 2000). For the range of particle energies that characterise the LISM and outer heliosheath the charge exchange (CE) cross section is approximately constant. The change in state that the LISM protons incur as the BS is traversed acts to increase the number of collisions in Eq.(4.1) since the proton density increases, as well

as the relative velocity taken from *Holzer* (1972) as

$$v_{rel} = \sqrt{\frac{128k_b}{9\pi m_p}(T_p + T_H) + (\mathbf{v}_p - \mathbf{v}_H)\cdot(\mathbf{v}_p - \mathbf{v}_H)}. \tag{4.2}$$

It is, therefore, expected that charge exchange will play a significant role in the outer heliosheath (it will be argued below that this is the region where most charge exchange collisions occur). If it is assumed that the proton and hydrogen distributions in the undisturbed LISM are Maxwellian it follows that significant departures from these distributions may be incurred in the outer heliosheath. However, from Fig.(4.1) it can be seen that the proton-proton cross section is the largest cross section close to lower energies in the heliosheath. These lower energies correspond to the slow, hot protons that populate the outer heliosheath. Fig.(4.1), therefore, suggests that proton-proton collisions will act to restore the Maxwellian proton distribution in the outer heliosheath and that any departure from a Maxwellian distribution should be marginal for protons. This is supported by the results of *Fahr and Bzowski* (2004).

Regarding the hydrogen species in the outer heliosheath it can be seen that the hydrogen-hydrogen cross section is almost $\sim 50\%$ less than the charge exchange cross section (for all particle energies encountered in the LISM and outer heliosheath). This implies that charge exchange induced departures from an initial Maxwellian distribution are not effectively counteracted by collisions among hydrogen atoms (see also *Fahr and Bzowski*, 2004). This implies that a hydrodynamical description of hydrogen atoms may incur the largest errors in the outer heliosheath (as found by *Heerikhuisen et al.*, 2006). In a later section it will be shown that while such errors are incurred, the hydrodynamical approach captures the state of SW protons (modified through their interaction with neutral atoms) and the characteristics of the hydrogen population accurately.

Recall from section 3.4 that the HP formed as a contact discontinuity (or transitional region) between the SW and LISM protons in the inner and outer heliosheath across which little or no mass transport takes place. Since this is a consequence of proton-proton interactions neutral hydrogen atoms are free to propagate across the HP (barring any effects occurring in the outer heliosphere that may impede such a crossing). Compared to the LISM proton density in the outer heliosheath the inner heliosheath is approximately 10^3 times less dense (as can be seen from Fig.3.6). Furthermore, from Fig.(4.1) it can be seen that the charge exchange cross section is significantly reduced at these energies (compared to particle energies in the outer heliosheath). This implies that charge exchange will occur less frequently in this region than was the case for the outer heliosheath. Since the inner heliosheath is the only region where electrons may acquire sufficient thermal energies to ionize neutral hydrogen atoms electron impact ionisation may also occur in this region, although at an even lesser rate than charge exchange interactions due to the comparatively small electron impact cross section (see Fig.4.1).

In the inner heliosphere most of the SW proton species energy is associated with its supersonic velocity, while in the inner heliosheath the largest contribution to the energy is thermal. There-

fore, electron impact ionisation can be neglected in the former region. As hydrogen atoms propagate toward the Sun increasing numbers of protons are encountered due to the adiabatic expansion of the SW. The proton number density at $\sim$ 5 AU is of the same order as the LISM proton density in the outer heliosheath. However, due to the reduced value of the charge exchange cross section in this region (due to its energy dependence, shown in Fig.4.1) it can be expected that this close to the Sun charge exchange interactions will occur at a significantly lesser rate than in the outer heliosheath.

Charge exchange in the inner heliosphere implies that relatively slow hydrogen atoms (characterised by the relative velocity between the Sun and LISM) exchange charge with relatively fast SW protons. The result is slow protons created in the SW and fast hydrogen atoms added to the neutral species. From Fig.(4.1) and Eq.(4.1) it can be seen that such a fast hydrogen atom is unlikely to have any subsequent interactions with SW protons. Since the newly created hydrogen atom has a velocity comparable to that of a SW proton, v_{rel} in Eq.(4.1) is greatly reduced allowing these fast neutral atoms to escape into the outer heliosheath without encountering another proton. In the outer heliosheath the probability of interacting with a proton is increased slightly. However, since the charge exchange cross section for an interaction between a fast moving neutral atom and a slow moving proton is still $\sim$ 80% less than the charge exchange cross section for the interaction between a slow hydrogen atom and a slow proton the former interaction is completely dominated by the latter in the outer heliosheath. Regarding the dynamics of the proton species these fast neutrals are, therefore, dynamically unimportant (see *Zank et al.*, 1996; *Fahr et al.*, 2000).

Slow protons created in the SW through charge exchange are, however, important. Due to the extremely small proton-proton cross section at SW energies it is unlikely that these newly created protons will interact with the bulk SW in such a way to produce a single Maxwellian distribution. These newly created protons constitute a third, separate particle species called pick-up ions (PUI's). The dynamics of PUI's in the heliosphere are extremely important. As stated in section 3.2, PUI's provide a seed population for anomalous cosmic rays (ACR's). PUI production also influences the SW dynamically, as will be shown later in this section. Due to their importance, a brief summary of PUI's in the heliosphere follows.

Although the SW can be modelled hydrodynamically, in reality it is a fully ionised plasma. Embedded in the SW plasma is the interplanetary magnetic field. In the hydrodynamical formulation information regarding the magnetic field is lost. However, in describing the dynmaics of PUI's it is momentarily necesary to examine the effect of the embedded magnetic field on the motion of PUI's in the SW. It will be shown that the end result still allows for the hydrodynamic formulation of the SW-LISM interactrion. As PUI's are created in the SW they immediately respond to the interplanetary magnetic field so that (see *Fahr*, 1973)

$$m_p \frac{d\mathbf{v}}{dt} = q\left[(\mathbf{v} - \mathbf{v}_{SW}) \times \mathbf{B}\right] \tag{4.3}$$

where m_p is the proton mass, v is the velocity of a single PUI, v_{SW} is the SW bulk velocity and **B** is the interplanetary magnetic field vector. q is the proton charge. Eq.(4.3) describes the gyration of PUI's around interplanetary magnetic field lines. Apart from gyration PUI's are scattered (and their distribution subsequently isotropised) by ambient fluctuations in the interplanetary magnetic field (such as turbulence) and through self generated low frequency fluctuations (see *Wu and Davidson*, 1972; *Lee and Ip*, 1987). These effects are discussed in great detail by *Zank* (1999). As can be seen from Eq.(4.3) the PUI velocity becomes constant as $v = v_{SW}$. The net effect of gyration and scattering of PUI's (ignoring other transport effects such as diffusion and drift. See *Fichtner et al.*, 1996a) is a radially symmetric PUI velocity distribution, given as (from *Fahr et al.*, 2000)

$$f_{PUI}(\mathbf{r}, v) = \begin{cases} constant & v \leq v_{SW}(\mathbf{r}) \\ 0 & v > v_{SW}(\mathbf{r}). \end{cases} \tag{4.4}$$

Compared to charge exchange, PUI-PUI and PUI-SW interactions are negligible. This results in the non-Maxwellian PUI distribution function (Eq.4.4) and PUI's forming a distinct particle population separate from the SW protons. Regarding the SW velocity distribution, charge exchange with slow neutrals induces a net loss of fast protons (exchanged for slow PUI's subsequently accelerated by electromagnetic forces) and should cause a deviation from an initial Maxwellian velocity distribution for SW protons. If the number of PUI's created are significantly less than the SW proton number density at a specific point in space and time these deviations should be negligible, allowing for the hydrodynamic description of SW protons.

From the above arguments a fully hydrodynamical description of the SW-LISM should accurately capture the SW proton state and the subsequent heliosphere forming due to its interaction with the LISM (which together with accurate PUI densities are exactly the requirements that such a model should satisfy within the context of cosmic ray modulation). If a hydrodynamical approach is not followed, the SW-LISM interaction needs to be calculated kinetically. This is the approach followed by *Baranov and Malama* (1993) and involves calculating a solution to the full Boltzmann equation together with the relevant collision integrals. An alternative approach is followed by *Zank et al.* (1996) where the neutral hydrogen species is divided into three distinct populations, each described by a separate set of hydrodynamical equations.

In this work a simpler hydrodynamical formulation will be used, similar to the model developed by *Pauls et al.* (1995). The model used here derives from the model developed by *Fahr et al.* (2000) which uses different source terms coupling the different particle species (specifically regarding the energy transfer between hydrogen atoms and protons). The model by *Fahr et al.* (2000) also uses a different numerical algorithm (based on the formalism in Chapter 2) to solve the set of coupled hydrodynamical equations. Lastly the mass conservation equation for PUI's is solved in the *Fahr et al.* (2000) model, providing results explicitly showing their abundance throughout the heliosphere.

In the next section the source terms coupling the different particle species in a hydrodynamical context are listed. Using these source terms numerical results will be obtained showing the influence of neutral atoms on the heliospheric structure. In a later section a parameter study will be presented to study the effect different assumed SW and LISM states have on the heliosphere. These results will also be compared to a similar study by *Müller et al.* (2006) where the model developed by *Zank et al.* (1996) is used. It will be shown that the results from the hydrodynamical approach followed in this work correspond to the results derived from the *Zank et al.* (1996) model and that these results describe the heliosphere with sufficient accuracy to be useful in the context of cosmic ray modulation.

4.3 Hydrodynamical modelling of the multi species heliosphere

In the framework of hydrodynamics both the SW-LISM protons and the LISM neutral hydrogen population are described by a set of Euler-equations similar to Eqs.(2.92), (2.93) and (2.94) with the addition of source terms affecting the coupling between the different particle species. Therefore, each species is described by

$$\frac{\partial \rho_i}{\partial t} + \nabla \cdot (\rho_i \mathbf{v}_i) = S_{i,\rho} \tag{4.5}$$

$$\frac{\partial}{\partial t}(\rho_i \mathbf{v}_i) + \nabla \cdot (\rho_i \mathbf{v}_i \otimes \mathbf{v}_i) + \nabla P_i = \mathbf{S}_{i,\mathbf{v}} \tag{4.6}$$

$$\frac{\partial E_i}{\partial t} + \nabla \cdot \left(\mathbf{v}_i \left(\frac{\gamma P_i}{\gamma - 1} + \frac{1}{2}\rho_i v_i^2 \right) \right) = S_{i,E} \tag{4.7}$$

where $i = p$ denotes the proton species and $i = H$ denotes the neutral hydrogen species. Since the PUI velocity distribution is not Maxwellian (see Eq.4.4) only the mass conservation equation will be solved for PUI's, together with an appropriate source term $S_{PUI,\rho}$. The source functions $S_{i,\rho}$, $\mathbf{S}_{i,\mathbf{u}}$ and $S_{i,E}$ are calculated by taking into account the production and loss rates of particles due to charge exchange, photoionisation and electron impact ionisation and the subsequent gains or losses in mass, momentum and energy. These rates are listed below and taken from *Kausch* (1998) and *Fahr et al.* (2000).

For charge exchange the frequency with which new protons are created (or hydrogen atoms are lost) is given by

$$\nu_{CE}^{H \rightarrow P} = \sigma_{CE} v_{rel} n_p \tag{4.8}$$

while the production frequency for hydrogen atoms (equal to the loss rate of protons) is given by

$$\nu_{CE}^{P\rightarrow H} = \sigma_{CE} v_{rel} n_H \tag{4.9}$$

where the charge exchange cross section is taken from *Fite et al.* (1962) as

$$\sigma_{CE} = \left(2.1 \times 10^{-7} - 9.2 \times 10^{-9} \ln\left(v_{rel}\right)\right)^2 \mathrm{cm}^2. \tag{4.10}$$

This is the charge exchange cross section shown in Fig.(4.1). The relative velocity v_{rel} is taken from *Holzer* (1972) as

$$v_{rel} = \sqrt{\frac{128 k_b}{9\pi m_p}\left(T_p + T_H\right) + \left(\mathbf{v}_p - \mathbf{v}_H\right)\cdot\left(\mathbf{v}_p - \mathbf{v}_H\right)} \tag{4.11}$$

where T_p and T_H are the temperatures of the proton and hydrogen species respectively.

Photoionisation occurs as a neutral atom is ionized by sufficiently energetic incident radiation. In the context of the heliosphere it is assumed that the only source of sufficiently energetic radiation is the Sun. The photoionisation frequency (resulting in a loss of neutrals and a production of protons) is given by

$$\nu_{PI}^{H\rightarrow P} = \alpha \frac{r_0^2}{r^2} \tag{4.12}$$

where r is the radial heliocentric position, $\alpha = 8 \times 10^{-8}\ \mathrm{s}^{-1}$ is constant and $r_0 = 1$ AU. Since the photoionisation frequency is inversely proportional to r^2 it is expected that it will only have significance close to the Sun.

Electron impact ionisation leads to the production of protons from neutral hydrogen atoms (provided that the incident electron has an energy larger than the ionisation energy of hydrogen) at a frequency of

$$\nu_{EI}^{H\rightarrow P} = \sigma_{EI} v_{e,rel} n_e \tag{4.13}$$

where it is assumed that the number of electrons and protons in the SW or LISM is approximately the same so that $n_e \approx n_p$. The relative velocity between the electrons and the neutral species is taken from *Fahr et al.* (2000) as

$$v_{e,rel} \sim \sqrt{\frac{m_e}{m_p}} v_{rel} \tag{4.14}$$

where v_{rel} is given in Eq.(4.2). The relevant cross section is taken from *Fahr et al.* (2000) as

$$\sigma_{EI} = 1 \times 10^{-17} \frac{a + b v_{rel,e}}{1 + v_{rel,e}\left(c + d v_{rel,e}\right)} \quad \text{for} \quad \frac{1}{2} m_e v_{rel,e}^2 > 13.6\ \mathrm{eV} \tag{4.15}$$

with

$$\begin{aligned} a &= -16.708177 \\ b &= 1.232277 \\ c &= 6.8078 \times 10^{-2} \\ d &= 9.5 \times 10^{-4}. \end{aligned} \tag{4.16}$$

σ_{EI} is shown in Fig.(4.1). From the above production and loss rates the source terms in Eqs.(4.5), (4.6) and (4.7) can be calculated.

For $S_{p,\rho}$ and $S_{H,\rho}$ it is noted that for charge exchange the number of protons lost by the proton species is exactly equal to the number of protons gained from the neutral population. Similarly the neutral population does not experience a decrease in number density due to charge exchange interactions. Photoionisation and electron impact ionisation do, however, result in a net loss of hydrogen atoms and a net gain of protons. Therefore, the $S_{p,\rho}$ and $S_{H,\rho}$ source terms may be written as

$$S_{p,\rho} = \left(\nu_{PI}^{H\rightarrow P} + \nu_{EI}^{H\rightarrow P}\right)\rho_H \quad S_{H,\rho} = -\left(\nu_{PI}^{H\rightarrow P} + \nu_{EI}^{H\rightarrow P}\right)\rho_H. \tag{4.17}$$

In Chapter 2 it was shown that the numerical calculation used to update the system between timesteps is done in three phases. During the first two phases the change in a volume averaged quantity due fluxes into and out of a certain volume is calculated. During the third step contributions from source or loss terms are taken into account. Therefore, during this last phase, the total change in a certain cell averaged quantity is given by the total production or loss rate of that quantity. This allows for the hydrogen mass conservation equation to be written in terms of the total time derivitave as

$$\frac{d\rho_H}{dt} = -\left(\nu_{PI}^{H\rightarrow P} + \nu_{EI}^{H\rightarrow P}\right)\rho_H. \tag{4.18}$$

The amount of hydrogen $\Delta\rho_H$ lost in a time $\Delta t = t_1 - t_0$ is obtained by integrating over time so that

$$\rho_H = \rho_{H,0} e^{-(\nu_{PI}^{H\rightarrow P} + \nu_{EI}^{H\rightarrow P})\Delta t} \tag{4.19}$$

where $\rho_{H,0}$ is the hydrogen density at time $t = t_0$. Since the number of neutrals lost due to photoionisation and electron impact ionisation is equal to the number of protons gained it follows that

$$\Delta\rho_p = \rho_{H,0} - \rho_{H,0} e^{-(\nu_{PI}^{H\rightarrow P} + \nu_{EI}^{H\rightarrow P})\Delta t}. \tag{4.20}$$

If it is assumed that ρ_H and ρ_p are cell averaged quantities (in the context of Chapter 2) Eqs.(4.19) and (4.20) give the cell averaged gain or loss in ρ_H and ρ_p during a single time step and are readilly implemented in Eq.(2.91).

Charge exchange between a neutral atom with velocity $\mathbf{v}_H$ and a proton with velocity $\mathbf{v}_p$ results in the proton species acquiring momentum proportional to $\mathbf{v}_H$ and losing momentum proportional to $\mathbf{v}_p$. If protons are added to the proton fluid at a rate of $\nu_{CE}^{H\rightarrow P}$ and removed at a rate of $\nu_{CE}^{P\rightarrow H}$ it follows that the momentum gain or loss due to charge exchange is given by

$$\mathbf{S}_{p,\mathbf{v},CE} = \nu_{CE}^{H\rightarrow P}\mathbf{v}_H - \nu_{CE}^{P\rightarrow H}\mathbf{v}_p = \frac{\sigma_{CE}}{m_p}\rho_p\rho_H v_{rel}\left(\mathbf{v}_H - \mathbf{v}_p\right). \tag{4.21}$$

In the context of Chapter 2, Eq.(4.21) needs to be rewritten as a gain or loss of a cell averaged quantity (in this case $\rho\mathbf{v}_p$) over a time interval Δt. By noting that

$$\frac{d}{dt}\left(\rho_p\mathbf{v}_p\right) = \mathbf{S}_{p,\mathbf{v},CE} \simeq \frac{\Delta\left(\rho_p\mathbf{v}_p\right)}{\Delta t} \tag{4.22}$$

it follows that

$$\Delta\left(\rho_p\mathbf{v}_p\right) \simeq \frac{\sigma_{CE}}{m_p}\rho_p\rho_H v_{rel}\left(\mathbf{v}_H - \mathbf{v}_p\right)\Delta t \tag{4.23}$$

which is readilly useable in Eq.(2.91) as the gain or loss in momentum as a result of charge exchange. Regarding photoionisation and electron impact ionisation it is assumed that the newly created protons are immediately convected with the proton bulk velocity and, therefore, yield the momentum source function

$$\mathbf{S}_{p,\mathbf{v},PI,EI} = \mathbf{v}_p\rho_H\left(\nu_{PI}^{H\rightarrow P} + \nu_{EI}^{H\rightarrow P}\right) \tag{4.24}$$

which is just the number of protons produced per unit volume per unit time (through photoionisation and electron impact ionisation) multiplied by their velocity. Similar to the procedure used to obtain Eq.(4.23) the gain in momentum during a time step Δt due to electron impact and photoionisation is

$$\Delta\left(\rho_p\mathbf{v}_p\right) = \mathbf{v}_p\rho_H\left(\nu_{PI}^{H\rightarrow P} + \nu_{EI}^{H\rightarrow P}\right)\Delta t. \tag{4.25}$$

For the energy source term $S_{p,E}$ resulting from charge exchange the result from *McNutt et al.* (1998) is used (the momentum source term derived therein is identical to the one in Eq.4.21). In *McNutt et al.* (1998) the momentum and energy source terms are calculated from the Boltzmann collision integrals resulting from charge exchange between protons and neutral atoms, where both species can be initially described by Maxwellian distribution functions with different bulk characteristics. The energy source term $S_{p,E}$ is

$$S_{p,E} = \frac{\sigma_{CE}}{m_p}\left[2v^*_{rel}\left(\rho_p P_H - \rho_H P_p\right) + \frac{1}{2}\rho_p \rho_H v_{rel}\left(v_H^2 - u_p^2\right)\right] \tag{4.26}$$

where σ_{CE} is evaluated at v_{rel} and

$$v^*_{rel} = \sqrt{\frac{8k_b}{9\pi m_p}\left(T_p + T_H\right) + \left(\mathbf{v}_p - \mathbf{v}_H\right)\cdot\left(\mathbf{v}_p - \mathbf{v}_H\right)}. \tag{4.27}$$

Similar to the procedure used to obtain Eq.(4.23) the gain or loss of energy experienced by the proton fluid during a time interval Δt is

$$\Delta E \simeq \frac{\sigma_{CE}}{m_p}\left[2v^*_{rel}\left(\rho_p P_H - \rho_H P_p\right) + \frac{1}{2}\rho_p \rho_H v_{rel}\left(v_H^2 - u_p^2\right)\right]\Delta t. \tag{4.28}$$

The momentum and energy source terms for the neutral hydrogen population are listed from *Kausch* (1998) and *Fahr et al.* (2000) as

$$\begin{aligned}
\mathbf{S}_{H,\mathbf{v}} &= -\left(\nu_{PI}^{H\to P} + \nu_{EI}^{H\to P}\right)\rho_H \mathbf{v}_H - \tfrac{\sigma_{CE}}{m_p}\rho_p \rho_H v_{rel}\left(\mathbf{v}_H - \mathbf{v}_p\right) \\
S_{H,E} &= -\left(\nu_{PI}^{H\to P} + \nu_{EI}^{H\to P}\right)\rho_H E_H - \tfrac{\sigma_{CE}}{m_p}\rho_p\left(E_H - \tfrac{\rho_H}{\rho_p}E_p\right).
\end{aligned} \tag{4.29}$$

Lastly the PUI density can be calculated from the conservation of mass. Using Eq.(4.3) it is assumed that all PUI's are eventually accelerated to the bulk SW velocity. This allows for the mass conservation equation

$$\frac{\partial \rho_{PUI}}{\partial t} + \nabla\cdot\left(\rho_{PUI}\mathbf{v}_p\right) = S_{PUI,\rho} \tag{4.30}$$

to be solved where $S_{PUI,\rho}$ is given by

$$S_{PUI,\rho} = \left(\nu_{PI}^{H\to P} + \nu_{EI}^{H\to P} + \nu_{CE}^{H\to P}\right)\rho_H. \tag{4.31}$$

By separating the contributions from charge exchange and photoionisation together with electron impact ionisation it follows that the gain in PUI's from charge exchange is

$$\Delta\rho_{PUI,CE} = \nu_{CE}^{H\to P}\rho_H \Delta t. \tag{4.32}$$

The gain in PUI's due to photoionisation and electron impact ionisation is given by

$$\Delta\rho_{PUI,PI,EI} = \rho_{PUI,0}e^{\left(\nu_{PI}^{H\to P} + \nu_{EI}^{H\to P}\right)\Delta t}. \tag{4.33}$$

The source terms listed above are used to calculate the SW-LISM interaction numerically. The results of this calculation are given in the next section. For the rest of this work the effects of

Parameter	Value
$n_{p,LISM}$	0.1 cm^{-3}
$n_{H,LISM}$	0.1 cm^{-3}
$\mathbf{v}_{p,LISM}$	$(-26$ km.s$^{-1})\hat{\mathbf{x}}$
$\mathbf{v}_{H,LISM}$	$(-26$ km.s$^{-1})\hat{\mathbf{x}}$
$T_{p,LISM}$	8000 K
$T_{H,LISM}$	8000 K
$n_{p,SW}$	5.0 cm^{-3}
$\mathbf{v}_{p,SW}$	$(400$ km.s$^{-1})\hat{\mathbf{r}}$
$T_{p,SW}$	10^5 K

Table 4.1: The assumed initial states of the SW and LISM.

photoionisation will only be taken into account in the inner heliosphere since $\nu_{PI}^{H\rightarrow P}$ decreases rapidly with increasing heliocentric distance. Electron impact ionisation will only be taken into account in the inner heliosheath since it is the only region where electrons may obtain sufficient thermal energies to ionize neutral hydrogen (see *Zank*, 1999; *Fahr et al.*, 2000). Between the HP and BS only charge exchange interactions will be taken into account since this region is too far away from the Sun for photoionisation to be significant and to cold for electron impact ionisation to play any significant role (as can be seen from Fig.4.1).

4.4 The three species heliosphere

Using the source terms from the previous section together with the numerical formulation in Chapter 2 the heliosphere is calculated by including the mutual effects of LISM neutrals on the proton populations in the SW and LISM. An initial condition is calculated using the grid shown in Fig.(2.4). Initially each cell in Fig.(2.4) is assigned the same value for the neutral hydrogen density, velocity and pressure. It is assumed that the neutral hydrogen velocity in each cell is parallel to the negative x-direction. All cells within a certain radius r_d are assigned a proton density, velocity and pressure consistent with adiabatic expansion of the SW. It is assumed that this initial expansion of the SW is purely radial. All the cells outside this radius are assigned the same proton density, velocity and pressure consistent with the LISM 'blowing over' the Sun-centred system. This implies that in each cell outside r_d the proton velocity is assumed to be parallel to the negative x-direction.

The values used are listed in Table 4.1, where $\hat{\mathbf{x}}$ and $\hat{\mathbf{r}}$ are unit vectors in the x and r directions (shown in Fig.2.4) respectively. This initial state is evolved in time according to the numerical scheme discussed in Chapter 2 until a steady state is reached.

Fig.(4.2) shows the total proton density (the sum of original SW protons and newly created PUI's) in the plane defined by Fig.(2.4). This plane corresponds to any plane axially symmetric about the LISM flow direction also containing the Sun. Comparison with Fig.(3.4) shows that much of the heliospheric structure is similar to the 'protons only' case from Chapter 3. For the initial values in Table 4.1 (comparable to the reference model from section 3.5) the SW-LISM interaction still produces three interfaces, namely the TS, HP and BS. It can be seen

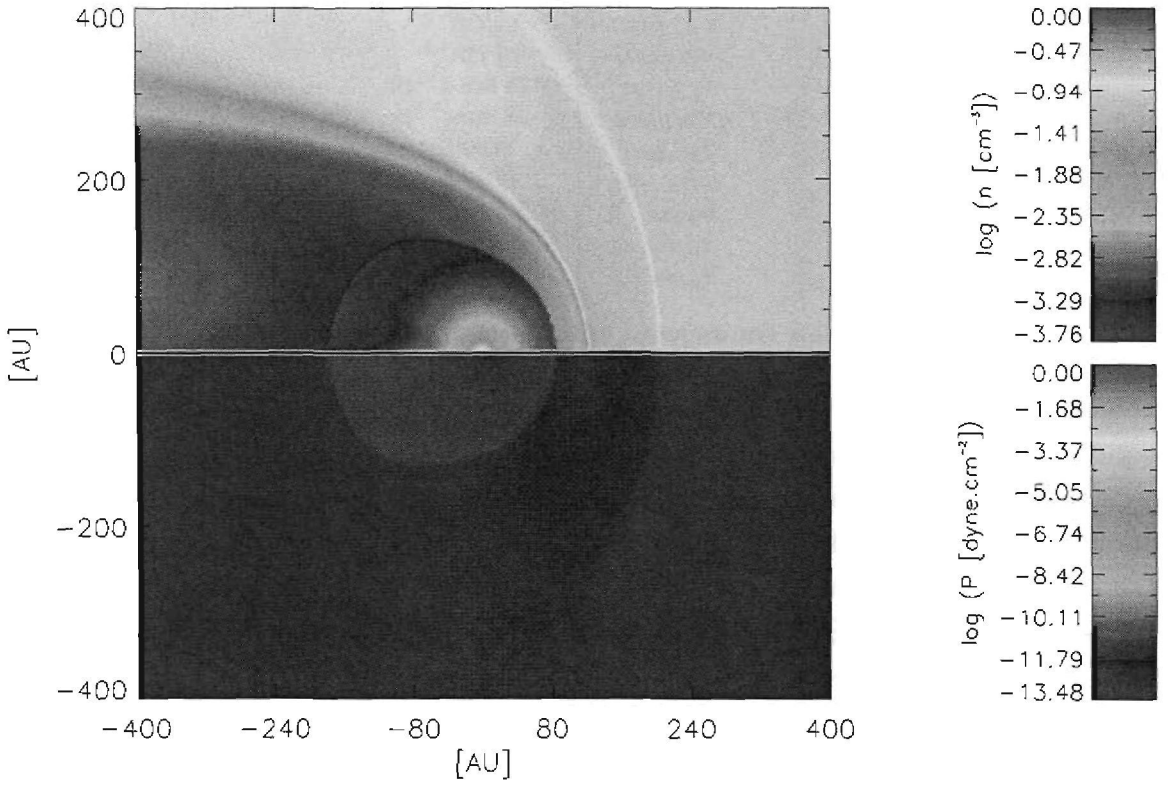

Figure 4.2: The proton number density (top) and pressure (bottom) in a plane parallel to the LISM inflow direction, containing the Sun at the origin. Results are calculated from a model taking into account the mutual interaction between protons, neutral hydrogen and PUI's. In the inner heliosphere and inner heliosheath the proton species consists of both SW protons and PUI's.

that the HP expands from a discontinuous separation between the shocked SW and LISM in the nose (where the separation is well defined) to a transition region as the polar regions are approached (where the region of separation becomes broader). As with the 'protons only' case these interfaces define four distinct regions. These are the inner heliosphere between the Sun and TS, the inner heliosheath between the TS and HP, the outer heliosheath between the HP and BS and the undisturbed LISM beyond the BS. Similar to the 'protons only' case Fig.(4.2) suggests that as the SW expands its density decreases with increasing heliocentric distance even though photoionisation causes a gain in protons in this region. As before the TS and BS correspond to jumps in density as the SW and LISM are compressed by the converging flows.

Shown in Fig.(4.3) is the radial and tangential velocity of the total proton species in the plane of Fig.(2.4). Comparing Fig.(4.3) with Fig.(3.5) shows that much of the characteristics of the 'protons only' heliosphere are retained even though neutral atoms interact with SW and LISM protons. The SW expansion in the inner heliosphere is still primarily radial. At the termination shock the radial density decreases immediately while significant tangential velocities are acquired as the HP is approached. As with the 'protons only' case the $-\nabla - P$ force acts to accelerate the protons between the TS and HP in the tangential direction. In the inner heliosheath this results in larger tangential velocities in the polar regions (compared to tangential velocities

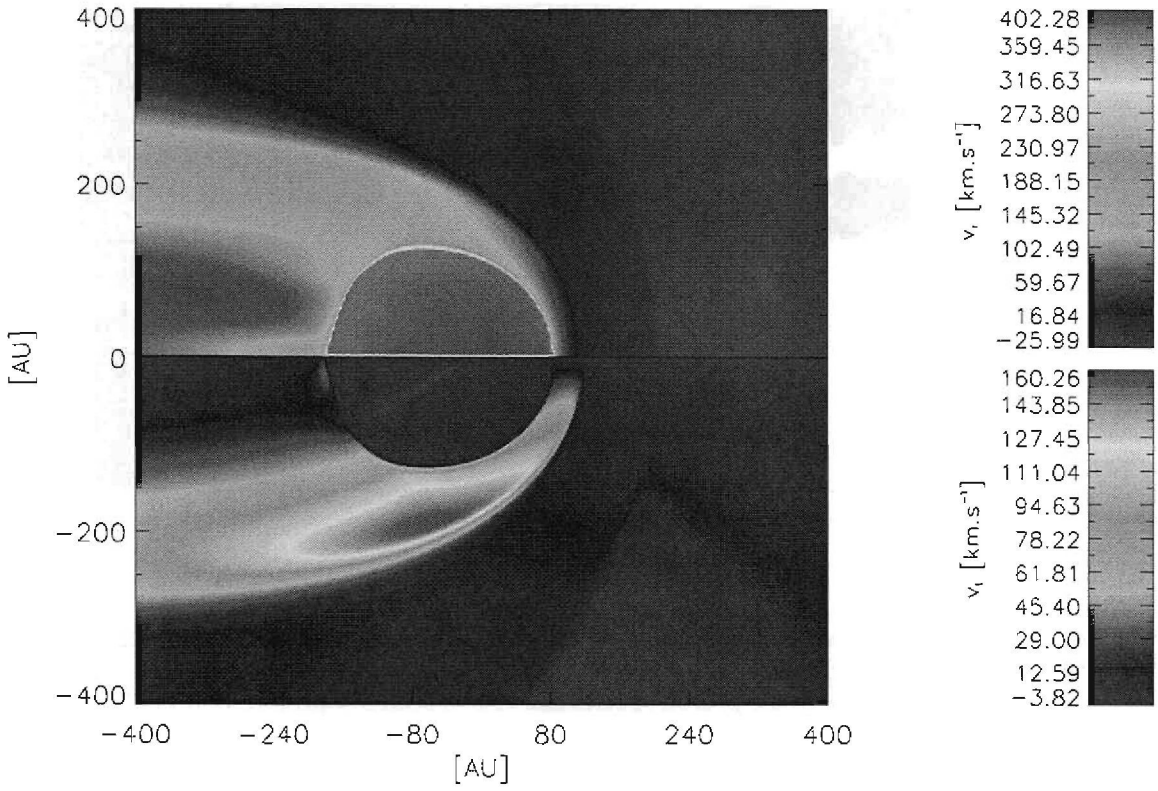

Figure 4.3: The proton radial (top) and tangential (bottom) velocity components (v_r and v_t) in a plane parallel to the LISM inflow direction, containing the Sun at the origin. Results are calculated from a numerical model taking into account the mutual interaction between protons, neutral hydrogen and PUI's. In the inner heliosphere and inner heliosheath the proton species consists of both SW protons and PUI's.

in the nose). The above results justify previous assertions that the proton-proton interaction between the SW and LISM dominates the characteristics of the heliosphere.

Fig.(4.4) shows regions of supersonic and subsonic proton flow calculated from the multi-species model in the plane of Fig.(2.4). Similar to the 'protons only' results the inner heliosphere is characterised by supersonic bulk velocities with the proton species transiting to a subsonic flow at the TS. Similarly the supersonic incoming LISM protons transit to subsonic velocities at the BS. The inner and outer heliosheath is primarily a region of subsonic flow except in the polar regions. As with the 'protons only' case the $-\nabla P$-force is effective enough to accelerate protons to supersonic velocities over the polar regions. Beyond the HP this implies that the shocked LISM proton velocity approaches the supersonic LISM inflow velocity close to the radial line defined by $\theta = 90^0$. Comparing Fig.(4.4) with Fig.(3.7) shows that for the multi-species case the supersonic region in the inner heliosheath is spatially distinct from the inner heliosphere which differs from the results calculated for the 'protons only' case.

Fig.(4.5) shows the hydrogen and PUI densities obtained for a steady state in the plane of Fig.(2.4). From Fig.(4.5) it can be seen that the hydrogen density is greatly enhanced in the

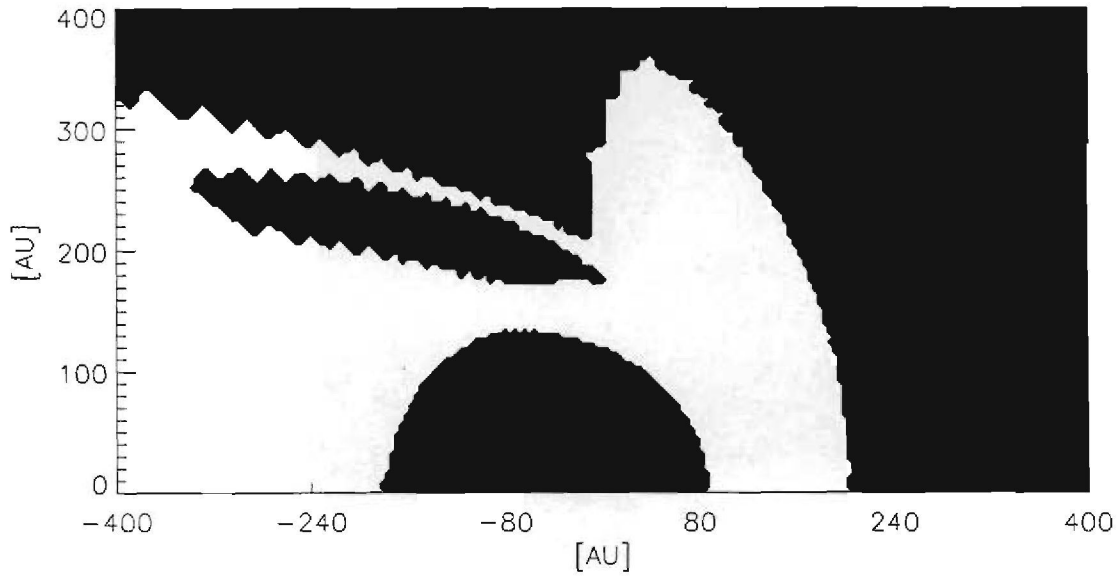

Figure 4.4: Regions of supersonic (black) and subsonic (white) proton flow as calculated from a model taking into account the mutual interaction between protons, neutral hydrogen and PUI's. In the inner heliosphere and inner heliosheath the proton species consists of both SW protons and PUI's.

outer heliosheath. This is the so-called hydrogen wall (see for example *Baranov and Malama*, 1993) forming as a consequence of charge exchange between slow moving subsonic protons and fast hydrogen atoms characterised by velocities similar to that of the undisturbed LISM. This interaction produces large quantities of slow moving hydrogen atoms to build up between the BS and HP. Although the description of the neutral hydrogen atoms are hydrodynamic Fig.(4.5) shows that this essential characteristic (hydrogen density enhancement between the HP and BS) of the hydrogen species is captured here.

In the inner heliosheath protons are decelerated radially as the HP is approached. These slow protons offer good targets for charge exchange interactions with incoming neutral atoms. Although the neutral atom density reaching the inner heliosheath is fairly lower than the LISM neutral density there are still enough neutrals present in the inner heliosheath to produce a significant amount of PUI's in the post-TS SW as shown in Fig.(4.5). It needs to be noted that PUI's are by definition ions picked-up by the SW. Since SW particles do not propagate past the HP in any appreciable quantity the mention of PUI's only makes sense between the Sun and TS, and in the inner heliosheath. In the outer heliosheath no distinction is made between protons initially from the LISM and those created through charge exchange.

In the inner heliosphere it can be seen that most PUI's are produced close to the Sun due to a combination of factors. Close to the Sun the proton density is highest which increases the number of charge exchange collisions per unit time per unit volume. Furthermore, the photoionisation rate (Eq.4.12) decreases proportional to r^{-2} which implies that close to the Sun photoionisation is most effective, further enhancing PUI production in this region. This is consistent with the discussion in section 4.2.

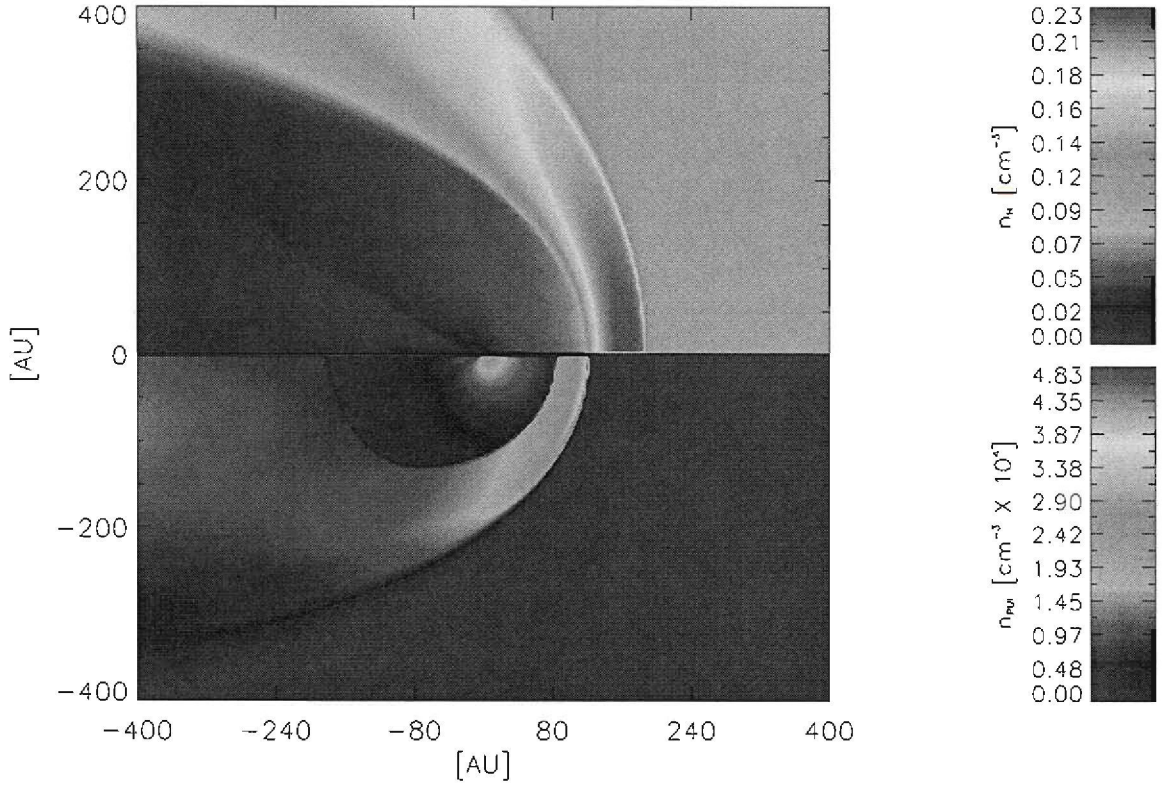

Figure 4.5: The neutral hydrogen (top) and PUI (bottom) number density at different heliocentric positions as calculated from a model taking into account the mutual interaction between protons, neutral hydrogen and PUI's.

The differences between the 'protons only' and multi-species heliospheres are best illustrated in Fig.(4.6). Shown in Fig.(4.6) are the density, pressure, radial and tangential velocity along different radial paths calculated for the total proton species for both the 'protons only' and multi-species cases. Also shown in the density plot are the hydrogen and PUI densities along the same radial paths. Immediately visible from Fig.(4.6) is that the TS, HP and BS form closer to the Sun if neutrals are included in the SW-LISM interaction, compared to the 'protons only' case calculated from similar initial SW and LISM states. This can be explained by using the parameter study from section 3.5 as a guide. In section 3.5 it is shown that decreasing the dynamic pressure ($\rho_p v_p^2$) associated with the SW causes the TS, HP and BS to form closer to the Sun. Visible in Fig.(4.6) is that the SW velocity decreases between the Sun and TS. This is in contrast to the 'protons only' case where the SW velocity is constant over this region. The decrease in SW velocity causes the dynamic pressure associated with the SW to drop. The reduced dynamic pressure in the SW subsequently causes the TS, HP and BS to form closer to the Sun.

The decrease in SW velocity between the Sun and TS can be attributed to charge exchange between slow moving hydrogen atoms (propagating into the inner heliosphere) and the faster moving SW protons. From Eq.(4.21) it can be seen that if the neutral hydrogen velocity is less

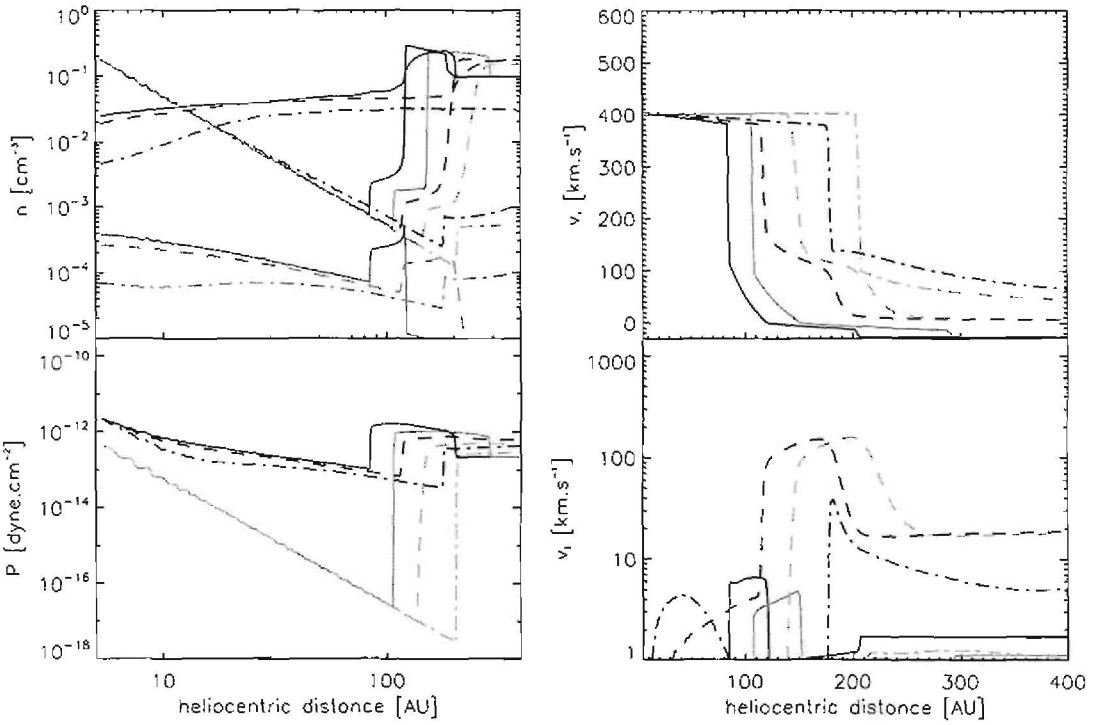

Figure 4.6: Radial profiles along the nose (solid lines) poles (dashed lines) and tail (dash-dotted lines) showing the total proton (black), hydrogen (blue) and PUI (green) number densities (top left panel), the proton radial and tangential velocities (top and bottom right panels) and the proton pressure (bottom left panel). The same proton profiles for the one fluid case from Chapter 3 are shown in yellow. Between the Sun and the TS and in the inner heliosheath the proton species consists of both SW protons and PUI's.

than the proton velocity charge exchange results in a net loss of momentum by the proton species. Furthermore, it can be seen from Eq.(4.21) that if the proton and hydrogen velocities are not parallel charge exchange can induce small deviations in the flow direction of the proton species. In Fig.(4.6) it can be seen that in the polar and tail regions the SW proton species obtains small tangential velocity components between the Sun and TS due to charge exchange with incoming neutral hydrogen atoms.

Shown in Fig.(4.6) are profiles of the total proton density, the PUI density and hydrogen density along different radial paths in the nose, polar region and tail. In the nose and polar regions it can be seen that the total proton density remains approximately proportional to r^{-2} between the Sun and TS, similar to the 'protons only' case. This implies that throughout the heliosphere the proton density is dominated by the contribution from SW protons since the number of newly created PUI's are not sufficient to enhance the density significantly.

In the inner heliosheath the proton density profiles in the nose and tail differ remarkably from the same profiles for the 'protons only' case. Whereas for the latter the proton density remained approximately constant beyond the TS it can be seen in Fig.(4.6) that the inclusion of neutral atoms causes a significant enhancement of in the proton density in this region. Furthermore, looking at the velocity profiles in Fig.(4.6) it can be seen that the inclusion of neutral atoms in

the SW-LISM interaction act to enhance the deceleration of protons beyond the TS. From the conservation of mass in one dimension, where the SW and LISM flows are parallel or anti-parallel (so that tangential components can be ignored), and no source terms are present it follows that

$$\rho_p v_p = \frac{K}{r^2} \tag{4.34}$$

where v_p is the magnitude of the one-dimensional radial velocity and K is a constant. From the discussion in section 3.4 it is expected for a subsonic flow that ρ_p will be constant and $v_p \propto r^{-2}$. If it is assumed that the density is not enhanced due to photoionisation or electron impact ionisation (as seems to be the case from Fig.4.1) the momentum loss experienced by the proton species can be implicitly included in Eq.(4.34) by letting

$$v_p = \frac{K_v}{r^2} - \zeta(r) \text{ for } r_{TS} < r < r_{HP} \tag{4.35}$$

where $\zeta(r)$ approximates the velocity lost due to charge exchange between fast protons and slow hydrogen atoms and K_v is a constant. Since charge exchange enhances the deceleration of protons between the TS and HP it follows that $\zeta(r) > 0$ and that $\zeta(r)$ increases with increasing radial distance. Substitution into Eq.(4.34) yields

$$\rho_p = \frac{K}{K_v - r^2\zeta(r)} \text{ for } r_{TS} < r < r_{HP}. \tag{4.36}$$

For $\zeta(r) \rightarrow 0$ Eq.(4.36) reduces to Eq.(4.34). The velocity in the inner heliosheath is positive everywhere. This implies that

$$\frac{K_v}{r^2} - \zeta(r) > 0 \text{ for } r_{TS} < r < r_{HP} \tag{4.37}$$

where r_{TS} and r_{HP} are the radial positions of the TS and HP respectively. In the tail it is assumed that r_{HP} approaches infinity. Subsequently $K_v > r^2\zeta(r)$ for $r_{TS} < r < r_{HP}$. Since $\zeta(r)$ increases with increasing radial distance and has to be less than K_v for $r_{TS} < r < r_{HP}$ the denominator in Eq.(4.36) becomes progressively smaller with increasing radial distance between the TS and HP. This in turn causes ρ_p to increase and accounts for the enhancement in ρ_p as the HP is approached in the nose (where the SW and LISM flow is approximately anti-parallel) and beyond the TS in the tail (where the SW and LISM flows are approximately parallel) . Similar density enhancements are to a lesser extent visible in the polar regions of the inner heliosheath.

Recall from section 3.4 that for the protons only case the pressure in the inner heliosphere is proportional to $r^{-10/3}$ since the inner heliosphere (where only SW and LISM protons are considered) is characterised by adiabatic expansion of the SW. Regarding the pressure profiles

shown in Fig.(4.6) it can be seen that the proton pressure in the inner heliosphere calculated for the multi-species model is proportional to $r^{-\alpha}$ where $\alpha < 10/3$ beyond approximately 10 AU. Therefore, the inclusion of neutral atoms acts to 'flatten' the pressure gradient between the Sun and TS. It will be shown that this flattening of the pressure gradient is consistent with heating of the SW due to the production of PUI's. For the 'protons only' case $P \propto r^{-10/3}$ leads to a temperature decrease (using the ideal gas law) of $T \propto r^{-4/3}$. The inclusion of neutral atoms, however, causes the proton pressure to decrease proportional to $r^{-\alpha}$ where $\alpha < 10/3$. For regions where $\alpha < 2$ it follows from the ideal gas law that the temperature will increase with radial distance, as shown in Fig.(4.7).

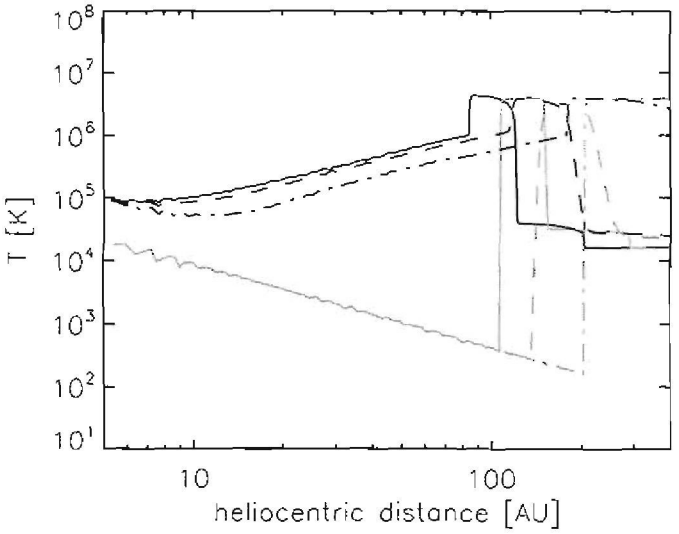

Figure 4.7: Radial profiles along the nose (solid lines), poles (dashed lines) and tail (dash-dotted lines) showing the temperature of the total proton species (consisting of both the SW protons and PUI's). The corresponding proton profiles for the one fluid case from Chapter 3 are shown in yellow.

Heating of the SW can be shown to occur using alternative approaches to the one presented here. It can be shown (see for example *Isenberg*, 2005) that heating of the SW occurs due to turbulence resulting from PUI production. Fig.(4.7) shows that this important consequence of PUI production is captured by the purely hydrodynamical formulation considered in this chapter. It should be noted however that the amount of heating is overestimated by the hydrodynamical model presented here (as can be seen from a direct comparison with the results from *Isenberg*, 2005).

From the results presented above the effect of neutral atoms on the SW-LISM interface can be summarised as follows: charge exchange with slower neutral atoms causes the bulk velocity of the SW proton species to decrease in the inner heliosphere and inner heliosheath. The proton density throughout most of the inner heliosphere remains unchanged since the number of PUI's created through photoionisation and electron impact ionisation (producing a net increase in density) is several orders smaller than the SW proton density. In the inner heliosheath, however, the proton deceleration induced by charge exchange with slow neutrals causes the

protons in this region to 'build-up' which in turn produces noticeable enhancements in the SW proton density beyond the TS. In the inner heliosphere the interaction between SW protons and incoming neutral atoms causes the pressure to decrease less with increasing radial distance (compared to the results where only protons are considered). Because the density in this region remains primarily unaltered this corresponds to heating of the SW as a consequence of PUI production.

Regarding the effect of neutral atoms on the SW-LISM interaction a parameter study is now presented along the same lines as in section 3.5. The purpose of this study is to gauge how the inclusion of neutral atoms affects the results from section 3.5, how the heliosphere reacts to different assumed states of the hydrogen carrying LISM and to compare the hydrodynamical treatment of neutral atoms as presented in section 4.3 with the different approach implicit in the results of *Müller et al.* (2006).

4.5 Response of the multi-species heliosphere to different boundary conditions

In this section a parameter study is presented to gauge the effect of neutral atoms on the geometry of, and plasma flow in the heliosphere as well as the response of the neutral modulated heliosphere to different boundary conditions. The results presented here will be compared to those already presented in section 3.5. The effect of different LISM neutral atom states on the heliosphere is also investigated. The chapter concludes by comparing results from this model with results calculated by *Müller et al.* (2006) using the model from *Zank et al.* (1996).

Regarding the discussion in section 3.2 it follows that a plausible range of parameters exist describing the SW and LISM proton states, as well as the state of the LISM neutral hydrogen atom population. Using the same method as discussed in the beginning of section 4.4 an initial condition is set up for a particular state of the SW and LISM (the latter now containing neutral atoms) and evolved in time until a steady state is reached. The parameters describing these different states are listed in Table 4.2 where model 1 will again be referred to as the 'standard model' and used as reference. The parameters in Table 4.2 follow from the discussion in section 3.2, analogous to the values listed in Table 3.2.

Shown in Figs.(4.8) and (4.9) are the radial positions of the TS, HP and BS for $\theta \in [0^0, 180^0]$ as calculated for all the models listed in Table 4.2. Figs.(4.10), (4.11), (4.12) and (4.13) show the proton (including PUI's), hydrogen and PUI densities as well as the magnitude of the radial proton (including PUI's) velocity and temperature along a radial path in the nose for each of the models listed in Table 4.2. Figs.(4.8) and (4.9) also show the geometry of the TS, HP and BS (in the sense that a position which is constant with respect to θ implies spherical symmetry) for the different models listed in Table 4.2.

Comparing Figs.(4.8) and (4.9) with Fig.(3.8) reveal that the inclusion of neutral atoms act to

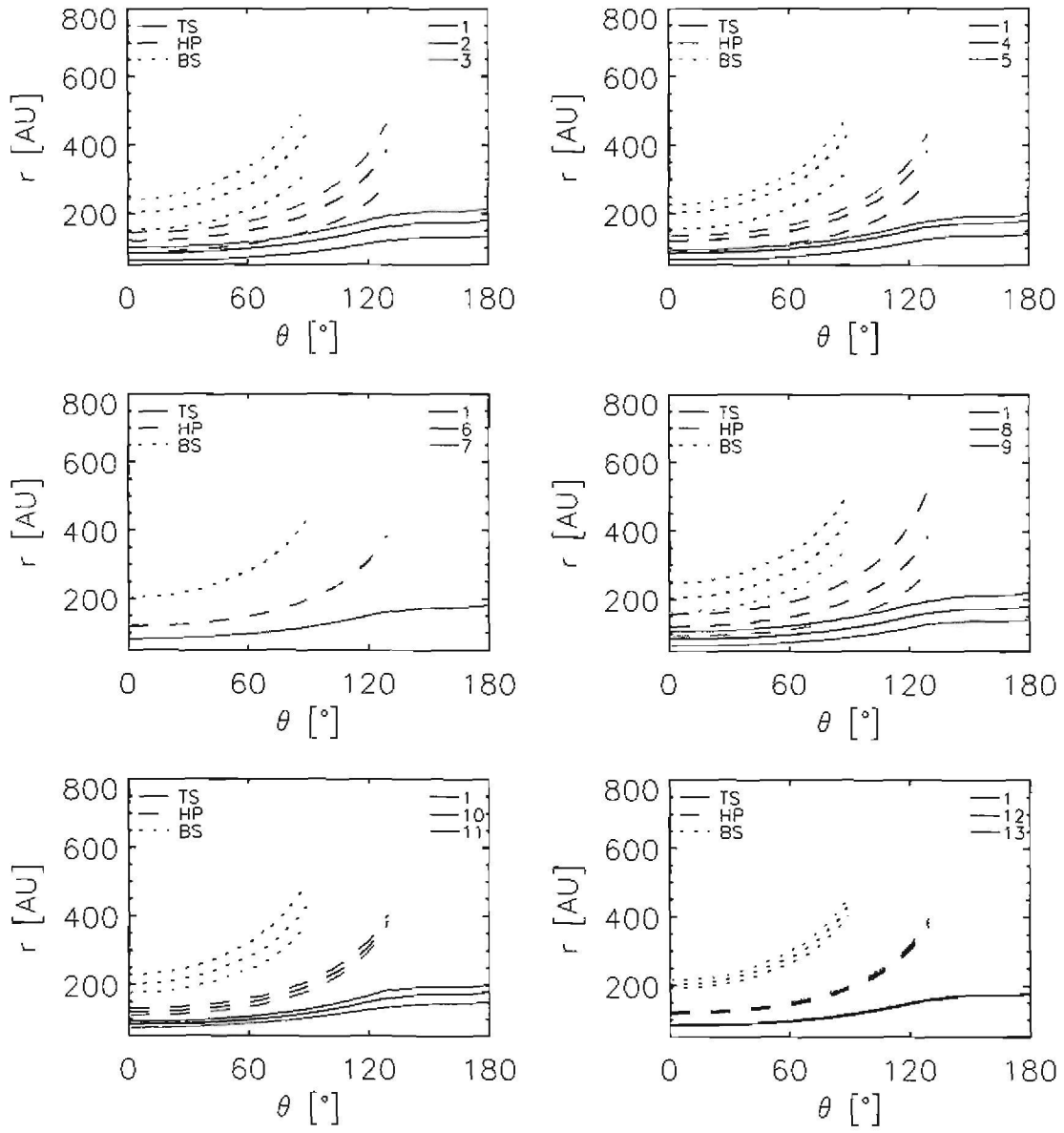

Figure 4.8: The radial position of the TS, HP and BS for $\theta \in [0^0, 180^0]$ for models 1 – 13 listed in Table.4.2. All of the results are calculated with the inclusion of neutral atoms and PUI's in the SW-LISM interaction.

Model	$n_{p,SW}$ (cm^{-3})	$v_{p,SW}$ ($km.s^{-1}$)	$T_{p,SW}$ (K)	$n_{p,LISM}$ (cm^{-3})	$n_{H,LISM}$ (cm^{-3})	$v_{p,LISM}$ ($km.s^{-1}$)	$T_{p,LISM}$ (K)	$T_{H,LISM}$ (K)
1	5.0	400.0	10^5	0.10	0.10	26.0	8000	8000
2	2.5	400.0	10^5	0.10	0.10	26.0	8000	8000
3	7.5	400.0	10^5	0.10	0.10	26.0	8000	8000
4	5.0	300.0	10^5	0.10	0.10	26.0	8000	8000
5	5.0	450.0	10^5	0.10	0.10	26.0	8000	8000
6	5.0	400.0	5×10^4	0.10	0.10	26.0	8000	8000
7	5.0	400.0	2×10^5	0.10	0.10	26.0	8000	8000
8	5.0	400.0	10^5	0.05	0.10	26.0	8000	8000
9	5.0	400.0	10^5	0.20	0.10	26.0	8000	8000
10	5.0	400.0	10^5	0.10	0.05	26.0	8000	8000
11	5.0	400.0	10^5	0.10	0.20	26.0	8000	8000
12	5.0	400.0	10^5	0.10	0.10	25.0	8000	8000
13	5.0	400.0	10^5	0.10	0.10	27.0	8000	8000
14	5.0	400.0	10^5	0.10	0.10	26.0	6000	6000
15	5.0	400.0	10^5	0.10	0.10	26.0	9000	9000
16	5.0	400.0	10^5	0.10	0.10	26.0	8000	6000
17	5.0	400.0	10^5	0.10	0.10	26.0	8000	9000

Table 4.2: Parameters used to calculate the SW-LISM interaction where the LISM consists of protons and neutral atoms.

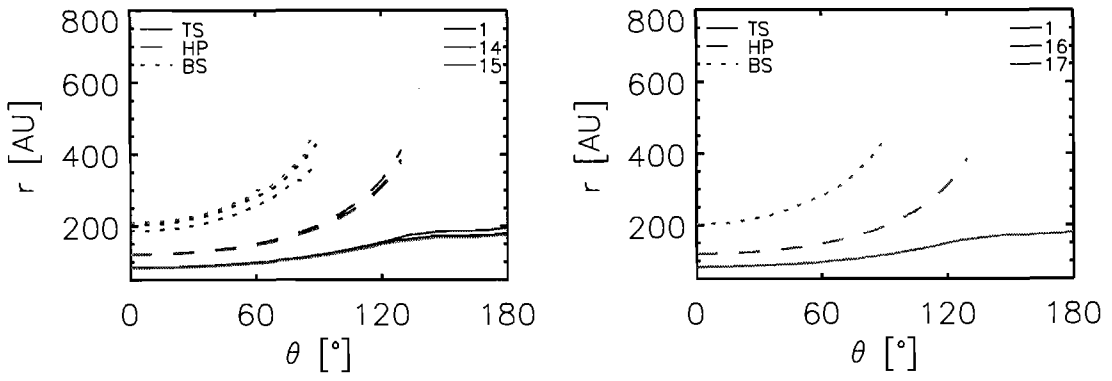

Figure 4.9: The radial position of the TS, HP and BS for $\theta \in [0^0, 180^0]$ for models $14 - 17$ listed in Table.4.2. All of the results are calculated with the inclusion of neutral atoms and PUI's in the SW-LISM interaction.

'smooth out' the TS profiles (most noticeable with the increased hydrogen density used in model 11) in the sense that the change in the TS position with changing θ becomes less pronounced. In Figs.(4.8) and (4.9) it is shown that the TS position (distance away from the Sun) increases steadily between the nose (at $\theta = 0^0$) and polar regions ($\theta = 90^0$). As the tail is approached from the polar region, the TS position profiles in Fig. (4.8) and (4.9) show a sharp departure from this smooth increase, visible as a 'knee' in the TS position profiles at $\sim 120^0$. Further comparison shows that the TS, HP and BS react differently to changes in boundary conditions when the mediating effect of neutrals are taken into account. The inclusion of neutral atoms smoothes out this 'knee' as is seen in Fig.(3.8).

From Figs.(4.8) it can be seen in the nose that decreasing the SW proton density by 50% (from 5.0 cm^{-3} to 2.5 cm^{-3}) results in the TS, HP and BS forming at distances 28%, 26% and 25% closer to the Sun. Increasing the SW density by 50% (from 5.0 cm^{-3} to 7.5 cm^{-3}) causes the same three interfaces to form 18% further out. In section 3.5 it was found that the TS, HP and BS formed $\sim$ 28% closer to the Sun when the SW proton density was decreased by 50% while a 50% increase caused these interfaces to form at radial distances which were $\sim$ 24% larger. Therefore, a 50% decrease in the SW proton density causes the TS, HP and BS to form approximately 28% closer to the Sun for both the multi species and 'protons only' cases. Increasing the SW proton density, however, causes the TS, HP and BS to form less further out (compared to their respective standard models) for the multi-species case than for the 'protons only' case. This is due to the momentum loss incurred by the proton species as a result of charge exchange with slow moving neutral atoms.

In the inner heliosphere enhancements in ρ_p due to charge exchange, photo and electron impact ionisation are negligible (as mentioned in the previous section). Since photo and electron impact ionisation effects are ignored beyond the BS the same goes for the supersonic LISM protons. It, therefore, follows that any decrease in the dynamic pressure (given by $\rho_p v_p^2$) is caused by deceleration of the proton species due to charge exchange. Reducing the SW proton density by 50% reduces the amount of momentum lost due to charge exchange (see Eq.4.21) by 50%. This implies that the effect of neutrals (slowing down the supersonic SW) for this case is 50% less significant and that this result should, therefore, show characteristics more similar to the 'protons only' case. This explains why the TS, HP and BS positions change (percentage wise) with similar magnitudes in the multi-species and 'protons only' cases when the SW proton density is decreased. Alternatively increasing the proton density by 50% enhances the effect of the source term in Eq.(4.21) by 50% implying that more momentum is lost due to charge exchange. The momentum lost effectively counteracts the enhancement in dynamic pressure that results from a higher proton density.

The above conclusion is also supported by the results in Fig.(4.10). Reducing the SW density causes the SW velocity in the inner heliosphere to decrease less with increasing radial distance. The hydrogen density in this region is higher than for the standard model because fewer photo and electron impact ionisation interactions take place. This also corresponds to a decreased

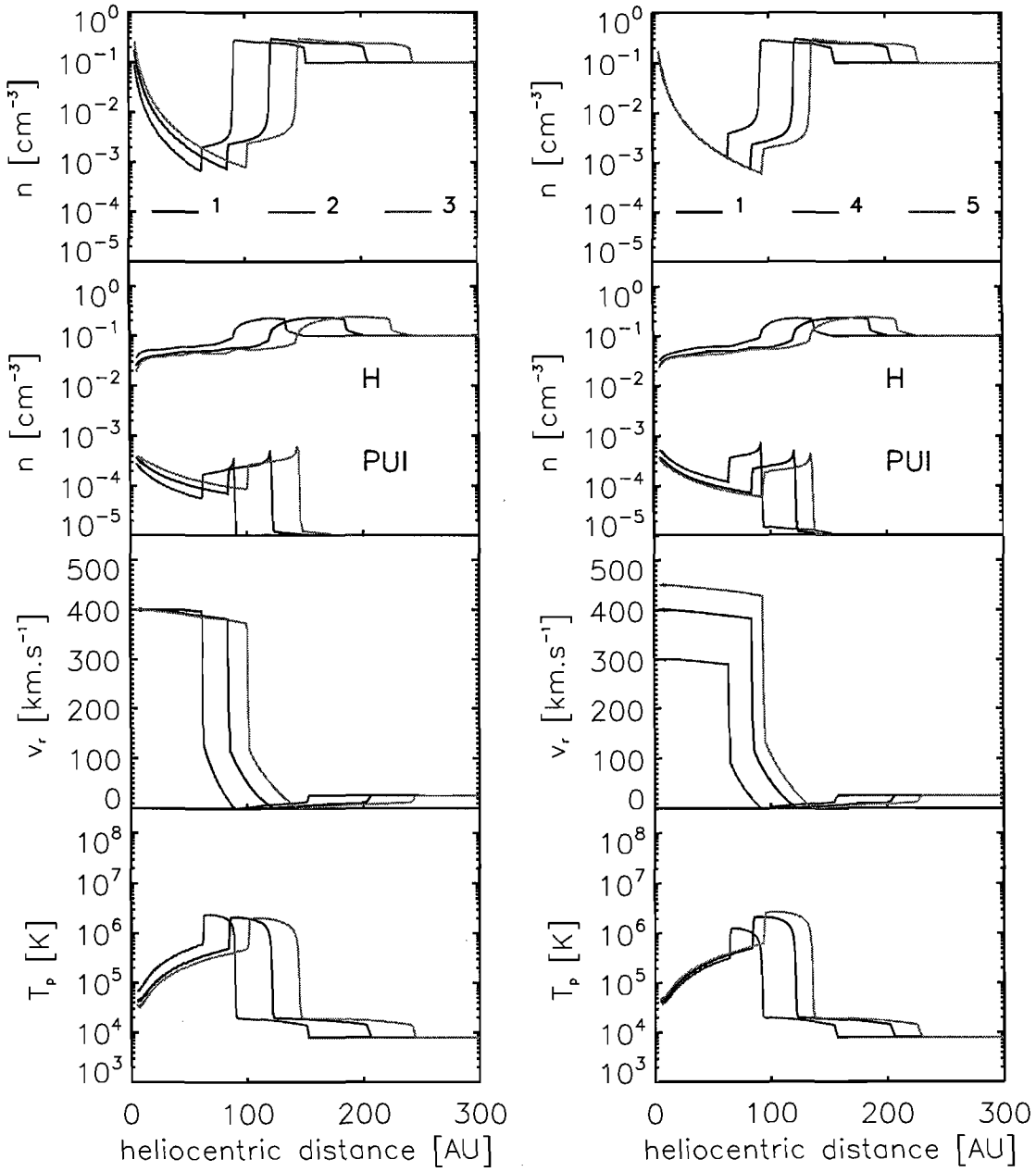

Figure 4.10: The proton (including PUI's), hydrogen and PUI densities as well as the magnitude of the radial proton (including PUI's) velocity and temperature along a radial path in the nose for each of the models 2 – 5 in Table 4.2 with model 1 used as reference.

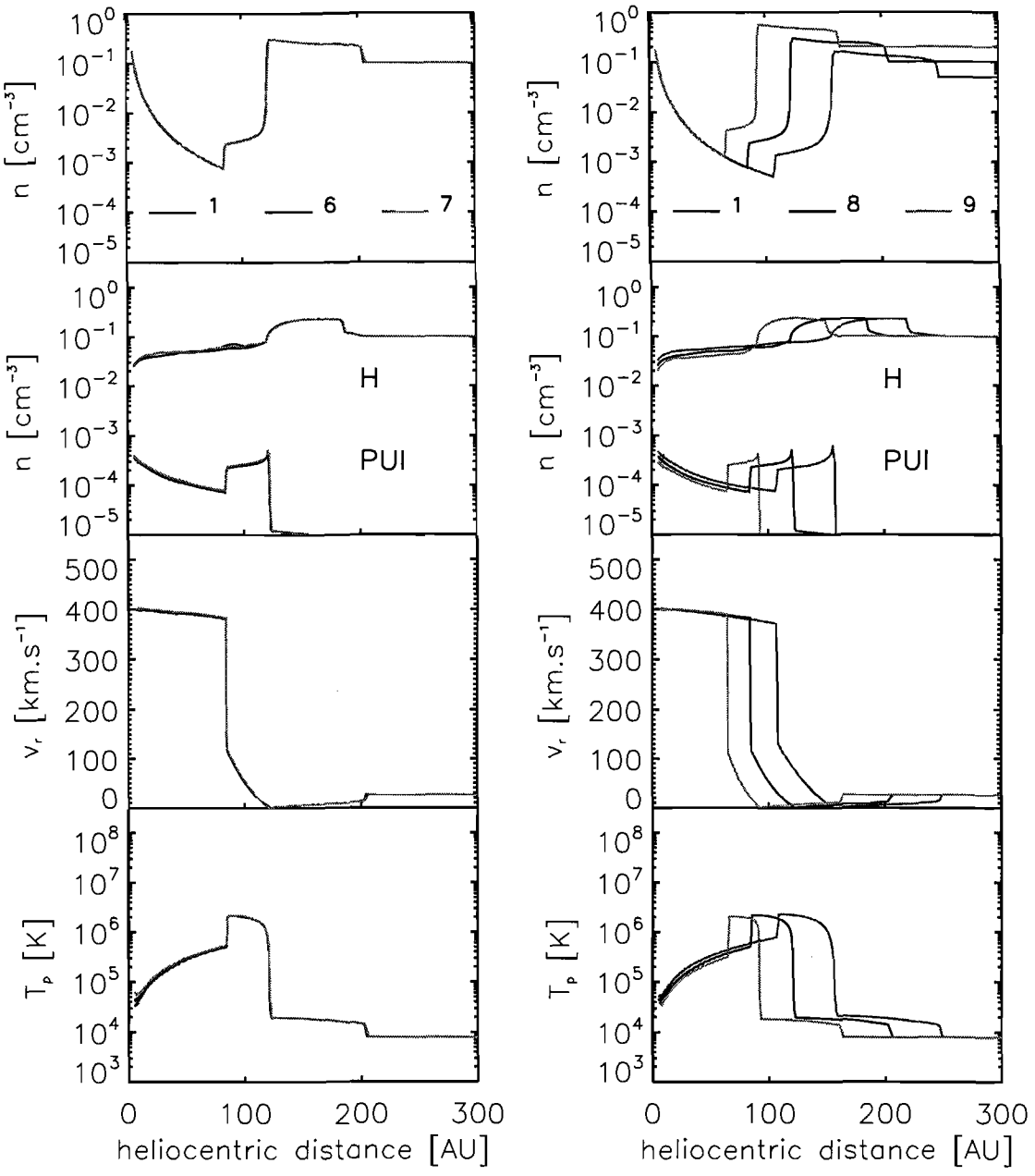

Figure 4.11: The proton (including PUI's), hydrogen and PUI densities as well as the magnitude of the radial proton (including PUI's) velocity and temperature along a radial path in the nose for each of the models 6 – 9 in Table 4.2 with model 1 used as reference.

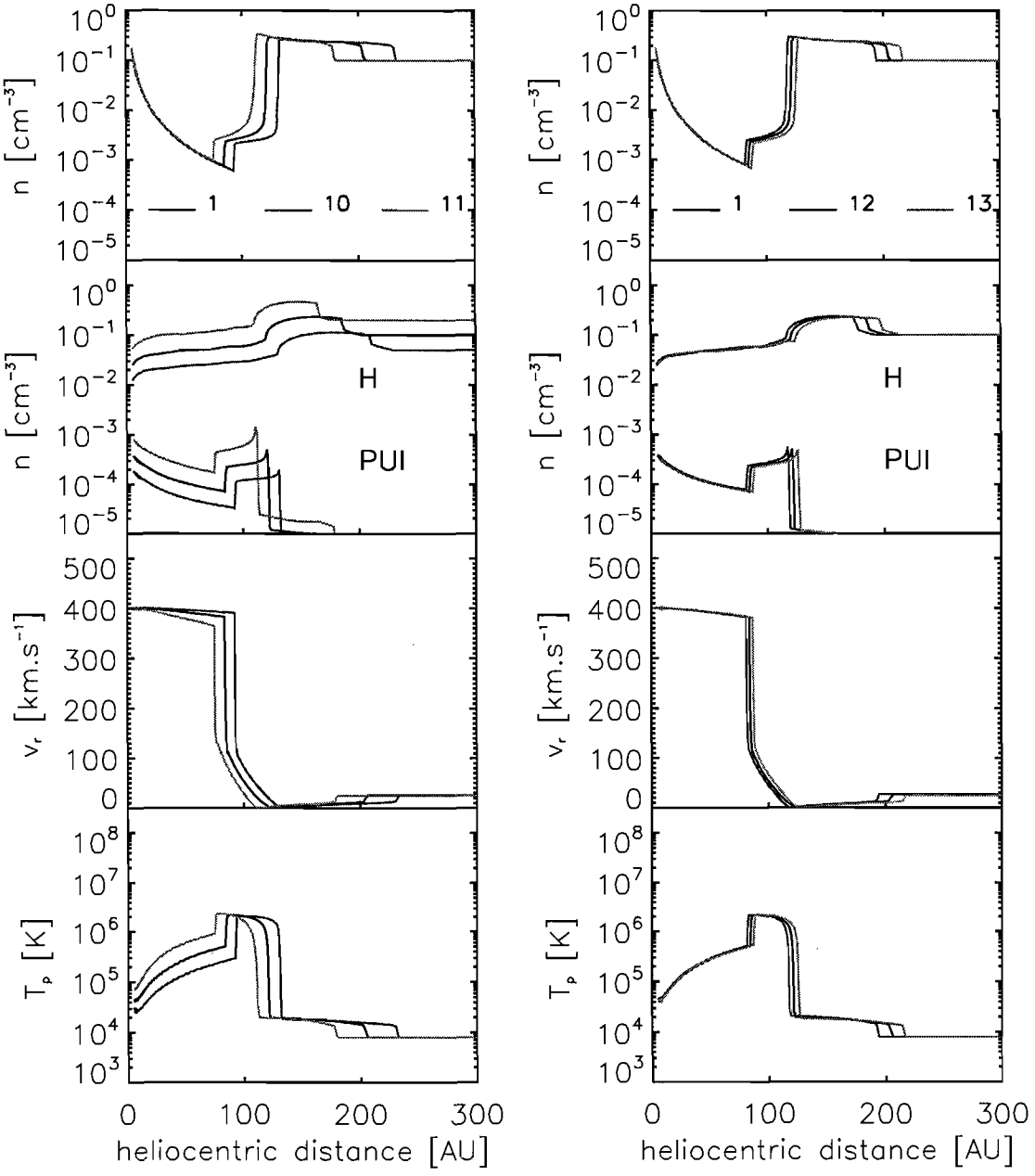

Figure 4.12: The proton (including PUI's), hydrogen and PUI densities as well as the magnitude of the radial proton (including PUI's) velocity and temperature along a radial path in the nose for each of the models 10 – 13 in Table 4.2 with model 1 used as reference.

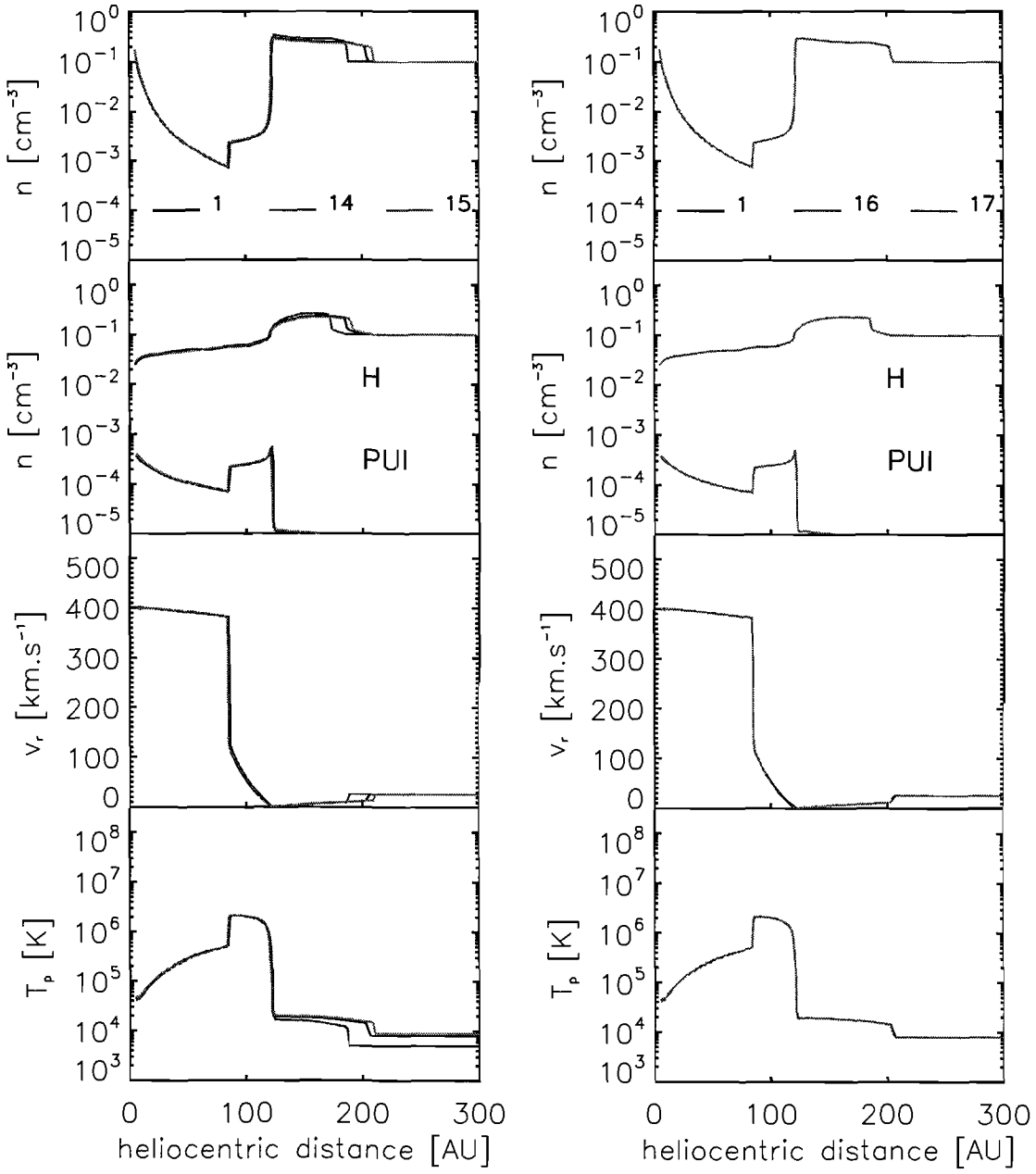

Figure 4.13: The proton (including PUI's), hydrogen and PUI densities as well as the magnitude of the radial proton (including PUI's) velocity and temperature along a radial path in the nose for each of the models 14 – 17 in Table 4.2 with model 1 used as reference.

PUI density throughout this region. The opposite applies to increases in the SW density.

From Fig.(4.10) it can be seen that changing the SW density also alters the volume of the heliosheath. The temperature in the inner heliosheath is of the same order for models 1, 2 and 3. The proton density profiles, however, show that the proton density in the inner heliosheath is larger for larger assumed SW densities at the inner boundary. This implies that the thermal pressure (from the ideal gas law) in the inner heliosheath will be larger for larger initial SW density values. An increase in the thermal pressure of the inner heliosheath needs to be countered by the protons in the outer heliosheath. The result is that both the HP and BS form further out. This accounts for the change in the volume of the heliosheath seen in Fig.(4.10). The opposite applies for model 2 where a reduced SW density is assumed at the inner boundary. This effect has important consequences in a dynamical context as will be shown in the next chapter.

From Fig.(4.8) it follows that reducing the SW velocity by 25% (from 400 km.s^{-1} to 300 km.s^{-1}) causes the TS, HP and BS to form 24% closer to the Sun. Increasing the SW velocity by 12.5% (from 400 km.s^{-1} to 450 km.s^{-1}) results in the TS, HP and BS forming 8%, 13% and 11% further away from the Sun. Comparison with the models 4 and 5 from section 3.5 shows that while a reduction in the SW velocity produces a change in the position of the TS, HP and BS comparable (percentage wise) to that of model 4 in section 3.5, an increase in the SW velocity causes a much smaller change in the position of the three interfaces for the multi-species case. An increase in the SW velocity increases the SW dynamical pressure and allows the SW to expand into a larger volume compared to the standard reference case. However, expansion into a larger volume increases the volume within which charge exchange can cause the SW protons to loose momentum, which in turn decreases the dynamical pressure of the SW and reduces the volume into which it can expand. Therefore, charge exchange acts to negate the increase in dynamical pressure and subsequently causes the TS, HP and BS to form less further out (compared to the multi-species standard model) than was the case for the 'protons only' result. The same applies to an increase or decrease in the relative velocity between the Sun and LISM.

From Fig.(4.10) it follows that increasing the SW velocity results in less PUI's being created in the inner heliosphere. Furthermore, the momentum lost by a representative sample of protons between the Sun and TS is larger the faster the sample of protons are moving as they leave the Sun. Predictably the temperature in the inner-heliosheath is higher for the case where a larger SW velocity is used because more kinetic energy is converted into thermal energy at the TS. This results in the volume of the inner-heliosheath increasing due to the increased thermal pressure. The increased thermal pressure in the inner heliosheath acts to compress the outer heliosheath. This increased compression results in the outer heliosheath increasing in volume as both the HP and BS are pushed out towards the incoming LISM.

Similar to the results shown in section 3.5 it can be seen from Fig.(4.8) that increasing or decreasing the SW proton temperature by 50% (from 10^5 K to 2×10^5 K and 5×10^4 K) does not significantly alter either the position or the geometry of the TS, HP and BS. As was the case

in section 3.5 the kinetic energy of the SW protons dominates the thermal energy in the inner heliosphere. As the protons pass the TS the amount of kinetic energy converted to thermal energy once again dominates the thermal energy 'carried' by the SW from its origin at the Sun. This implies that increasing or decreasing the thermal energy of the SW at the Sun does not significantly alter the dynamics of the SW-LISM interface, even if neutral atoms are included.

Regarding the LISM, a decrease of 50% in the proton density (from 0.1 cm^{-3} to 0.05 cm^{-3}) results in the TS, HP and BS forming at heliocentric distances which are 24%, 30% and 20% larger than for the reference model. An increase of 50% (from 0.1 cm^{-3} to 0.2 cm^{-3}) causes the same three interfaces to form 26%, 16% and 20% further out. Both of these results differ significantly from similar results for the 'protons only' case where it was found that increasing the LISM proton density results in the TS, HP and BS forming 30% closer to the Sun while a 50% decrease caused the three interfaces to form 43% further away.

For the mutli-species case reducing the LISM proton density reduces the dynamical pressure in the LISM. This allows the SW to expand into a larger volume than would be the case for the standard model. Allowing the SW to expand into a larger volume in turn causes the SW to lose more momentum to the neutral species due to charge exchange. This acts to reduce the dynamic pressure of the SW protons which then again counteracts the reduction in LISM proton dynamical pressure. This causes the TS, HP and BS to form less far away from the Sun in the multi-species case than for the 'protons only' case. Increasing the LISM proton density enhances the LISM dynamical pressure. This reduces the volume into which the SW can expand. Reducing this volume causes less momentum to be lost by the SW to the neutral hydrogen species which in turn counteracts the effect of increasing dynamical pressure from the LISM proton species. Therefore, in both cases (models 8 and 9) the inclusion of neutral hydrogen atoms act to reduce the sensitivity of the heliosphere to variations in the LISM state.

From Fig.(4.11) it follows that increasing the LISM proton density decreases the amount of neutral hydrogen that can propagate into the inner heliosphere slightly. A reduced hydrogen density in the inner heliosphere in turn reduces the deceleration and heating experienced by the SW in this region slightly. Furthermore, less neutral atoms in the inner heliosphere leads to smaller amounts of PUI's being produced in this region. Lastly increasing the LISM proton density decreases the volume of the heliosheath which is exactly the opposite of what happens when the SW density is increased.

Decreasing the hydrogen density in the LISM by 50% (from 0.1 cm^{-3} to 0.05 cm^{-3}) causes the TS and HP to form 8% further away from the Sun while the change in the BS position is 13% further out. Increasing the LISM hydrogen density (from 0.1 cm^{-3} to 0.2 cm^{-3}) causes the three interface positions to form 11%, 9% and 13% closer to the Sun. Increasing the hydrogen density at the outer boundary causes more neutral atoms to propagate into the inner heliosphere. This leads to more effective deceleration and heating of SW protons in this region. This culminates in the TS, HP and BS forming closer to the Sun. The opposite applies to the case where the hydrogen density is decreased by 50%. Proton deceleration is less efficient in the heliosheath

Model	r_{TS}	r_{HP}	r_{BS}
1	83	121	208
2	61	90	151
3	100	142	242
4	64	92	155
5	94	136	230
6	83	121	208
7	83	121	208
8	106	158	249
9	62	91	161
10	92	131	230
11	74	110	180
12	86	125	217
13	81	118	191
14	83	121	188
15	83	121	210
16	83	121	208
17	83	121	208

Table 4.3: The radial positions of the TS, HP and BS (r_{TS}, r_{HP} and r_{BS}) in the nose as calculated for the different models in Table 4.2.

and inner heliosphere which in turn causes the three interfaces to form at greater heliocentric distances.

Similar to the results from 3.5 it can be seen from Fig.(4.9) that the BS position is slightly sensitive to increases or decreases in the LISM temperature. From Figs.(4.9) and (4.13) it can be seen that increasing or decreasing the hydrogen temperature by 12.5% and 25% respectively does not alter the heliosphere significantly. The results from above are summarised in Table 4.3

The results presented above show (as was found in section 3.5) that the heliosphere is most sensitive to changes in the dynamic proton pressure associated with either the SW or the LISM. Regarding the role of neutral atoms it is found that in some cases (as noted above) the effects of changes in the proton dynamic pressure are also counteracted through the interaction of protons with neutral atoms. Regarding the hydrodynamical treatment of neutral atoms a selection of the results presented above is now compared to the results of *Müller et al.* (2006). As mentioned previously the results of *Müller et al.* (2006) are calculated using the model developed by *Zank et al.* (1996) which uses a different hydrodynamical formulation of the SW-LISM interaction problem (see the discussion in section 4.2).

4.6 Comparisons between different hydrodynamic formulations

Using a wide range of possible LISM states it was found by *Müller et al.* (2006) that the position of the TS in the tail region is related to the position of the TS in the nose region through the relation

$$r_{TS,t} = (2.08 \pm 0.04) r_{TS} \tag{4.38}$$

where $r_{TS,t}$ and r_{TS} are the positions of the TS in the tail and nose respectively. Similarly it was found that the positions of the HP and BS (r_{HP} and r_{BS}) in the nose are related to the positions of the TS and HP in the nose through

$$r_{HP} = (1.39 \pm 0.01) r_{TS} \tag{4.39}$$

$$r_{BS} = (1.95 \pm 0.05) r_{HP}. \tag{4.40}$$

These relations are found by applying the model developed by *Zank et al.* (1996) (which models the neutral hydrogen population as several distinct hydrodynamical fluids) to different assumed LISM states. A comparison is now made between the interface positions arising from Eqs.(4.38)-(4.40) and the positions of these interfaces as they occur in the numerical results calculated for models 1-17. Regarding a specific model, the position of the TS in the nose is used to calculate the predicted positions of the TS in the tail and the HP and BS in the nose. This is then compared to the positions of these interfaces as they form in the fully two dimensional numerical simulation. Shown in Fig.(4.14) are the positions of the HP and BS in the nose as well as the TS in the tail as found for different models from Table 4.2. Also shown are the same positions calculated using Eqs.(4.38)-(4.40). As can be seen from Fig.(4.14) the actual positions of the TS in the tail and HP in the nose correspond to the same positions calculated from Eqs.(4.38) and (4.39). This implies that the geometry of the heliosphere (affecting $r_{TS,t}$) and the volume of the inner heliosheath (affecting r_{HP}) is the same for the hydrodynamical formulation used here and the formulation used by *Zank et al.* (1996). The only difference between the two formulations seems to be the position of the BS in relation to the HP.

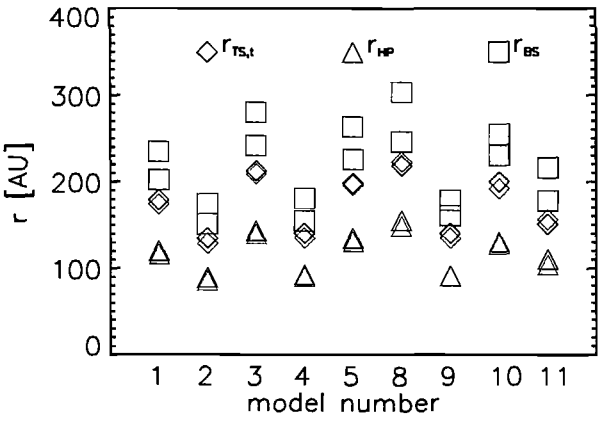

Figure 4.14: The radial position of the HP and BS in the nose and the TS in the tail as found for different models from Table 4.2 (black symbols) and the same positions calculated using Eqs.(4.38)-(4.40) (blue symbols). The errors in Eqs.(4.38)-(4.40) are smaller than the symbols used.

Similar to Eqs.(4.38)-(4.40) it is found by *Müller et al.* (2006) that the hydrogen density at the TS is related to the hydrogen density at 5 AU through

$$n_{H,TS} = (1.43 \pm 0.02) n_{H,5AU}^{0.85 \pm 0.01} \tag{4.41}$$

where $n_{H,TS}$ and $n_{H,5AU}$ are the hydrogen densities at the TS and 5 AU respectively. Similarly the maximum hydrogen density in the hydrogen wall ($n_{H,max}$) is found to be related to the hydrogen density at 5 AU through

$$n_{H,max} = (7.1 \pm 1.5) n_{H,5AU}^{0.81 \pm 0.06}. \tag{4.42}$$

As in Fig.(4.14) the actual hydrogen densities at the TS and in the hydrogen wall (as they arise during the full numerical simulation) from several models in Table 4.2 are compared to results calculated using Eqs.(4.41) and (4.42). The comparison is shown in Fig.(4.15).

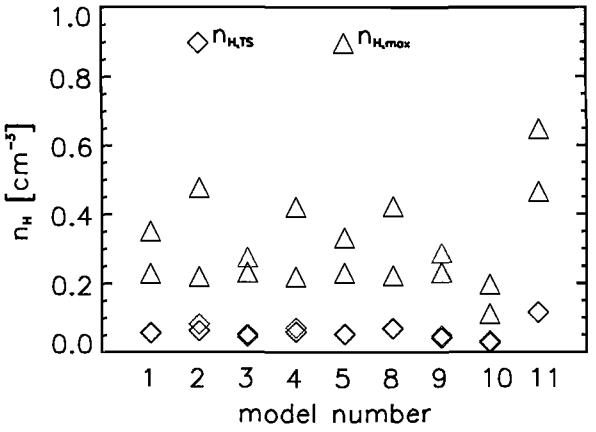

Figure 4.15: The hydrogen density at the TS and in the hydrogen wall as found for different models from Table 4.2 (black symbols) and the same densities calculated using Eqs.(4.41) and (4.42) (blue symbols). The errors in Eqs.(4.41) and (4.42) are smaller than the symbols used.

Regarding the hydrogen density at the TS it can be seen that the hydrodynamical treatment used here yields results similar to the treatment formulated by *Zank et al.* (1996). This implies that the amount of hydrogen propagating into the inner heliosphere (and its subsequent effect on the SW protons) is well described by the model used in this work. Regarding the hydrogen population in the outer heliosheath (represented by the hydrogen density in the hydrogen wall) it can be seen that significant differences exist between the two formulations. Figs.(4.14) and (4.15) suggest that these differences do not extend to the inner heliosheath and inner heliosphere.

This is essentially the conclusion reached by *Fahr and Bzowski* (2004) and *Heerikhuisen et al.* (2006), the latter comparing hydrodynamical results (such as those by *Zank et al.*, 1996) with

kinetic results (similar to the results by *Baranov and Malama,* 1993). While the hydrodynamical description is least accurate for neutral hydrogen atoms in the outer heliosheath, these models still capture some essential features of this population (such as the hydrogen wall) and accurately describe the neutral atom modified SW proton state. It will be shown that this is completely adequate for the application shown in the next chapter where the state of the heliosphere between the Sun and HP needs to be known accurately. In the broader context of cosmic ray modulation it is of utmost importance that heliospheric models describe the TS geometry and PUI abundance accurately. Since these requirements are fulfilled within relatively short computational time spans by the hydrodynamical formulation (and numerical scheme) presented in this work, such a model is best suited for the dynamical results (and subsequent application to cosmic ray modulation) presented in the next chapter.

4.7 Summary

Using a hydrodynamical description of the SW interaction with the hydrogen carrying LISM it is found that the inclusion of neutral atoms in this interaction has a non-negligible effect on the formation of the heliosphere. The interaction between neutrals and protons in the outer heliosheath produces the so called 'hydrogen wall' characterised by the build up of slow neutral atoms between the BS and HP. In the inner heliosheath the interaction between SW protons and incoming neutral atoms results in increased deceleration of SW protons beyond the TS. This produces a density enhancement in this region. In the inner heliosphere the interaction between neutral atoms and SW protons causes the latter to decelerate (while remaining supersonic). The SW pressure gradient between the Sun and TS is also decreased due to the heating of the SW as a consequence of PUI production.

The sensitivity of the heliosphere to different SW and LISM states is also affected by neutral atoms. An increased neutral density acts to produce a more spherically symmetric TS. Furthermore, increases in the SW dynamic pressure are to some extent counteracted by the interaction of the SW with incoming neutral atoms while neutrals tend to counteract the effects of a changing LISM proton state.

The hydrodynamic formulation used in this work serves to capture the state of the neutral atom-modified SW proton species accurately. This can be seen from comparisons with results from *Müller et al.* (2006) and *Heerikhuisen et al.* (2006). Since the hydrodynamical formulation presented here is computationaly efficient, it is used in the next section to examine the heliosphere as a time dependent structure. The state of the heliosphere at a given time is then used to explore the modulation of 10 MeV comsic ray electrons. Since both these applications focus on the region between the Sun and HP, the errors incurred by this formulation regarding the hydrogen and proton species in the outer heliosheath are negligible.

Chapter 5

The dynamic heliosphere and cosmic ray transport

5.1 Introduction

In Chapters 3 and 4 the characteristics of the heliosphere as it forms in a steady state are discussed. In numerical terms this required specification of the SW and LISM states at the inner and outer boundaries of a plane polar grid, as shown in Fig.(2.4)[1]. In Chapters 3 and 4 these specified states were assumed to be time invariant. From the discussion in section 3.2, however, it follows that both the SW and LISM properties change in time. In this chapter the time dependent structure of the heliosphere is investigated as it forms under the influence of a time dependent SW. Throughout the remainder of this chapter it will be assumed that the LISM properties are constant in time.

The SW state varies over both short and long periods of time. An example of the latter is the SW dependence on the solar cycle which was briefly mentioned in section 3.2. In Chapters 3 and 4 it is assumed that the SW expansion is spherically symmetric. However, during periods of decreased solar activity, the SW departs from a simple radial expansion with the emergence of a fast, low density stream at high latitudes. In section 5.2 it will be shown how this solar cycle dependence can be included as a time dependent boundary condition in a hydrodynamical model. The influence of such a time dependent boundary condition on the geometry and plasma flow of the heliosphere is shown.

Apart from the long term variations in the SW (and subsequently in the heliospheric structure) the SW is also subject to short term variations which do not necessarily show any preferred periodicity. The short term variability of the SW is seen in the differences between successive observations of the SW velocity and density, as shown in Fig.(3.1). As an application of the hydrodynamical model presented in this work, it will be shown in this chapter how these short term variations can be included as a time dependent boundary condition in the model in order to compute a record of the heliospheric state over the past $\sim$ 30 years.

[1] In the context of Fig.(2.4) the inner boundary corresponds to the cells immediately bordering the origin at $(0,0)$. The outer boundary corresponds to cells furthest away from the origin.

Using data from the Voyager 1 spacecraft these computations can be constrained and used to estimate the time at which Voyager 2 will cross the TS. The accuracy of the time dependent, hydrodynamic description of the SW-LISM interaction can be tested by comparing the predicted and actual times at which Voyager 2 crosses the TS. Since the trajectories of the Voyager 1 and 2 spacecraft are such that the two spacecraft span an arc of $\sim 55^0$ heliographic latitude the correspondence between the predicted crossing of Voyager 2 and its actual crossing will provide insight into how symmetric the heliosphere is with respect to the solar equatorial plane. This is important since it has been suggested recently (see *Opher et al.*, 2006) that the interstellar magnetic field may produce definite north-south [2] asymmetries in the heliospheric structure.

The chapter concludes with an application in cosmic ray modulation. Using a steady state heliosphere from Chapter 4 in conjunction with a cosmic ray modulation model values for the diffusion coefficients of 10 MeV cosmic ray electrons can be calculated. Using these coefficients together with 10 MeV electron observations from Voyager 1 and 2 provides a method with which to further constrain the time dependent record of the heliosphere calculated below.

5.2 Long term variations in the heliospheric structure

The results presented in Chapters 3 and 4 dealt with the HS as a steady state structure, forming due to the interaction of the SW and LISM where the states of the associated particle populations are assumed to be constant at appropriate boundaries. In section 3.2, however, it is mentioned that solar activity changes from periods of maximum activity to periods of minimum activity (and back) with a periodicity of 11 years. In this section the effect of the solar cycle on the heliosphere is investigated. Similar studies have been presented by *Pauls and Zank* (1997); *Scherer and Fahr* (2003a,b); *Scherer and Ferreira* (2005) and *Ferreira and Scherer* (2006). The aim of this section is to show how a time dependent boundary condition describing the SW dependence on the solar cycle can be included in the numerical model presented thus far. Subsequently a brief overview of the heliospheric response to the solar cycle will be presented. It will be shown how the heliospheric state at different instances can be correlated to actual dates. This correlation is needed to calculate the results presented in the next section.

The 11-year solar activity cycle is visible in observations of sunspot numbers and the magnitude of the magnetic tilt angle (defined as the angle between the solar axis of rotation and the solar magnetic axis) as shown in Fig.(5.1). Both these quantities act as tracers of solar magnetic activity. Comparing Fig.(5.1) with Fig.(3.1) shows the effect of the solar cycle on the SW. During solar maximum (characterised by large sunspot numbers and large tilt angles) the SW exhibits large fluctuations within the smallest time scales (the time between two subsequent observations) as shown in Fig.(3.1). During solar maximum the mean values of the SW velocity and density at 1 AU are approximately $300 - 450$ km.s^{-1} and $2.5 - 7.5$ cm^{-3} at all latitudes and longitudes. This spherical uniformity changes during solar minimum. From Fig.(3.1) it can

[2]Here north and south refers to regions either side of the solar equatorial plane.

be seen that a high speed, low density SW stream emerges at high latitudes during solar minimum. This fast SW component does not exhibit the same large fluctuations over short time scales seen during solar maximum. The difference in amplitude between successive observations is less in the fast SW than in the slow SW at solar minimum (or the SW at any latitude and longitude during solar maximum). The fast SW is characterised by velocities and densities of $750 - 800$ km.s^{-1} and ~ 2.5 cm^{-3}, as mentioned in section 3.2. As a first step in modelling the heliosphere as a time dependent structure this 11 year SW variation is included as a time dependent boundary condition in the hydrodynamical model from Chapter 4.

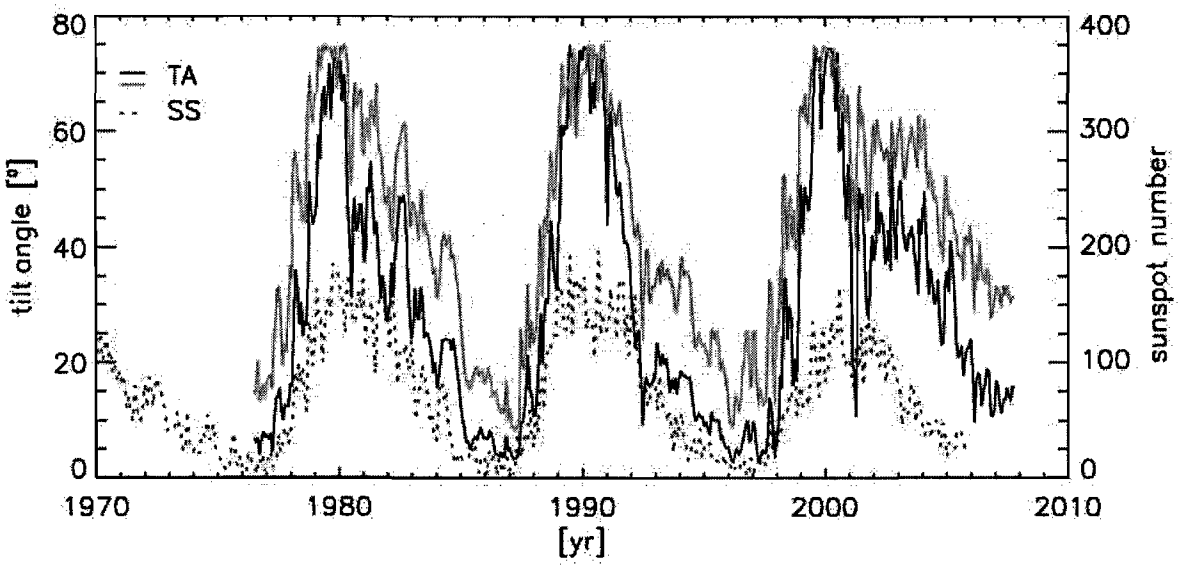

Figure 5.1: The average tilt angle (TA, solid black and green lines) and monthly averaged sunspot number (SS, dotted red line) showing the periodic change between solar minimum and solar maximum. Sunspot data provided courtesy of www.spaceweather.com. Tilt angles are obtained from http://wso.stanford.edu where two different potential field models relying on observations of the solar photosphere are used. These two models are represented by the black and green lines above. See website for more details.

Evident from Fig.(3.1) is that during solar minimum the transition between the slow and fast SW components occur at solar latitudes of $\pm 35^0$. At lower latitudes (between -35^0 and 35^0) it is assumed that the SW state remains unchanged throughout the solar cycle (as is suggested by the Ulysses observations shown in Fig.3.1). At higher latitudes (less than -35^0 and greater than 35^0) it is assumed that the fast stream emerges gradually as solar minimum occurs, with maximal velocities reached every 11 years. Assuming that the SW velocity at high latitudes increases from 400 km.s^{-1} during solar maximum to 800 km.s^{-1} during solar minimum (corresponding to a period of 5.5 years) the time and latitude dependent radial SW velocity $\mathbf{v}(\phi, t)$ (in a particular solar hemisphere) at 1 AU is described by

$$\mathbf{v}(\phi, t) = v_0 A_v(\phi, t)\hat{r} \tag{5.1}$$

(here ϕ denotes solar latitude) where $v_0 = 400$ km.s^{-1} and $\hat{r}$ is a unit vector in the radial

direction. A_v is given by

$$A_v = 1 + f(t) \mp f(t) \tanh\left[\frac{2\pi}{45^0}\left(\phi \pm 35^0\right)\right] \tag{5.2}$$

in the northern and southern solar hemisphere respectively with

$$f(t) = 0.25\left[\cos\left(\frac{2\pi t}{11} + \pi\right) + 1\right]. \tag{5.3}$$

Eqs.(5.2) and (5.3) are obtained by combining the SW latitudinal dependence from *Hattingh* (1998) and *Ferreira* (2001) with the sinusoidal time variation used by *Scherer and Fahr* (2003a). Here t is the time in years and ϕ the latitudinal angle. The value of A_v at different times and latitudes is shown in Fig.(5.2). The line defined by $\phi = \pm 90^0$ is parallel to the solar axis of rotation and assumed to be perpendicular to the LISM inflow direction. Positive latitudes refer to the northen hemisphere while negative latitudes refer to the southern hemisphere. The plane defined by $\phi = 0$ lies along the x-axis in Fig.(2.4) and corresponds to the solar equatorial plane. The results presented in this section are restricted to a heliocentric plane parallel to both the solar rotation axis and the LISM inflow direction (where it is assumed that the latter is perpendicular to the former). The rotation of the Sun is neglected in all the results presented in this chapter. Therefore, the x-axis in Fig.(2.4) is fixed to be anti-parallel to the LISM inflow direction at the outer boundary.

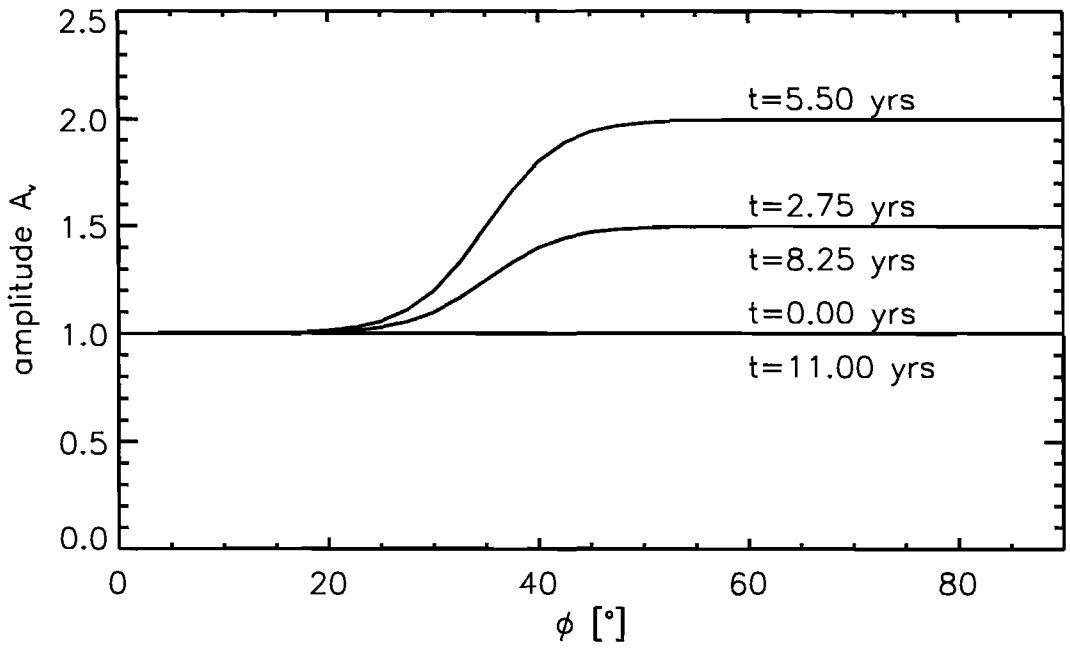

Figure 5.2: The time and heliolatitude dependent amplitude of the SW. The magnitude of the SW velocity during solar maximum is assumed to be 400 km.s^{-1}. Multiplication with A_v approximates the SW velocity dependence on solar latitude and time at 1 AU.

Eq.(5.1) is now used as a time dependent boundary condition describing the velocity of the SW at 1 AU in the hydrodynamical model discussed in Chapter 4 (including the effect of neutral atoms in the LISM on the heliosphere). It is assumed that the LISM state is constant over the time scales involved and similar to the LISM state used for model 1 in section 4.5. Using these boundary conditions the model is evolved in time until all oscillations become approximately harmonic. Similar to *Scherer and Fahr* (2003a) the SW proton density is calculated by assuming that

$$\rho_p v_p = constant \tag{5.4}$$

everywhere and for all times (where v_p is the magnitude of the time and latitude dependent SW velocity). The results ('snapshots' taken at solar minimum) are shown in Figs.(5.3) and (5.4).

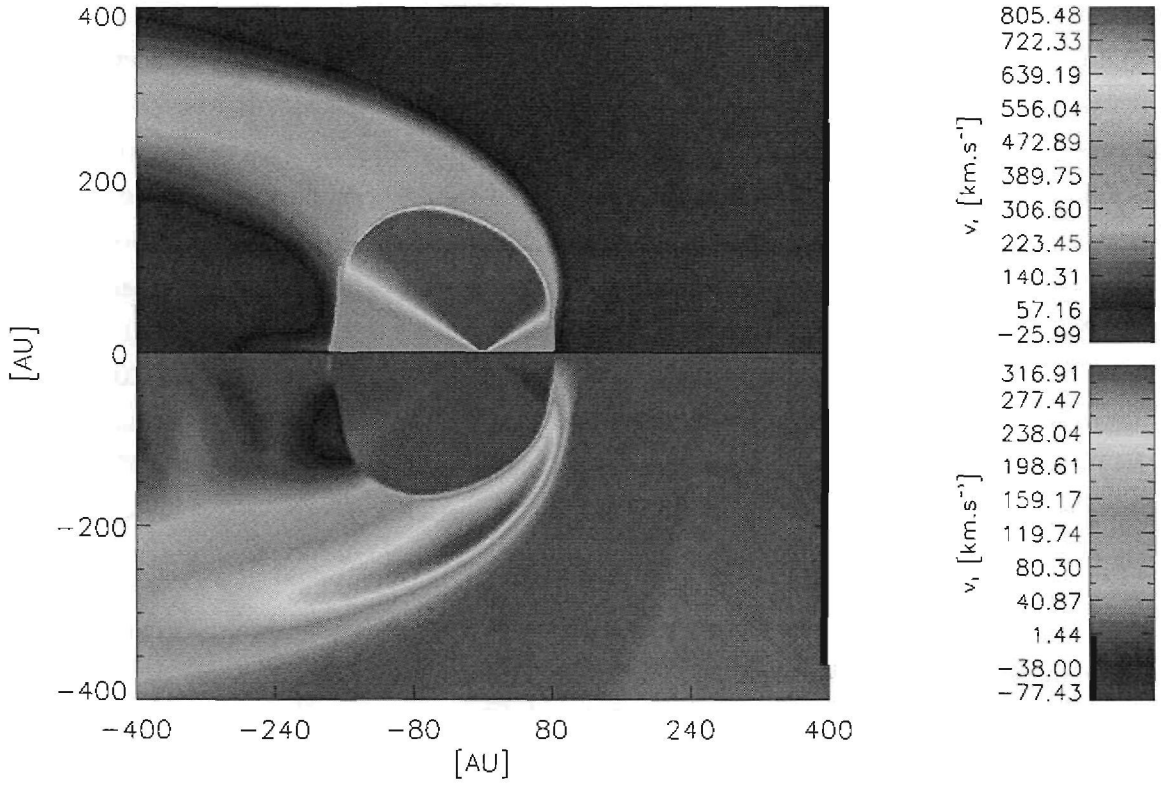

Figure 5.3: The radial (top) and tangential (bottom) proton velocity in a plane parallel to the LISM inflow direction and the solar axis of rotation at solar minimum. It is assumed that the solar rotation axis is perpendicular to the LISM inflow velocity. In the top panel the fast SW is visible as the red conical structure protruding from the Sun at the origin into the polar regions. Due to the enhanced dynamic pressure of the fast SW the heliosphere is elongated in the polar directions compared to Fig.4.3.

Fig.(5.3) shows the proton [3] radial and tangential velocities in a heliocentric plane parallel to both the LISM inflow direction and the solar axis of rotation. The fast solar wind stream is vis-

[3]Here as in the previous chapter 'proton' refers to both protons of solar origin and PUI's created in the SW.

ible (in the SW radial velocity) as the red conical structure protruding into the polar regions. The maximal fast SW velocity (at high latitudes) is two times greater than the slow SW velocity at lower latitudes (or the SW velocity during solar maximum) and two times less dense. Recalling that the dynamic pressure is given by $\rho_p v_p^2$ this implies that the fast SW dynamic pressure is greater than the slow SW dynamic pressure (or the dynamic pressure of the SW at solar maximum) by a factor of 2. From the parameter study presented in section 4.5 it is expected that greater SW dynamic pressures will result in the TS, HP and BS forming further away from the Sun. In Fig.(5.3) and Fig.(5.4) it can be seen that this is indeed the case for regions in the fast SW stream. The fast SW acts to elongate the heliospheric structure over the polar regions as the TS, HP and BS in these regions are pushed further out (compared to Fig.4.3 and Fig.4.6). This is consistent with results presented by *Pauls and Zank* (1997) and *Scherer and Ferreira* (2005)

Fig.(5.4) shows that the fast SW causes less hydrogen atoms to propagate into the volume between the Sun and HP. This in turn reduces PUI production in this region significantly. Evident in Fig.(5.4) is that the PUI density in the nose during solar minimum is approximately the same as the PUI density in the nose and polar regions during solar maximum. The decrease in the PUI density in the fast SW regions is consistent with the results found in section 4.5 where it was shown that an increase in the SW dynamic pressure reduces the number of hydrogen atoms propagating into the inner heliosheath (and subsequently into the region between the Sun and TS). Furthermore, the reduced density of the fast SW further impedes PUI production. Therefore, during solar minimum less PUI's are created in the polar regions than in the nose regions (or in both regions during solar maximum). Quantitatively it can be seen that the PUI density in the polar regions is 0.35 times less than the PUI density in the nose during solar minimum. This is similar to the results presented by *Scherer and Ferreira* (2005) where it is noted that during solar minimum most of the PUI production occurs in the equatorial regions. As PUI's provide a seed population for ACR's (as PUI's are accelerated at the TS) a solar cycle dependent PUI production rate also implies that the ACR intensity in the heliosphere should vary with the solar cycle (see *Scherer and Ferreira*, 2005).

In section 4.5 it is also shown that increasing the dynamic pressure of the SW leads to increased temperatures in the inner heliosheath. The temperature profiles in Fig.(5.4) are consistent with these results. As mentioned in sections 3.5 and 4.5 the transition of the TS by the SW corresponds to most of the SW kinetic energy being converted into thermal energy. Due to the increased dynamic pressure of the fast SW more kinetic energy is converted to thermal energy as the TS is crossed. Therefore, the temperature of the shocked fast SW plasma is higher (by a factor of ~ 4) in the polar regions compared to the slow SW temperature in the inner heliosheath at lower latitudes (or the subsonic SW in the inner heliosheath during solar maximum).

As the fast SW reaches the TS it undergoes a transition to a denser subsonic flow. However, the fast SW in the heliosheath is less dense (by a factor of ~ 4) than the slow SW in the inner heliosheath at lower latitudes (or the SW in the inner heliosheath during solar maximum) as shown in Fig.(5.4). In Fig.(5.4) the steady state results (blue lines) approximate solar maxi-

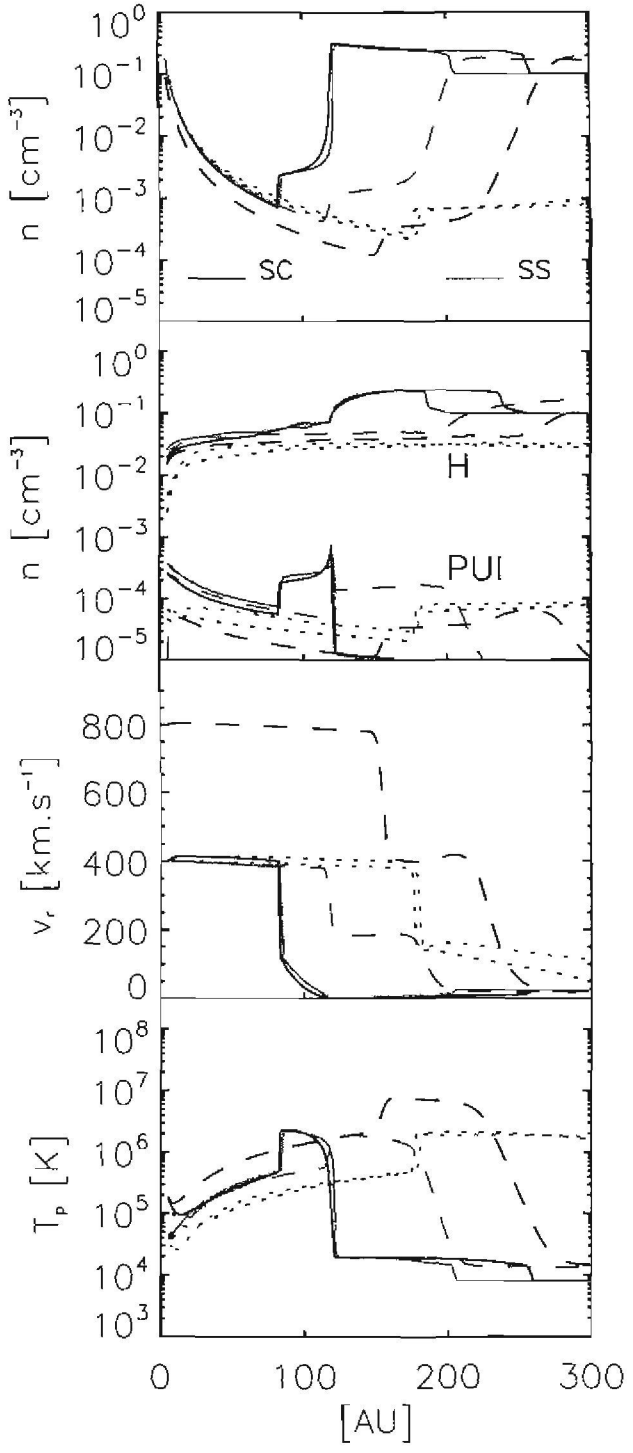

Figure 5.4: Radial profiles of the proton, hydrogen and PUI density, proton speed and proton temperature in the nose (solid lines), polar region (dashed lines) and in the tail (dotted lines). In the inner-HS and inner heliosheath the proton density refers to the sum of the SW proton and PUI densities. Black lines (denoted by SC for 'solar cycle' in the top panel) indicate profiles during solar minimum. Blue lines correspond to the same profiles for the steady state (SS) multi-species case from Fig.(4.6) in which the SW expansion was assumed to be spherically symmetric. Note that the temperature and density axis are scaled logarithmically.

mum conditions. However, the fast SW in the heliosheath flows considerably faster than the slower SW in the same region during solar maximum (as can be seen by comparing Fig.5.3 and Fig.4.3). Therefore, as solar minimum conditions continue the fast SW 'blows' a low density bubble in the inner heliosheath, as shown in the top panel of Fig.(5.5).

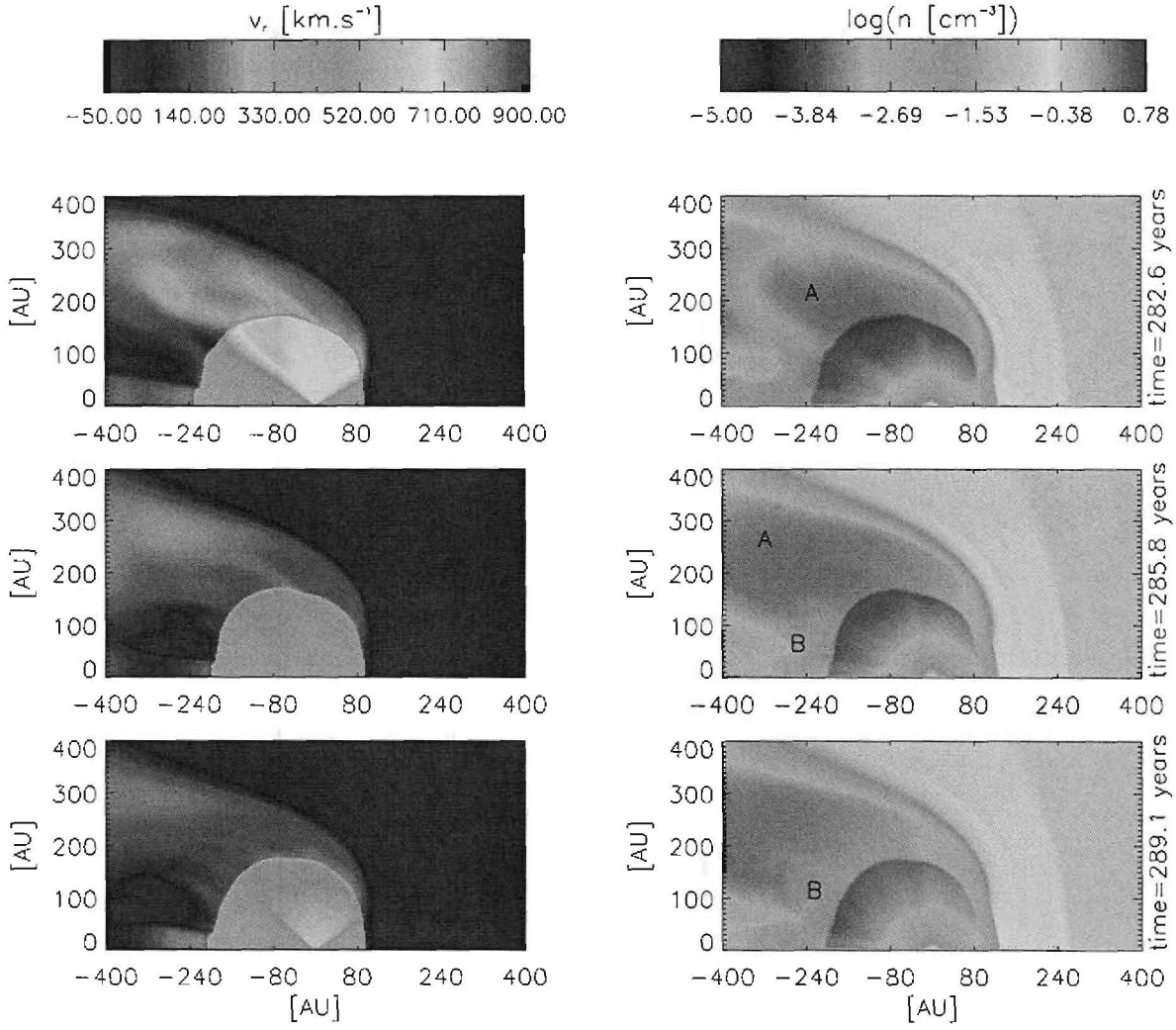

Figure 5.5: The proton speed and density in a plane parallel to both the LISM inflow velocity and solar axis of rotation at different times. The times listed are measured from the instance the model is run. The top panel shows a snapshot of the heliosphere a short time after solar minimum. The fast SW blows a low density bubble (A) in the inner heliosheath. As the solar cycle progresses towards solar maximum the bubble (A) propagates as shown in the middle panel. The passage of the low density region (A) induces rotational flows (B) in the tail, beyond the TS. Note that the logarithm of the density is shown in the three panels to the right in order to resolve the contrast between regions characterised by different densities to a better extent.

Progressing towards solar maximum the fast, less dense SW in the inner heliosheath is steadily replaced by a slower, denser proton flow as can be seen from the middle panel in Fig.(5.5). As the cycle is repeated this results in a series of rarefaction waves propagating through the inner heliosheath, as is suggested by comparing the positions of the region marked (A) in the top and middle panels of Fig.(5.5). This corresponds to the results presented by *Scherer and Fahr*

(2003a,b) and *Scherer and Ferreira* (2005). Noted by the latter is the emergence of a 'tornado alley' during solar minimum. The 'tornado alley' is shown in Fig.(5.5) as the region of fast rarefied plasma flow emerging beyond the TS in the polar regions during solar minimum. In the tail region (outside of the fast heliosheath flow region) the passage of a rarefied region induces an inflow of particles (shown in the middle and bottom panels of Fig.5.5) into a region bordering both the TS and fast inner heliosheath flow. This in turn causes a rotational flow beyond the TS in the tail, as can be seen from the bottom panel of Fig.(5.5) and the regions of adjacent positive and negative tangential flow in Fig.(5.3). As noted by *Scherer and Ferreira* (2005) the 'tornado alley' affects the divergence of the SW in the heliotail, which in turn affects CR modulation (as will be discussed briefly in section 5.4).

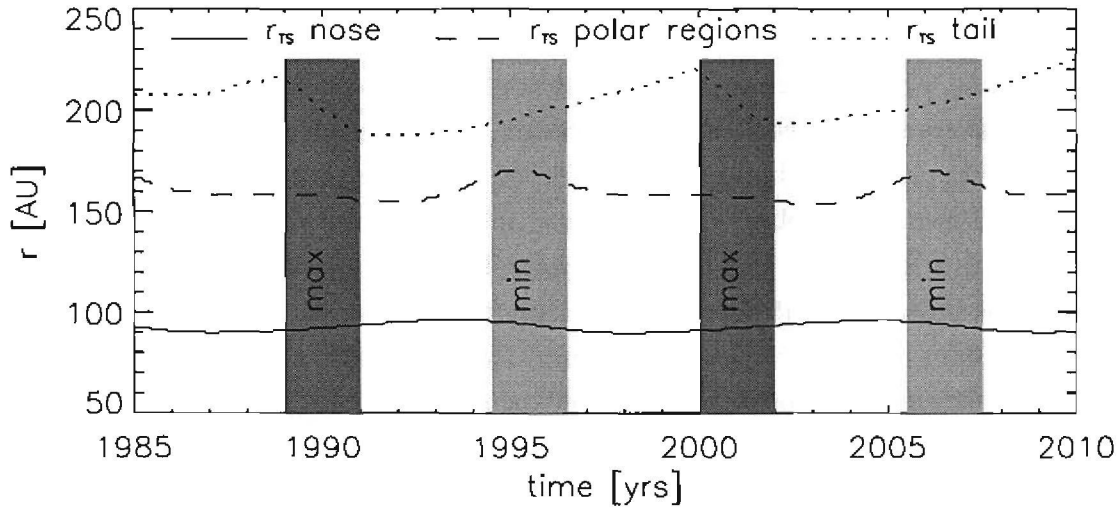

Figure 5.6: The radial position of the TS (r_{TS}) in the nose (solid line), polar region (dashed line) and in the tail (dotted line) with time. The shaded regions indicate periods of maximal solar activity (denoted by 'max') and minimal activity (denoted by 'min'). The solar cycle induces a TS response at all latitudes. The TS response in the nose is out of phase with the TS response in the polar regions. The same is found for the TS response in the tail.

The solar cycle induces variations in the TS position over all latitudes as shown in Fig.(5.6). As the solar cycle progresses towards solar minimum the TS responds by moving outward over the polar regions. At lower latitudes the TS response is delayed. Furthermore, the TS response in the polar regions and tail is more prominent than the TS response in the nose. In the polar regions the TS position changes with $\sim$ 15 AU between solar minimum and maximum. In the nose the change in the TS position is $\sim$ 5 AU. Similar studies regarding the variation of the TS with the solar cycle have been presented by *Whang and Burlaga* (1993); *Karmesin et al.* (1995) and *Wang and Belcher* (1999). In all three cases it was found that the TS moves outward as solar minimum is approached and inward towards solar maximum. The variation in the TS position was found to be in the order of $\sim$ 10 AU. It needs to be noted that the results presented here follow the more detailed approach by *Scherer and Fahr* (2003a) and *Scherer and Fahr* (2003b) where the extent of the fast SW is limited to high latitudes. The result is the phase difference

between the TS response at different latitudes as shown above and the decreased amount of movement exhibited by TS in the nose.

The TS response to the increased dynamic pressure in the fast SW hints at what can be expected if the short term variations in the SW state observed by different spacecraft are included in the model. It will be shown that the slow SW dynamic pressure (or the dynamic pressure of the SW at solar maximum) can easily vary by a factor of 2 on relatively short time scales. This implies that the short term dynamic pressure variations in the SW can cause the TS to react differently at different latitudes. In the next section a record of the TS position at different times will be calculated by taking into account both short and long term variations in the SW state. In order for such a calculation to be useful the results at different time steps in the model need to be correlated with actual dates.

Fig.(5.6) resembles a first step in calculating an accurate record of the heliospheric state over the past $\sim$ 30 years. While the heliosphere also exhibits short term variations which may influence its state (these are considered in the next section), the results shown in Fig.(5.6) will be used as a foundation on which shorter term variations are imposed. Since short term variations are calculated from actual observations in time, the time evolution in the model needs to be correlated with actual dates. This is done by using the $\sim$ 11 year periodicity of the solar cycle. The time scale shown in Fig.(5.6) is calculated by letting the dynamic model reach a state where all the oscillations are approximately harmonic. The first solar maximum after such a state is reached is associated with solar maximum between 1967 and 1970. Initially the date at which solar activity was maximal is assumed to be the first of January, 1969. It needs to be noted that records of sunspot numbers between 1964 and 1975 show that the sunspot number in this time interval peaked between 1967 and 1970. Therefore, the actual dates with which the model results are correlated may be shifted forward in time by 1 year and backwards in time by 2 years. By assigning a date to the first solar maximum after a harmonic state is reached allows for the correlation between subsequent model results (at later times) and actual dates. The time correlation discussed here will be used in the next section.

5.3 Modelling the heliosphere using spacecraft observations

The first aim of this section is to obtain an accurate record of the heliospheric state over the past $\sim$ 30 years. In the context of hydrodynamic models (as presented so far in this work) this necessitates that the state of both the SW and LISM be known at points in space and time that can be used in a numerical model (as a appropriate boundary conditions). Using the characteristics of the heliosphere (as discussed in section 4.4) in conjunction with the observations from a range of spacecraft, such time dependent boundary conditions describing the state of the SW at 1 AU (containing the short term variations in the SW state observed by spacecraft) can be obtained. As in the previous section it will be assumed that the LISM state is constant over the time scales involved.

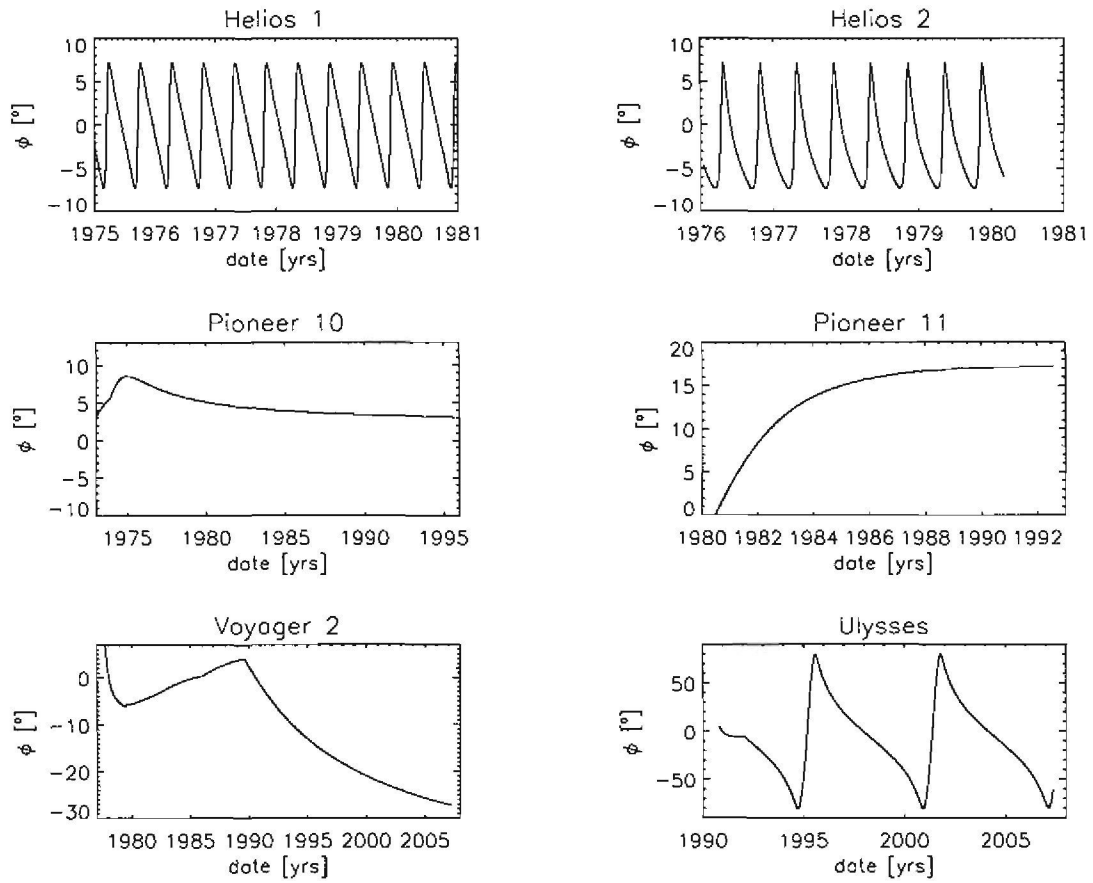

Figure 5.7: The heliographic latitude of Helios 1, Helios 2, Pioneer 10, Pioneer 11, Voyager 2 and Ulysses with time. SW observations from these spacecraft are used as boundary conditions in the model. Regarding the discussion in section 5.2 it can be seen that only Ulysses reached sufficient latitudes to observe the fast SW during solar minimum.

Similar studies have been presented by *Belcher et al.* (1993); *Wang and Belcher* (1999) and *Whang and Burlaga* (2000). See also *Stone and Cummings* (2001). This section aims to extend these studies by using SW plasma data observed between 1975 and the present from a range of spacecraft. Furthermore, the results presented here take into account the solar cycle dependent SW, as described in the previous section. Observations from the Helios 1 and 2, Pioneer 10 and 11, Voyager 2 and Ulysses spacecraft are used in this regard. Shown in Fig.(5.7) are the heliographic latitudes of these spacecraft with time. Evident from Fig.(5.7) is that all the spacecraft, with the exception of Ulysses, stayed within a heliographic latitude range of $[-30^0, 30]$ between 1975 and 2007. Since the fast solar wind only appears at latitudes greater than $\sim 35^0$ (from section 5.2), the data from these spacecraft, together with low latitude observations from Ulysses, provide measurements of the slow SW state at different points in space and time.

Not shown in Fig.(5.7) are the heliographic longitudes at which the above mentioned spacecraft are found at different times. In Chapters 3 and 4 it is assumed that the SW state at the inner boundary is spherically symmetric. In section 5.2 a departure is made from this spherical

symmetry by using a time and latitude dependent boundary condition in describing the SW state at the inner boundary, neglecting solar rotation. This leads to the SW expansion being symmetric about the solar axis of rotation, implying that the SW state at the inner boundary does not vary with longitude. Physically it is entirely possible for the SW flow to differ over heliographic longitude. Assuming that any variation in the SW state between different longitudes arises at the Sun (and that whatever structure causes these variations rotates with the Sun) averaging over one solar rotation should limit longitudinal variations in spacecraft data. Therefore, in order to limit these variations, 26-day averages (corresponding to the solar rotation period) of spacecraft data will be used in this section.

In the context of hydrodynamical models the SW and LISM states are specified at appropriate boundaries (as discussed in the beginning of sections 3.3 and 4.4). In contrast, the positions in space at which spacecraft data are observed do not necessarily correspond to these boundaries. Therefore, a spacecraft observation describing the SW state at a certain point in space and time needs to be extrapolated to 1 AU (corresponding to the inner boundary of the numerical model) and adjusted in time. In order to achieve this results from sections 4.4 and 4.5 are used.

In section 4.5 it was found that the SW density in the nose and polar regions is proportional to r^{-2} between the Sun and TS irrespective of the SW state (where r is the distance from the Sun). Therefore if a density n is observed at position r the r^{-2} proportionality implies that

$$nr^2 = n_{1AU}r_{1AU}^2 = constant \tag{5.5}$$

where n_{1AU} is the density at 1 AU, and $r_{1AU} = 1$ AU. From Eq.(5.5) the corresponding density at 1 AU can be calculated.

Regarding the velocity it was found in section 4.4 that the SW velocity decreases between the Sun and TS due to the interaction between protons and hydrogen atoms. From model 1 in section 4.5 the velocity decrease between the Sun and the TS can be approximated to be linear in r (shown in Fig.5.8). This implies that

$$v_p \approx mr + c \text{ for } 0 \leq r < r_{TS} \tag{5.6}$$

where v_p is the magnitude of the radial proton velocity and

$$m = -1.69 \times 10^{-9} \text{ s}^{-1}. \tag{5.7}$$

The value of c can be calculated from Eq.(5.6) using m and the observed velocity at a position r. Using Eq.(5.6) the velocity measured by a spacecraft (at some distance beyond 1 AU) is extrapolated back to 1 AU. Assuming that the LISM state is constant over the time scales involved, from Fig.(4.10) it can be seen that the value of m in Eq.(5.6) (corresponding to the slope of the velocity profiles in the figure) remains approximately the same irrespective of the SW velocity.

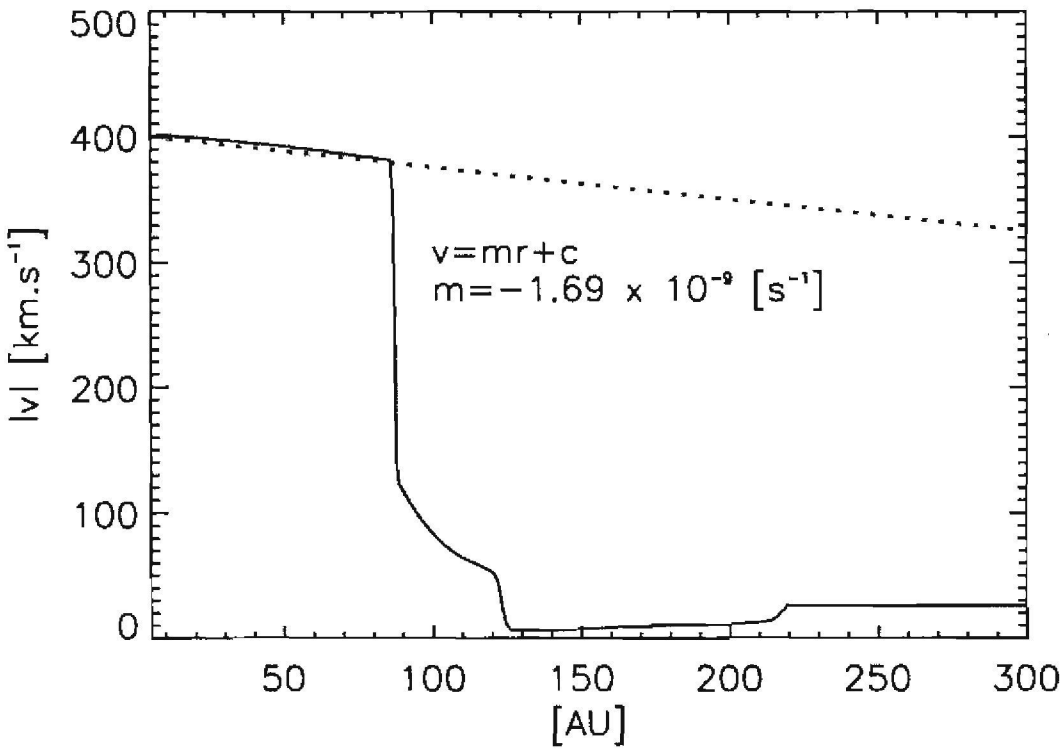

Figure 5.8: The magnitude of the radial proton velocity along a radial path in the nose (solid black line) calculated for model 1 in section 4.5. The decrease in velocity between the Sun and TS is approximately linear, as shown by the dotted line above.

Furthermore, the decrease in velocity between the Sun and TS is approximately similar for SW densities greater than or equal to 5.0 cm^{-3}. For lower densities the slope of the velocity profile tends to zero. For these cases using $m = -1.69 \times 10^{-9}$ s^{-1} incurs a small error, proportional to the difference between the velocity calculated from Eq.(5.6) and the real value of the velocity at some distance r. It should be noted that the above results do not take pressure effects from the PUI population into account. As shown by *Fahr and Fichtner* (1995) the inclusion of such effects may lead to less pronounced deceleration of the SW. However, the correlation between different results (shown later in this section) suggests that any error incurred by neglecting this effect is marginal within the context of this work.

Lastly as the observed SW density and velocity values are extrapolated back to 1 AU the time at which these values describe the SW state must also be adjusted. Therefore, if a spacecraft observes the state of a certain sample of SW particles at a point in time and space, extrapolating this state back to 1 AU should be similar to an observation of the same sample of protons at 1 AU at an earlier time. Integrating Eq.(5.6) over time (where t_1 denotes the time at which the observation is made by the spacecraft and t_0 is the time at 1 AU) yields

$$t_1 - t_0 = \frac{1}{m} \ln \left| \frac{mr_1 + c}{mr_0 + c} \right| \tag{5.8}$$

where r_1 is the radial position at which the observation is made at time t_1 and r_0 corresponds to 1 AU. Using Eqs.(5.5), (5.6) and (5.8) the SW observations from the spacecraft listed Fig.(5.7) are extrapolated back to 1 AU, with the time adjusted accordingly. Also shown is the corresponding dynamic pressure at 1 AU calculated from the extrapolated density and velocity values. Starting with the first of January 1975 the extrapolated values of the density and velocity from all spacecraft (given that a particular spacecraft was active during that time interval) are binned in 26-day intervals. All the data from a specific spacecraft in a specific time interval are then averaged over that time interval, thereby obtaining extrapolated 26-day averages of the SW density and velocity for each spacecraft. Using these different 26-day averages in each 26-day interval an upper, lower and mean value is calculated. The upper limit is taken as the largest 26-day averaged value (from any spacecraft) within a specific 26-day interval, the lower limit as the smallest average value within the same interval, and the mean value as the average of all the 26-day averages (from all spacecraft) within that 26-day interval. The results are shown in Fig.(5.9).

The data shown in Fig.(5.9) can now be used as an appropriate time dependent boundary condition describing the SW state at 1 AU in a hydrodynamical model of the SW-LISM interaction. Similar to Fig.(5.6) the hydrodynamical model is evolved in time, using the time dependent boundary condition described in section 5.2. The first solar maximum after an approximately harmonic state is reached is associated with the first of January 1969. Thereafter the model is evolved in time until the simulation time corresponds to the first of January 1975. As the model progresses beyond this point in time, the extrapolated values from Fig.(5.9) are used to describe the SW state at 1 AU, corresponding to a specific time. During solar maximum conditions it is assumed that the SW state at 1 AU is similar over all latitudes. As solar minimum is approached the emerging fast SW state gradually approaches a density of 2.5 cm^{-1} and a velocity of 800 $km.s^{-1}$ for all latitudes above 35^0 and below -35^0. This is done in order to be consistent with Ulysses observations showing very little variability in the fast SW. The result is a record of the approximate state of the heliosphere for the past $\sim$ 30 years.

Using the upper, lower and mean values in Fig.(5.9) three different records of the heliosphere are calculated. Shown in Figs.(5.10) and (5.11) are snapshots of the heliosphere (calculated from mean values in Fig.5.9) taken at different times. Most visible in the middle panels are the effect of short term variations in the SW on the TS structure. The short term variations from Fig.(5.9) induce waves of increased and decreased dynamic pressure in the SW. As these waves reach the TS it is expected from the discussion in sections 3.5 and 4.5 that the TS will move inward or outward in the response to these changes in dynamic pressure. During solar minimum these waves are confined to the slow SW. Subsequently the TS response is to a combination of the short term variations in dynamic pressure at lower latitudes and the solar cycle induced increase in dynamical pressure at high latitudes. Also evident from Figs.(5.10) and (5.11) is that the short term variations in the SW propagate well into the inner heliosheath, and become less and less visible as the HP is approached.

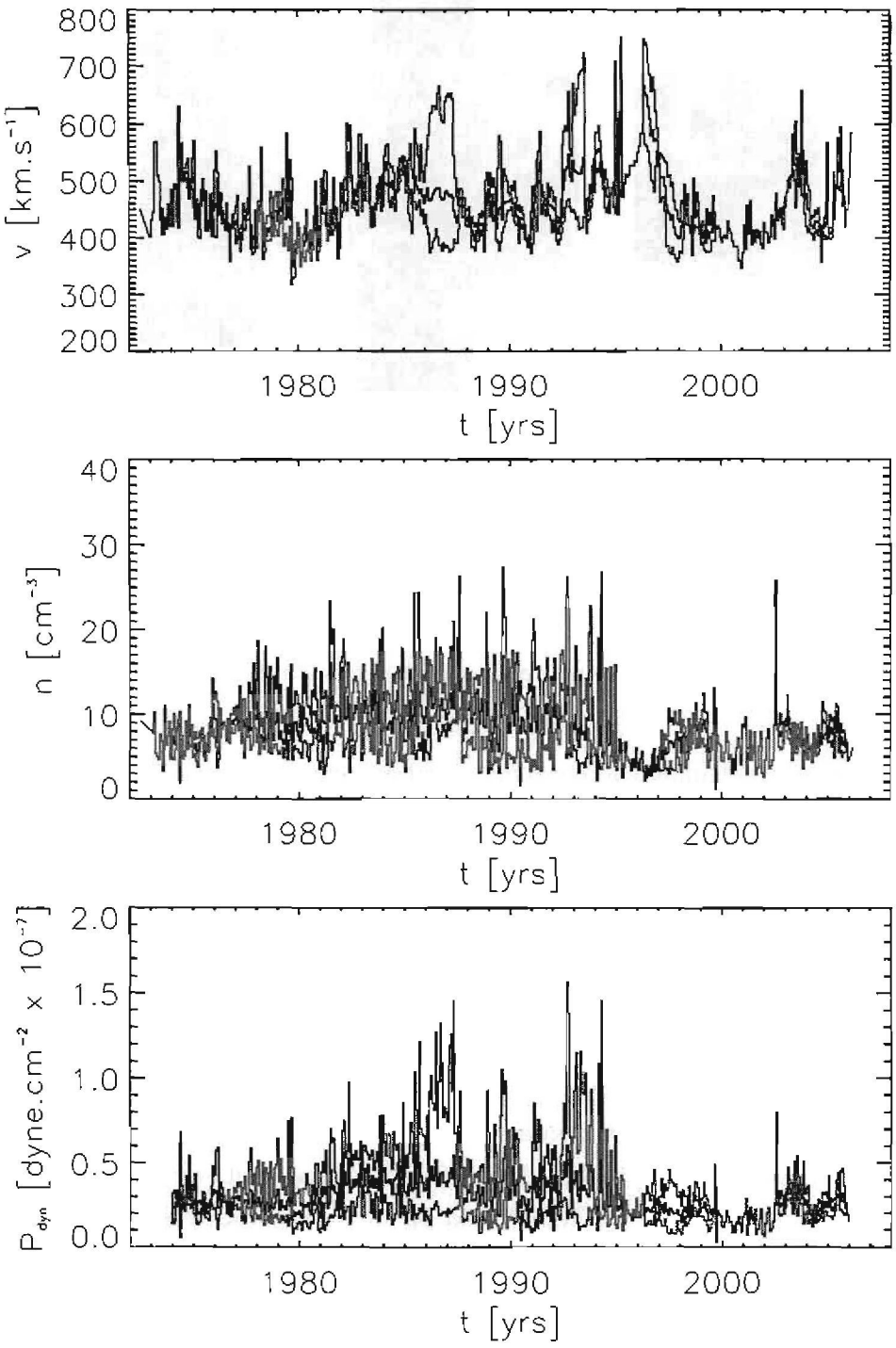

Figure 5.9: Upper (solid red lines), lower (solid blue lines) and mean values (solid black lines) of 26-day averaged values of the SW density (top), velocity (middle) and subsequent dynamic pressure (bottom). The dynamic pressure is denoted by P_{dyn}. The actual daily observations form the Helios 1 and 2, Pioneer 10 and 11 as well as the Voyager 2 and Ulysses spacecraft are extrapolated back to 1 AU using Eqs.(5.5), (5.6) and (5.8) and averaged over 26-day intervals. Original data provided courtesy of http://cohoweb.gsfc.nasa.gov.

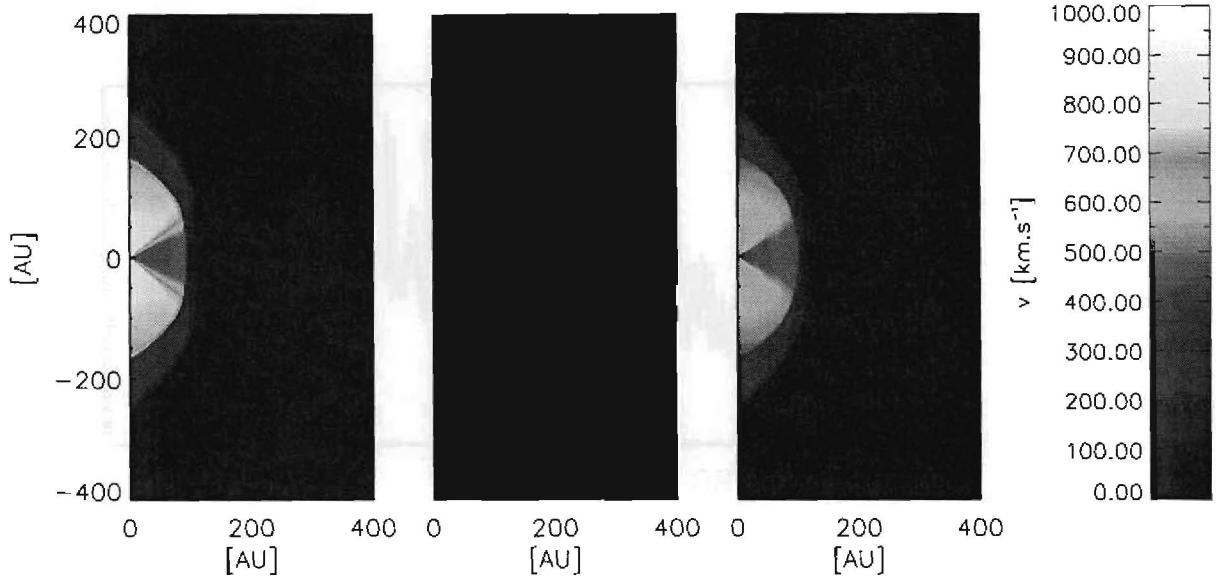

Figure 5.10: The magnitude of the proton velocity in the nose and polar regions of the heliosphere during solar minimum 1996 (left panel), solar maximum 2001 (middle panel) and in 2005, approaching solar minimum (right panel). During solar maximum the short term variations in the SW from Fig.(5.9) are used to describe the SW state at 1 AU over all solar latitudes. As solar minimum is approached the fast SW approaches a smooth stream characterised by a velocity of 800 km.s^{-1} at 1 AU, over all fast SW latitudes.

The record of the HS calculated above is now further constrained by using the known time and position at which Voyager 1 crossed the termination shock. It is known that Voyager 1 crossed the TS during December 2004 at a radial distance of 94 AU away from the Sun (see for example *Webber*, 2005). At the time of crossing Voyager travelled along a trajectory at a heliographic latitude of 34.1^0. This offers a point in space and time with which to normalize the TS position in the calculated record of the heliosphere.

From the calculated record of the heliosphere the difference in position of the TS at 34.1^0 degrees heliographic latitude during December 2004 is compared to the known radial position (at 94 AU) at which Voyager 1 encountered the TS. It is found that the numerical model over estimates the TS position by $\sim$ 10 AU (due to the LISM state not being known exactly). Using this difference the positions of the TS, HP and BS are now reduced by decreasing their radial positions at all latitudes and times by $\sim$ 10 AU so that the TS position at 34.1^0 heliographic latitude during December 2004 is 94 AU. The normalised TS position at Voyager 1 and 2 latitudes is shown in Fig.(5.12).

Using the normalised TS position the time at which Voyager 2 should cross the TS can be estimated. Voyager 2 is currently travelling at a latitude of -27^0 with near constant velocity. Therefore, from the calculated TS position at -27^0 latitude the time at which Voyager 2 should encounter the TS can be estimated, as shown in Fig.(5.12). Evident from Fig.(5.12) is that in all three cases (calculated from upper, lower and mean values respectively) Voyager 2 should have crossed the TS during 2007. Preliminary results from comparing energetic particle inten-

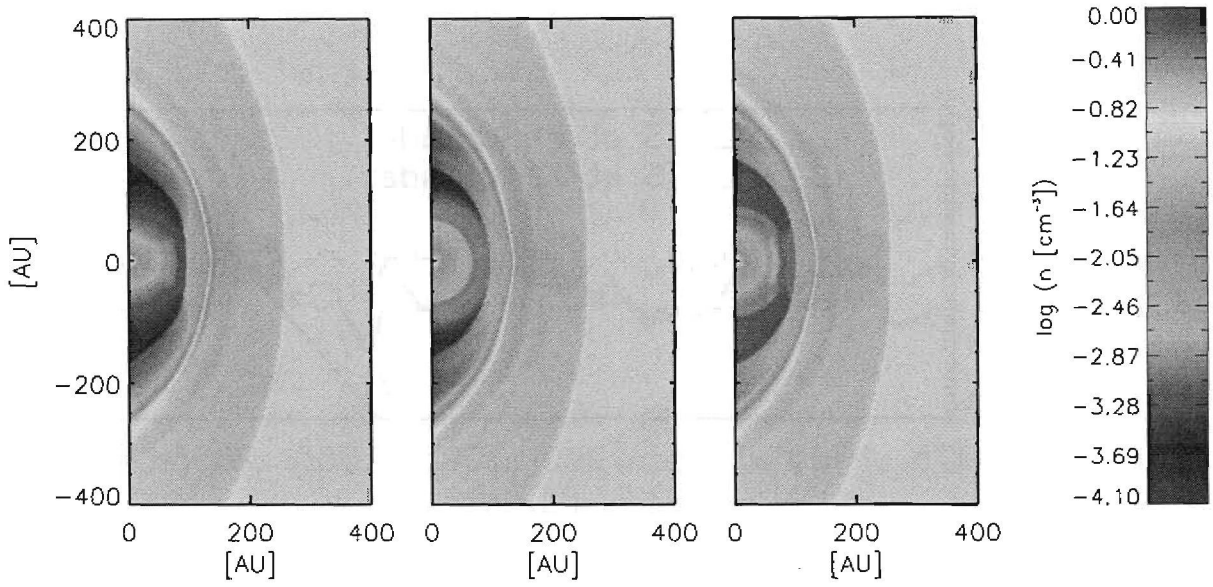

Figure 5.11: The proton density in the nose and polar regions of the heliosphere during solar minimum 1996 (left panel), solar maximum 2001 (middle panel) and in 2005, approaching solar minimum (right panel). During solar maximum the short term variations in the SW from Fig.(5.9) are used to describe the SW state at 1 AU over all solar latitudes. As solar minimum is approached the fast SW approaches a smooth stream characterised by a density of 2.5 cm^{-3} at 1 AU, over all fast SW latitudes. Note that the logarithm of the density is shown in order to resolve the contrast between regions characterised by different densities to a better extent.

sities measured by both spacecraft (Webber, private communication) indicates that Voyager 2 crossed the TS in August 2007.

The results in the middle and lower panels of Fig.(5.12) are consistent with earlier results by *Belcher et al.* (1993); *Whang and Burlaga* (2000); *Stone and Cummings* (2001) and *Webber* (2005). *Belcher et al.* (1993) found that short term SW variations may cause the TS position to change by $\pm \sim 10$ AU per year. This can be seen by comparing Figs.(5.6) and (5.12) where the TS position changes much more dramatically in the latter figure due to the presence of additional short term SW variations. *Whang and Burlaga* (2000) estimated that Voyager 1 will be close to crossing the TS in 2000. This is reflected in Fig.(5.12) within a margin of error of ± 2 years. Similar to the results presented by *Stone and Cummings* (2001) and *Webber* (2005) it is found that Voyager 1 was in close proximity to the TS for a sustained period in time after 2002 before finally crossing the TS in December 2004.

The correlation between the predicted (from Fig.5.12) and actual crossing of the TS by Voyager 2 offers important information regarding the geometry and dynamics of the heliosphere. If Voyager 2 indeed crossed the TS in 2007 (as predicted by all three of the above cases), it suggests that the heliosphere (or at least the SW plasma between the Sun and HP) acts as a hydrodynamical system. This implies that the heliospheric magnetic field is dynamically unimportant so far as the symmetry of the heliosphere about the solar equatorial plane is concerned, since the method used to estimate Voyager 2's crossing of the TS assumes that the heliosphere

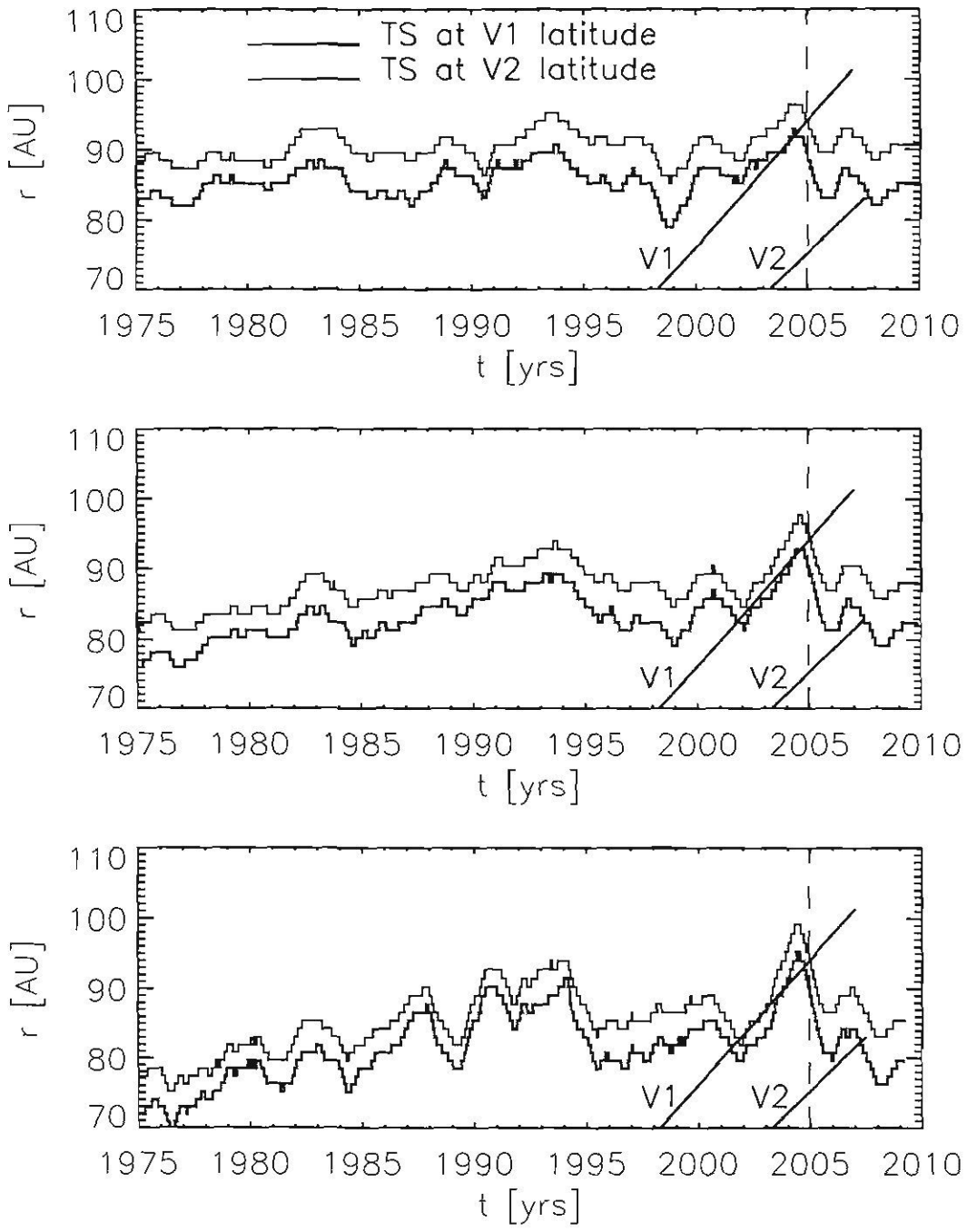

Figure 5.12: The calculated radial heliocentric position of the TS at 34.1^0 latitude (solid black line) and at -27^0 latitude (solid blue line). The top, middle and bottom panels show the TS position calculated from lower, mean and upper limit values in Fig.(5.9). The calculated TS position at all latitudes is decreased by a constant value so that the TS at 34.1^0 latitude is found at a radial distance of 94 AU, corresponding to the known time of crossing by Voyager 1. Also shown are the radial positions of both Voyager 1 and 2 (V1 and V2) in time. The vertical dashed line indicates the time at which Voyager 1 crossed the TS.

is symmetric about the solar equatorial plane. However, as suggested by *Opher et al.* (2006), depending on the relative orientation between the heliospheric and interstellar magnetic fields, severe asymmetries may occur between the regions either side of the solar equatorial plane. If the predicted crossing of the TS by Voyager 2 is correct it, therefore, reduces the probability of such asymmetries occurring on a global scale. Furthermore, if the SW acts as a hydrodynamical fluid (implying that the magnetic field does not severely alter its bulk properties) the solar magnetic field should, to a good approximation, be advected by the SW plasma. Therefore, relatively good descriptions of the average heliospheric magnetic field (HMF) can be obtained without necessarily performing a self consistent MHD calculation.

Fig.(5.12) also offers interesting information regarding the approach of the TS by Voyager 1. In all three cases it is shown that as Voyager 1 approached the TS at the beginning of 2002 the TS itself was moving outward at a velocity comparable to that of Voyager 1. However, the distance between Voyager 1 and the TS between 2002 and 2004 differs depending on which panel in Fig.(5.12) is used. Looking at the TS position from lower limit values, it can be seen that Voyager 1 was $\sim$ 5 AU away from the TS between 2002 and 2004. Looking at the TS position from mean values it can be seen that Voyager 1 almost crossed the TS in 2002 where after it stayed in close contact with the TS before finally crossing it in 2004. Lastly, looking at the TS position from the upper limit values it can be seen that Voyager 1 repeatedly crossed the shock between 2002 and 2003 whereafter the distance between Voyager 1 and the TS increased before Voyager 1 finally crossed the shock in December 2004.

In *Webber* (2005) proton intensities > 0.5 MeV measured by Voyager 1 are used to investigate Voyager 1's approach to the TS. Assuming that particles are accelerated at the TS (see *Fichtner*, 2001, for a review) and beyond (see *Ferreira et al.*, 2007), it follows that energetic particle intensities should increase as the TS is approached. Exactly how far from the TS such an increase would be visible depends on the transport coefficients of such energetic particles. Regarding the > 0.5 MeV proton intensities measured by Voyager 1 *Webber* (2005) suggests that the increased intensities measured by Voyager 1 during $2002 - 2003$ arised from Voyager 1 being close to the TS (or repeatedly crossing it) during this interval in time. The intensity observed by Voyager 1 drops in 2003 before steadily increasing towards December 2004, when Voyager 1 crossed the TS for the last time, entering the inner heliosheath.

The analyses of *Webber* (2005) suggests an application within the context of cosmic ray modulation. Using the steady state heliosphere from section 4.5 the values of the diffusion coefficients describing the diffusion of 10 MeV cosmic ray electrons can be calculated by using a cosmic ray modulation model, similar to the procedure followed by *Ferreira et al.* (2004b) and *Ferreira et al.* (2007). Using these calculated diffusion coefficients an analysis similar to that of *Webber* (2005) is presented in order to gauge how close Voyager 1 had to be to the TS between 2002 and 2004 in order to observe the increased 10 MeV electron intensities shown in the next section. This calculation will then be used to constrain the results shown in Fig.(5.12) further. This is done in the next section.

5.4 Cosmic ray modulation and the approach of the TS by both Voyager spacecraft

Cosmic rays (CR's) are broadly defined as ionized energetic particles of extraterrestrial origin ranging in energy between a couple of keV (where 1 keV $= 10^3$ eV) up to $\sim 10^{21}$ eV. Depending on their origin CR's can be divided into four different populations. CR's associated with coronal mass ejections (events were a huge mass of solar plasma is ejected into interplanetary space) are called solar CR's. A second population of energetic particles originate at Jupiter. These particles are electrons with energies between 1 and 10 MeV (where 1 MeV $= 10^6$ eV) and are referred to as Jovian electrons (see for example *Ferreira*, 2005; *Heber et al.*, 2007, for reviews). A third CR population originates from PUI's being accelerated to CR energies at the TS (as briefly mentioned in sections 3.2 and 4.2). This population is referred to as anomalous CR's (see for example *Fichtner*, 2001; *Cummings and Stone*, 2007; *Ferreira et al.*, 2007). A fourth population of energetic particles originate outside the heliosphere, presumably accelerated to CR energies at supernova blast waves (see for example *Axford et al.*, 1977; *Blandford and Ostriker*, 1978; *Koyama et al.*, 1995). These particles are referred to as galactic CR's (GCR's). The focus of this section will be on the modulation of 10 MeV GCR electrons.

A natural consequence of diffusive shock acceleration is that the differential energy spectrum j of the accelerated particles is proportional to a power law in energy (see for example *Jones and Ellison*, 1991). For GCR's it follows that $j \propto E^{-\gamma}$ where γ is constant and E is the kinetic energy per particle. j is defined in terms of the particle rigidity R and distribution function f as $j = R^2 f$. The rigidity is defined as $R = pc/q$ where p is the particle momentum, c the speed of light and q the absolute value of the particle charge. As CR's encounter the heliosphere different modulation processes cause a departure from the $E^{-\gamma}$ proportionality.

When GCR's enter the heliosphere, irregularities in the heliospheric magnetic field (HMF) cause rapid changes in their pitch angles (defined to be the angle between the particle's velocity vector and the mean magnetic field direction). These stochastic changes in pitch angle cause the GCR particle motions to approximate random walks between successive scattering interactions. The net result of these random walks is diffusion. Since GCR's are charged particles they diffuse differently parallel to a magnetic field line than perpendicular to it. Therefore, GCR diffusion is an anisotropic process described by a set of diffusion coefficients that control diffusion parallel and perpendicular to the mean magnetic field direction.

GCR's also experience drift motions due to gradients, curvatures and current sheets forming in the HMF. Lastly, the SW also modulates CR particles through convection. GCR's convected with the SW experience adiabatic acceleration or deceleration, depending on the divergence of the SW flow (see for example *Scherer and Ferreira*, 2005; *Ferreira et al.*, 2007). These modulation processes (diffusion, drift, convection and energy changes) can be combined in a kinetic transport equation, following from *Parker* (1965) as

$$\frac{\partial f}{\partial t} = \nabla \cdot (\mathbf{K} \cdot \nabla f) - \mathbf{v} \cdot \nabla f + \frac{1}{3}(\nabla \cdot \mathbf{v}) \frac{\partial f}{\partial \ln R} + Q \tag{5.9}$$

where f is the CR distribution function, t the time and $\mathbf{K}$ is the diffusion tensor (containing the coefficients describing anisotropic diffusion and HMF induced drifts. See for example *Burger and Hattingh, 1998; Burger et al., 2000,* for details on the diffusion tensor). In Eq.(5.9), $\mathbf{v}$ is the SW velocity and R is the rigidity as before. Q is a source function (used to describe CR sources within the heliosphere). From left to right the terms on the right side of Eq.(5.9) describe diffusion and drift, convection, energy changes and sources. Since this section focuses on GCR's only it can be assumed that $Q = 0$. For a more detailed review of the processes contained in Eq.(5.9) see *Potgieter* (1998).

The departure from the $E^{-\gamma}$ proportionality of the differential energy spectrum is also energy dependent. At the extreme high energy end of the energy spectrum galactic cosmic rays are negligibly affected by modulation processes in the heliosphere. Lower energy particles are more modulated due their smaller mean free paths. For electrons the modulated differential energy spectrum (observed at Earth) tends to $j \propto E^{-\gamma}$ above $\sim$ 20 GeV but departs noticeably from this proportionality at lower energies. For low energy electrons (electrons with energies less than $\sim$ 300 MeV) diffusion is the dominant modulation process (see for example *Ferreira,* 2005). This aspect of CR electron modulation will be used to constrain the results presented in Fig.(5.12) as is explained next.

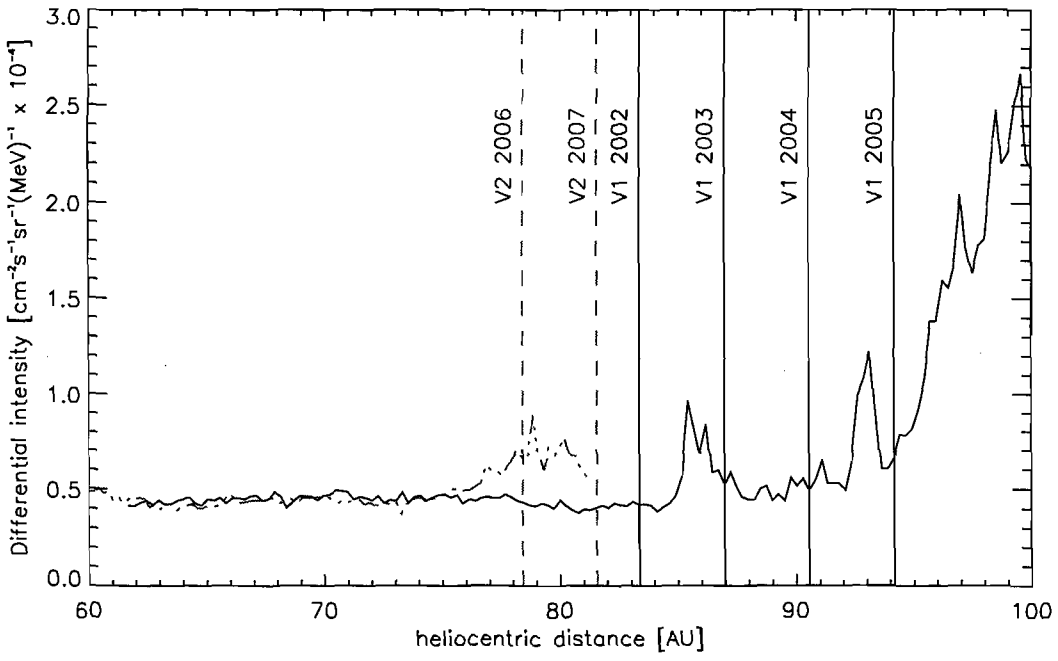

Figure 5.13: The differential intensity of 10 MeV electrons, observed by Voyager 1 (black line) and Voyager 2 (red dashed tripple dotted line) at different radial positions (McDonald private communication 2007). The radial position of Voyager 1 at the beginning of 2002, 2003 and 2004 is indicated by the vertical black lines. Similarly the radial position of Voyager 2 at the beginning of 2006 and 2007 is indicated by vertical dashed red lines.

Shown in Fig.(5.13) are recent observations from both Voyager 1 and 2 showing the 10 MeV electron differential intensity observed along the respective spacecraft trajectories (McDonald private communication 2007). Evident from Fig.(5.13) is that the observed 10 MeV electron intensities between the Sun and TS (the latter being at $\sim$ 94 AU during December 2004 along the Voyager 1 trajectory) showed very little variation, with the exception of a brief period in time between $\sim$ 2002.3 ($\sim$ 84.6 AU) and $\sim$ 2003.2 ($\sim$ 87.8 AU) for Voyager 1 and a similar period between $\sim$ 2005.3 ($\sim$ 76.8 AU) and $\sim$ 2006.9 ($\sim$ 81.2 AU) for Voyager 2. After Voyager 1 crossed the TS in 2004.9 a steady increase in the observed 10 MeV electron intensity is visible with increasing radial distance. However, the intensity increases observed by Voyager 1 between $\sim$ 2002.3 and $\sim$ 2003.2 (before Voyager 1 crossed the TS) requires some explanation.

As can be seen from the middle and lower panels in Fig.(5.12) this period in time corresponds to Voyager 1 being in close proximity to the TS. In Fig.(5.12) it is shown that between $\sim$ 2000 and $\sim$ 2002 the TS moved closer to the Sun whereafter its motion was reversed. From Fig.(5.13) it can be seen that the differential intensity increases with increasing radial distance beyond the TS. Regarding the inward motion of the TS this implies that the region beyond the TS characterised by higher intensities of 10 MeV electrons also moved closer to the Sun between $\sim$ 2000 and $\sim$ 2002 (assuming that the time scales required for 10 MeV electrons adjusting to a new TS position is much less than the time scales characterising the movement of the TS itself). As the TS subsequently reversed its motion and moved away from the Sun these regions of higher 10 MeV electron intensities were left in the TS's wake. Since it is assumed that the 10 MeV electrons adjust relatively quickly to a new TS position (compared to the TS motion itself) it follows that these high intensity remnants should disappear within comparitively short periods of time. However, regarding the increased electron intensities observed by Voyager 1 before it crossed the TS in 2004.9 it needs to be calculated how quickly these remnants of high intensities disappeared. Such a calculation will give an estimate as to how far Voyager 1 had to be from the TS between mid-2002 and mid-2003 in order for the spacecraft to still observe remnants of high electron intensity regions left behind by the TS. The results can then be used to constrain the results in Fig.(5.12).

The first step in this process is to use a numerical CR modulation model (see for example *Le Roux and Potgieter*, 1995; *Hattingh*, 1998; *Steenberg and Moraal*, 1999; *Langner and Potgieter*, 2005; *Ferreira et al.*, 2007) to calculate the 10 MeV electron differential intensities along the Voyager 1 trajectory. These results are constrained by comparing the calculated intensities with 10 MeV electron observations from Voyager 1. Using the 'best fit' calculated intensities the diffusion coefficients affecting electrons can be calculated. Since diffusion dominates the transport and modulation of low energy electrons the calculated diffusion coefficients can be used to calculate an upper limit of the distance Voyager 1 had to be from the TS in order to observe remnants of the higher intensity regions left behind by the TS.

The CR modulation model used here is discussed in *Ferreira et al.* (2007). The model uses the radial position of the TS and HP at different heliographic latitudes as input parameters, as

well as the SW flow and the heliospheric magnetic field (HMF). These are calculated from the multi-species model presented in Chapter 4 with parameters adjusted so that the TS forms at 94 AU in the nose. Assuming that the HMF is embedded in ('frozen' into) the SW plasma the induction equation

$$\frac{\partial \mathbf{B}}{\partial t} + \nabla \times (\mathbf{v} \times \mathbf{B}) = 0 \tag{5.10}$$

where $\mathbf{v}$ is the SW velocity, is solved to obtain the magnetic field $\mathbf{B}$. It is assumed that all GCR electron modulation occurs between the Sun and HP. The HP position at different latitudes defines the outer boundary of the CR modulation model where the unmodulated local interstellar spectrum of *Langner et al.* (2001) is specified.

The diffusion coefficients used in the electron modulation model are similar to the coefficients calculated by *Teufel and Schlickeiser* (2002). From the latter the expression for the electron parallel mean free path (from the 'damping model') at 1 AU is

$$\lambda_{||} = (0.0106 \text{ AU})\, \lambda_0 \left(\frac{R}{R_{MV}}^{1/3} + \frac{3.57}{\left(\left(\frac{R_0}{R_{MV}} \right)^2 + \left(\frac{R}{R_{MV}} \right)^2 \right)^{1/4}} \right) \tag{5.11}$$

where λ_0 depends on the ratio of the background magnetic field and the magnitude of the magnetic field fluctuations at 1 AU. R is the rigidity, $R_{MV} = 1$ MV (where 1 MV is 10^6 V) and $R_0 = 0.511$ MV. The parallel mean free path at some distance r greater than 1 AU is obtained by multiplying Eq.(5.11) with a calculated scaling factor, similar to the procedure followed by *Ferreira et al.* (2007). The scaling factor is calculated from the ratios of the magnetic field magnitudes at Earth and at a position r (using the calculated magnetic field from Eq.5.10). This ratio is then multiplied by r^{-1} which yields an almost constant value (as noted in *Ferreira et al.*, 2007). The parallel mean free path and the parallel diffusion coefficient are related through

$$\kappa_{||} = \frac{v}{3} \lambda_{||} \tag{5.12}$$

where v is the particle speed. Subsequently the diffusion coefficient describing diffusion parallel to the magnetic field (for 10 MeV electrons beyond 1 AU) can be calculated as

$$\kappa_{||} = 8.6 \times 10^{21} \text{ cm}^2.\text{s}^{-1}. \tag{5.13}$$

where

$$\lambda_{||} = 5.79 \times 10^{-2} \text{ AU} \tag{5.14}$$

which is slightly lower than the *Palmer* (1982) consensus, but still realistic when compared to observations at Earth (see for example *Dröge*, 2000). The diffusion coefficients describing diffusion perpendicular to the magnetic field are $\kappa_{\perp,r}$ and $\kappa_{\perp,\theta}$. In a plane polar heliocentric coordinate system $\kappa_{\perp,r}$ describes diffusion perpendicular to the magnetic field in the radial direction while $\kappa_{\perp,\theta}$ describes diffusion perpendicular to the magnetic field in the tangential direction defined in Fig.(2.4). Following *Giacalone and Jokipii* (1999) and *Le Roux et al.* (1999) it is assumed that $\kappa_{\perp,r}$ and $\kappa_{\perp,\theta}$ can be obtained by multiplying $\kappa_{||}$ by some constant factor. Subsequently (from *Ferreira*, 2001) it is assumed that

$$\kappa_{\perp,r} = 0.01\kappa_{||} \text{ and } \kappa_{\perp,\theta} = 0.015\kappa_{||}. \tag{5.15}$$

The value of $\kappa_{||}$ in Eq.(5.13) is such that any remnants of high intensities left in the wake of the TS disappear almost immediately. As shown in the approximation that follows, the electrons diffuse away so quickly that Voyager 1 had to be less than 0.1 AU from the TS in order to observe the increased intensities shown in Fig.(5.13) between 2002.3 and 2003.3.

Using the radial positions of the TS and HP at different latitudes (from model 5 in section 4.5) the CR modulation model is applied to obtain the 10 MeV electron differential intensities along Voyager 1's trajectory, as shown in Fig.(5.14). For these calculations the local interstellar spectrum of *Langner et al.* (2001) is used. Also shown are the actual differential intensities observed by Voyager 1 (McDonald private communication 2007). In order to fit the calculated intensities to the observed intensities the $\kappa_{||}$ (from Eq.5.13) is multiplied by a constant factor (from Eq.5.15 such a procedure implies that $\kappa_{\perp,r}$ and $\kappa_{\perp,\theta}$ are also multiplied by the same factor).

Shown as reference is the calculated 10 MeV electron differential intensity where the value of the parallel diffusion coefficient was assumed to be 80 times greater (everywhere in the heliosphere) than the value given in Eq.(5.13). From the calculated differential intensity it can be seen that such a large diffusion coeficient (implying a larger mean free path from Eq.5.12) corresponds to very little modulation taking place between the TS and HP. From the observed intensities it is seen that the 10 MeV electron intensity shows a very small radial gradient between the Sun and TS, while beyond the TS the radial gradient steepens. Therefore, better correlation between the observed intensities and model calculations can be obtained by assigning a relatively large value to $\kappa_{||}$ for the regions between the Sun and TS and using a relatively small value between the TS and HP. This procedure is justified considering the results from *Florinski et al.* (2003) and *Ferreira et al.* (2007) where the enhancement of the magnetic field in the inner heliosheath due to flow deceleration causes a decrease in the diffusion coefficients. Furthermore, it is also possible that increased turbulence in the heliosheath may decrease the diffusion coefficients. A best fit is obtained by using a value for $\kappa_{||}$ that is 80 times greater than the value given in Eq.(5.13) for the region between the Sun and TS, while the value of $\kappa_{||}$ between the TS and HP is assumed to be 0.8 times the value in Eq.(5.13). Larger values of $\kappa_{||}$

either side of the TS yield greater intensities between the Sun and TS, while reducing the radial intensity gradient between the TS and HP.

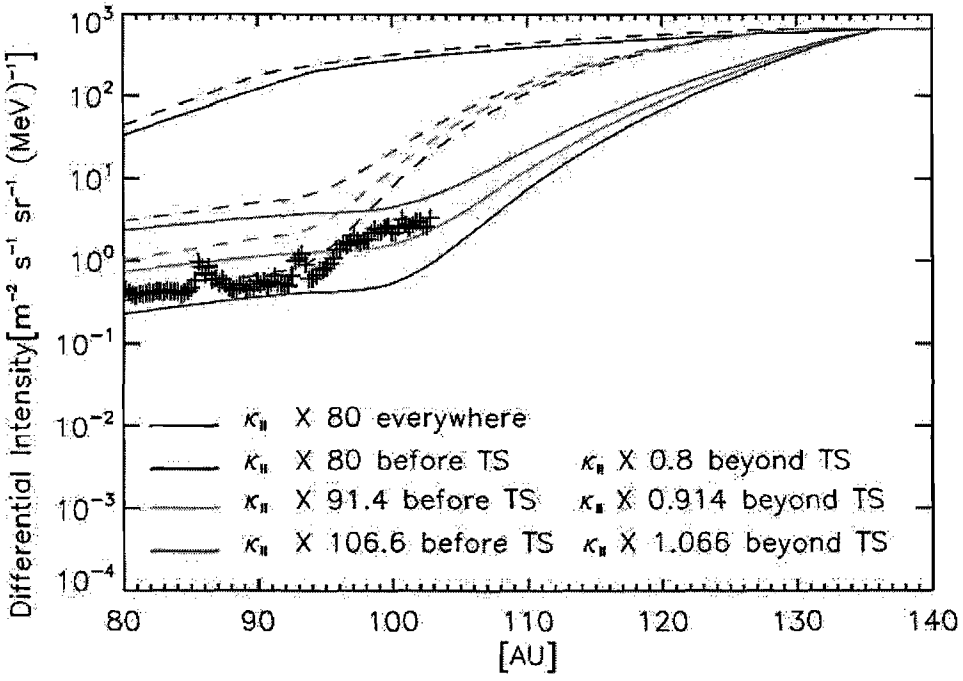

Figure 5.14: The calculated 10 MeV electron intensities along a radial path in the nose defined by $\theta = 0^0$ (solid lines) and at Voyager 1 latitudes (dashed lines). Here θ referes to the angle defined in Figs.(2.4) and (3.3). The actual intensities observed by Voyager 1 are shown by the '+' symbols (the errors on the observations are smaller than the dimensions of the symbols used). The intensities are calculated for six different scaled values of the parallel diffusion coefficient $\kappa_{||}$.

The 'best fit' value of $\kappa_{||}$ in Fig.(5.14) is now used in conjunction with Eq.(5.15) to obtain an upper limit regarding Voyager 1's proximity to the TS between 2002.3 and 2003.3. The rate of diffusion will determine the amount of time that can elapse between the TS moving outward (leaving remnants of the high 10 MeV electron intensity region between the TS and HP in its wake) and Voyager 1 still detecting remnants of these electrons at the same position at some later time. In the outer heliosphere $\kappa_{\perp,r}$ dominates diffusion (see *Ferreira*, 2001). Using the 'best fit' value of $\kappa_{||}$ (as described in the previous paragraph) from Fig.(5.14) in Eq.(5.15) yields

$$\kappa_{\perp,r} = 0.01\kappa_{||,new} \tag{5.16}$$

where $\kappa_{||,new} = 80\kappa_{||}$ and $\kappa_{||}$ is taken from Eq.(5.13). Subsequently the mean free path perpendicular to the magnetic field in the radial direction is approximated as

$$\lambda_{\perp,r} = 0.01\lambda_{||,new}. \tag{5.17}$$

where $\lambda_{||,new} = 80\lambda_{||}$ and $\lambda_{||}$ is given in Eq.(5.14). The approximate time between scattering events for electrons can be obtained from

$$T = \frac{\lambda_{\perp,r}^2}{\kappa_{\perp,r}}. \tag{5.18}$$

Using this value for $\lambda_{\perp,r}$ from Eq.(5.17) together with $\kappa_{\perp,r}$ from Eq.(5.16) yields $T = 70$ s, which approximates the time passing between two scattering interactions for a 10 MeV electron in the region between the Sun and TS. Therefore, in one year an electron will undergo approximately 450000 scattering collisions. Assuming that electron diffusion approximates a random walk this implies that the radial distance travelled by a 10 MeV electron in the pre-shock region in one year is

$$d \approx \sqrt{450000}\lambda_{\perp,r} \approx 31 \text{ AU}. \tag{5.19}$$

Therefore, as time progresses the number of 10 MeV electrons left in the wake of the TS fills an ever increasing volume. The dimensions of the volume are dominated by d calculated above (since diffusion in this region is dominated by $\kappa_{\perp,r}$). Assuming that the total number of electrons left in the wake of the shock is conserved an upper limit of the electron density after one year can be calculated from

$$\sigma_1 d = \sigma_0 \lambda_{\perp,r} \tag{5.20}$$

where σ_0 and σ_1 are the one-dimensional particle number densities after 70 s and 1 year respectively. For the one-dimensional case it is found from Eq.(5.20) that after 1 year $\sigma_1 \approx 0.001\sigma_0$. This result can be considered to be an upper limit since diffusion in other dimensions are left out of the calculation. In three dimensions the ratio of densities after 70 s and 1 year will be proportional to d^{-3}, where d is calculated by taking three dimensional diffusion into account.

Regarding Fig.(5.13) it can be seen that the maximum electron intensity observed by Voyager 1 between 2002.3 and 2003.3 is 0.4 times less than the maximum intensity observed beyond the shock. Using Eq.(5.20) this yields $d = 0.1$ AU. Since $d = 0.1$ AU is an upper limit this implies that Voyager 1 had to be closer than 0.1 AU to the shock in order to observe remnants of the increased 10 MeV electron intensities left behind by the TS.

In the above analyses it is assumed that diffusion is dominated by $\kappa_{\perp,r}$. It should be noted that parallel diffusion may well be important in this region, depending on the magnetic field structure either side of the TS. Since $\kappa_{||}$ is larger than $\kappa_{\perp,r}$ by a factor of 100 a similar analyzes to the one presented above (using $\kappa_{||}$ instead of $\kappa_{\perp,r}$) will require that Voyager 1 had to be even closer to the TS in order to observe the high intensity remnants left behind in its wake.

In the bottom panel of Fig.(5.12) it can be seen that Voyager was within $\sim$ 0.1 AU from the TS between 2001.6 and 2003.2. From Fig.(5.14) the period in time during which Voyager 1 observed increased 10 MeV electron intensities (before crossing the TS) is between $\sim$ 2002.3 and $\sim$ 2003.2. Comparison between the two figures, therefore, suggests an error in time of ± 0.7

years. This is consistent with the increased 10 MeV electron intensity observed by Voyager 2 at 2006.2. From the bottom panel of Fig.(5.12) it can be seen that in 2006.1 Voyager 2 was within a fraction of an AU from the TS, before it moved away from the spacecraft. The dates correspond to each other well within the margin of error of ± 0.7 years. Lastly the bottom panel of Fig.(5.12) suggests that Voyager 2 should have crossed the TS at $\sim$ 2007.2, while preliminary results (Webber, private communication) indicate that Voyager 2 crossed the TS in August 2007 (corresponding to $\sim$ 2007.7). Once again the two dates agree within the calculated margin of error.

In the middle panel of Fig.(5.12) it can be seen that Voyager came close to the TS in $\sim$ 2002.3 and again in $\sim$ 2003.3. This corresponds to the period in time during which Voyager 1 observed sustained increases in the 10 MeV electron intensity, as noted above. However, the maximum distance between Voyager 1 and the TS during this period of time (as suggested by the middle panel of Fig.5.12) was $\sim$ 3 AU. This suggests an error in the TS position of ± 3 AU.

The margin of error in time and position given here effectively constrain the results in Fig.(5.12). The 10 MeV electron data from Fig.(5.13) seem to be consistent with either the results calculated in the middle and lower panels of Fig.(5.12). This adds weight to the conclusions reached in the previous section that the heliosphere (between the Sun and HP) acts as a hydrodynamical system in which the magnetic field seems dynamically less important than the hydrodynamic quantities associated with the SW.

5.5 Summary

In this section it was shown how the solar cycle dependent SW can be included as a time dependent boundary condition in the numerical scheme discussed in previous chapters. It was shown that the solar cycle induces periodic changes in the heliospheric geometry and plasma flow. As the fast SW emerges during solar minimum the heliosphere is elongated in the polar regions. The periodic elongation causes the whole heliospheric structure to pulsate periodically, as illustrated by the time dependent position of the TS in the nose, polar and tail regions shown in Fig.(5.6).

The heliosphere is also sensitive to short term variations. In this chapter it was shown how the TS position changes due to short term SW variations (the latter observed by a range of spacecraft). Using these short term SW variations the time dependent position of the TS can be calculated and a prediction can be made as to when Voyager 2 will cross the TS. The predicted time of crossing (during 2007) corresponds to preliminary results that indicate Voyager 2 crossed the TS in August 2007. This correspondence suggests that the heliospheric structure between the Sun and HP act as a hydrodynamical system, and that global north-south asymmetries produced by the magnetic field (which is not included self consistently in the hydrodynamic formulation) are unlikely.

Lastly a CR modulation study was used to constrain the time dependent TS position calculated from the hydrodynamical model. It was found that the diffusion coefficients describing 10 MeV electron transport required that Voyager 1 had to be closer than 0.1 AU to the TS in order to observe remnants of high electron intensities associated with the region beyond the shock. Using this distance a margin of error on the time dependent TS position is defined as ± 3 AU in position and ± 0.7 years in time.

The heliospheric state for the last $\sim$ 30 years calculated in this chapter can be used in time dependent cosmic ray modulation models in order to establish a record of CR intensities in the heliosphere over the past 30 years.

Chapter 6

Summary and conclusions

The aim of this work, as stated in **Chapter 1**, is to model the heliosphere realistically and dynamically. This required a numerical calculation of the SW-LISM interaction (from which the heliosphere forms). In this work it was assumed that the SW-LISM interaction can be described hydrodynamically, following the work by *Pauls and Zank* (1996); *Zank et al.* (1996); *Pauls and Zank* (1997); *Kausch* (1998) and *Fahr et al.* (2000). In this regard the numerical method used to calculate all the results presented in this work was discussed in chapter 2.

Summerising the work by *Kausch* (1998) and *LeVeque* (2002), **Chapter 2** began with an examination of the properties of constant coefficient, linear hyperbolic systems. It was shown that these systems could be decoupled into sets of linearly independent advection equations. Advection implies the transport of a quantity in a medium without affecting the medium itself. Linear advection equations are easily solvable. Given an initial state it is found that the solution to the advection equation (at some later time) merely consists of a translation of the initial state. Therefore, decoupling a set of linear hyperbolic equations (with constant coefficients) into a set of linearly independent advection equations simplifies the dynamics of the system considerably.

The chapter proceeded by showing how the set of Euler-equations could be approximated as a set of linear hyperbolic equations, with constant coefficients. This was done through a process of volume averaging. The domain of the system was divided into a set of finite volumes. The state of the system within each volume was then averaged over the extent of the volume. This procedure reduced the system to a set of piecewise constant states within each volume. The conservation of some quantity within a volume implies that the quantity may only change due to fluxes at the volume boundaries, or sources within the volume. Subsequently the system was evolved in time by calculating fluxes between adjacent volumes.

The fluxes at each volume interface were calculated by writing the Euler-equations into their quasi-linear form. This yielded the flux Jacobian matrix. The eigenvalues of the flux Jacobian matrix give the velocities with which hydrodynamical quantities propagate through the system while its eigenvectors define the phase-space trajectories of these quantities. Linearising the flux Jacobian (locally at each interface between adjacent volumes) reduced the quasi-linear

Euler equations to a set of advection equations. The fluxes into and out of each volume were then calculated from this set.

The chapter concluded by showing how the numerical algorithm could be made compliant with physical entropy conditions by ensuring that the numerical viscosity of the system remains above a certain threshold. Furthermore, it was shown how non-physical solutions could be avoided by using the HLLE-solver, which used an alternative flux function to evolve the system in time. Lastly, it was shown how second order accuracy could be obtained for regions in the system where data was approximately continuous.

In **Chapter 3** the numerical method from Chapter 2 was applied to the SW-LISM interaction, where it was assumed that both the SW and LISM consisted solely of protons. In order to apply the numerical scheme, appropriate boundary conditions describing the SW and LISM state had to be defined. To this end a review of observational evidence describing the SW and LISM states were given.

It was shown that the structure of the heliosphere necessarily consisted of three interfaces, called the termination shock (TS), heliopause (HP) and bow shock (BS). It was shown that these three interfaces formed as waves, initially propagating away from the initial point of contact between the SW and LISM, became stationary. From the flux Jacobian calculated in Chapter 2 it was shown that two of these waves became stationary at sonic points, implying that two of the interfaces (the TS and BS) were stationary transonic shocks in the steady state solution of the SW-LISM interaction problem. The third interface (the HP) became a stationary wave at a point where the velocities either side of it tended to zero. This implied that the HP had to be a contact discontinuity.

The characteristics of the heliosphere in two dimensions were also discussed. It was shown that the TS envelops a region in which the SW expansion is supersonic, radial and adiabatic. At the TS the SW undergoes a transition to a subsonic flow. In the nose and polar regions the SW flow acquires an appreciable tangential velocity component between the TS and HP. It was further shown that a tangential pressure gradient between the TS and HP re-accelerates the SW to supersonic velocities in the polar regions of the inner heliosheath. The two dimensional geometry of the heliosphere was shown and discussed. The TS had a characteristic 'bullet shape' while the HP and BS formed two bow-like structures in the nose and polar regions. It was shown that while the HP is a contact discontinuity in the nose it broadens into a thin transition region towards the polar regions.

The chapter concluded with a parameter study. From the observational evidence reviewed in the beginning of the chapter a set of different plausible boundary conditions describing the SW and LISM state were defined. The heliosphere was then calculated for each different boundary condition. From the parameter study it was concluded that the dynamic pressure of either the SW or the LISM is the parameter affecting the heliosphere most. For cases where a higher SW (or lower LISM) dynamic pressure was assumed at either boundary the TS, HP and BS formed

further away from the Sun. The opposite applied to lower SW (or higher LISM) dynamic pressures assumed at either boundary. Furthermore, it was found that the heliosphere is not sensitive to a range of SW temperatures, and only slightly so for different LISM temperatures.

In **Chapter 4** a more complete description of the SW-LISM interaction was given. In this chapter the effect of neutral atoms in the LISM on the heliosphere was discussed. It was shown how the mutual interaction between protons and neutral atoms were included in the hydrodynamical formulation of the SW-LISM interaction problem by defining appropriate mass, momentum and energy source terms coupling the different particle species. These source terms were included in the numerical method discussed in Chapter 2.

Neutral atoms enter the region influenced by the heliosphere at the BS. Between the BS and HP (in the nose) charge exchange between neutral atoms and protons causes a build-up of neutral atoms (called the 'hydrogen wall'). Neutral atoms propagating past the HP interact with the SW through charge exchange, electron impact ionisation (in the outer heliosheath) and photoionisation (close to the Sun). These interactions lead to a third particle species forming in the SW, called pick-up ions (PUI's).

The effect of neutral atoms on the heliosphere was explicitly shown. Between the Sun and TS the interaction with neutral atoms decelerated and heated the subsonic SW while the SW density was significantly enhanced beyond the TS. Furthermore, neutral atoms reduced the asymmetry of the TS, compared to the characteristic 'bullet shape' found in Chapter 3.

The chapter concluded with a parameter study similar to Chapter 3. The heliosphere was calculated from a set of different boundary conditions describing the SW state close to the Sun and the LISM state at large heliocentric distances. Similar to Chapter 3, it was found that the dynamic pressure of either the SW or the LISM proton populations determines the structure of the heliosphere more than any other parameter (within the tested range of values). However, compared to the results from Chapter 3 it was shown that the inclusion of neutral atoms reduced the effect larger assumed values of the SW dynamic pressure had on the heliosphere. Similarly, neutral atoms to some extent reduced the effect higher or lower LISM dynamic pressures had on the structure of the heliosphere.

The results of the parameter study were compared to results from *Müller et al.* (2006), where an alternative hydrodynamic description of the neutral particle species is used. It was found that the two descriptions yielded similar results regarding the TS and HP positions, as well as the number of neutral particles that enter the region between the Sun and HP. From this it could be concluded that the hydrodynamic formulation used in this work calculated the SW flow between the Sun and HP (as well as the positions of the TS and HP) accurately. In the context of cosmic ray modulation the model used here, therefore, provides an optimal trade-off between computation time and accuracy since the model calculates parameters used in cosmic ray modulation studies (the SW flow and positions of the HP and BS) with sufficient accuracy, while being computationally more efficient than other (more complex) models. This made it

possible to do the dynamic calculations presented in Chapter 5 within relatively short periods of time.

In **Chapter 5** the heliosphere is investigated as a time dependent structure. From the SW observations presented in Chapter 3 it followed that the SW state changes with the solar activity cycle. During solar minimum a fast, less dense SW stream emerges at higher solar latitudes. As solar maximum is approached the fast SW disappears and the SW becomes approximately uniform at all latitudes. It was shown how the solar cycle dependent SW could be included in the hydrodynamical model by using a time and latitude dependent boundary condition.

The solar cycle dependent SW caused periodic changes in the heliosphere. During solar minimum the fast SW stream elongated the heliosphere along the solar axis of rotation. Furthermore, the transition between solar minimum and solar maximum produced a series of rarefaction waves propagating through the inner heliosheath. The passage of these rarefied regions induced rotational flows in the lower latitude regions beyond the TS in the tail. Furthermore, the solar cycle dependent SW caused the TS to pulsate at all latitudes in response to the solar cycle. The effect was greatest in the polar regions but still significant in the nose and tail regions of the heliosphere. It was also shown that the TS response between different latitudes were out of phase with one another.

Short term variations in the SW state (as observed by a range of spacecraft) were also included in the hydrodynamic model. The characteristics of the SW expansion between the Sun and TS (as investigated for a range of parameters in Chapter 4) was used to extrapolate spacecraft observations back to 1 AU, which corresponded to the inner boundary of the numerical model. Using data from various spacecraft (between 1975 and the present) allowed for the calculation of a data set (of SW parameters at 1 AU at different 26-day intervals) which could be used as a time dependent boundary condition in the hydrodynamic model of the SW-LISM interaction. Together with the solar cycle, this allowed for the calculation of a record of the state of the heliosphere over the past $\sim$ 30 years.

From the calculated record of the heliosphere the TS position (at both Voyager 1 and 2) latitudes could be calculated as it changed in time. From these results it was predicted when Voyager 2 would cross the TS. Using lower, mean and upper limit values of spacecraft observations it was found that Voyager 2 should cross the TS in 2007. This corresponded to preliminary results (Webber, private communication 2007) which indicated that Voyager 2 crossed the TS in August 2007.

The chapter concluded by constraining the record of the heliosphere using 10 MeV cosmic ray electron observations. It was shown that as Voyager 1 approached the TS (before crossing it in December 2004) it observed sustained increases in the 10 MeV electron intensity. In this section it was assumed that these intensity increases were remnants left behind by the outward moving TS. Using a cosmic ray modulation model it was determined that Voyager 1 had to be less than 0.1 AU from the shock to observe these remnants before they diffused away. This

calculation allowed for the heliospheric record to be constrained. The TS position calculated from mean and upper limit values were accurate within ± 3 AU and 0.7 years respectively.

Regarding the results presented in this work the following conclusions can be made:

- The heliosphere can be modelled accurately and time dependently using the hydrodynamic model discussed in this work. This followed from the correlation between the predicted time at which Voyager 2 will cross the TS (calculated from the model) and the actual time of crossing (Webber, private communication 2007). The accuracy of the model is also reflected in the 10 MeV electron observations made by Voyager 1. From these observations it could be shown that Voyager 1 had to be less than 0.1 AU from the TS between $\sim$ 2002.3 and $\sim$ 2003.2. This corresponded with the distance between Voyager 1 and the TS calculated from the hydrodynamic model within a margin of error of ± 0.7 years and ± 3 AU. In this sense the aim of this study was achieved, in that the heliosphere was modelled accurately and time dependently using a hydrodynamic model of the SW-LISM interaction.
- From the correspondence between the predicted and actual time of Voyager 2 crossing the TS it can further be concluded that the heliosphere (at least in the region spanned by the trajectories of Voyager 1 and 2) acts as a hydrodynamic system. Implicit to the hydrodynamic formulation used in this work is the assumption that the heliosphere is symmetric about the solar equatorial plane. The correlation between the calculated and predicted time at which Voyager 2 crosses the TS, therefore, reduces the likelihood that the heliospheric magnetic field (HMF) produces significant global asymmetries with respect to the solar equatorial plane.
- Regarding cosmic ray modulation studies it follows that an accurate time dependent description of the heliosphere can be obtained from a purely hydrodynamic model, as presented here. The hydrodynamic model discussed here calculates the SW flow and positions of the TS and HP accurately and time efficiently, which implies that time dependent CR modulation models can calculate results time efficiently, while still maintaining a high degree of accuracy regarding heliospheric parameters affecting CR modulation.

For future studies it is recommended that:

- The heliospheric record calculated in this work should be used with a time dependent cosmic ray modulation model to calculate CR modulation in this dynamic environment.
- A similar analysis as the one applied in this work to 10 MeV electron intensities should be applied to observed anomalous cosmic ray observations from Voyager 1 and Voyager 2.
- The heliospheric model could be extended to include diffusion and viscosity, especially in resolving the transitional region between the fast and slow SW during solar minimum.

- The possibility of extending the heliospheric model to three dimensions should be investigated. This would allow for the inclusion of longitudinal effects in the SW.
- The numerical scheme used for the hydrodynamic model could be modified so that the volumes of the cells (over which quantities are averaged) can be adjusted during each time step. This would allow for better resolution close to interesting phenomena (such as the TS) without increasing the computational time unnecessarily.

Bibliography

Allen, C. W., *Astrophysical quantities*, London: University of London, Athlone Press, 3rd ed., 1973.

Anderson, R. C., R. C. Henry, H. W. Moos, and J. L. Linsky, Ultraviolet observations of cool stars. VIII - Interstellar matter toward Procyon, *Astrophysical Journal, 226*, 883–887, 1978.

Axford, W. I., A. J. Dessler, and B. Gottlieb, Termination of Solar Wind and Solar Magnetic Field., *Astrophysical Journal, 137*, 1268–1278, 1963.

Axford, W. I., E. Leer, and G. Skadron, The Acceleration of Cosmic Rays by Shock Waves, in *International Cosmic Ray Conference, International Cosmic Ray Conference*, vol. 11, pp. 132–137, 1977.

Baranov, V. B., and Y. G. Malama, Model of the solar wind interaction with the local interstellar medium - Numerical solution of self-consistent problem, *Journal of Geophysical Research, 98*, 15,157–15,163, 1993.

Belcher, J. W., A. J. Lazarus, R. L. McNutt, Jr., and G. S. Gordon, Jr., Solar wind conditions in the outer heliosphere and the distance to the termination shock, *Journal of Geophysical Research, 98*, 15,177–15,183, 1993.

Biermann, L., Kometenschweife und solare Korpuskularstrahlung, *Zeitschrift fur Astrophysik, 29*, 274–286, 1951.

Biermann, L., Solar corpuscular radiation and the interplanetary gas, *The Observatory, 77*, 109–110, 1957.

Blandford, R. D., and J. P. Ostriker, Particle acceleration by astrophysical shocks, *Astrophysical Journal, 221*, L29–L32, 1978.

Burger, R. A., and M. Hattingh, Toward a Realistic Diffusion Tensor for Galactic Cosmic Rays, *Astrophysical Journal, 505*, 244–251, 1998.

Burger, R. A., M. S. Potgieter, and B. Heber, Rigidity dependence of cosmic ray proton latitudinal gradients measured by the Ulysses spacecraft: Implications for the diffusion tensor, *Journal of Geophysical Research, 105*, 27,447–27,456, 2000.

Chassefiere, E., J. L. Bertaux, R. Lallemant, and V. G. Kurt, Atomic hydrogen and helium densities of the interstellar medium measured in the vicinity of the sun, *Astronomy and Astrophysics, 160*, 229–242, 1986.

Chen, F. F., *Introduction to plasma physics*, New York: Plenum Press, 1974.

Cummings, A. C., and E. C. Stone, Composition of Anomalous Cosmic Rays, *Space Science Reviews, 130*, 389–399, 2007.

Cummings, A. C., E. C. Stone, and C. D. Steenberg, Composition of Anomalous Cosmic Rays and Other Heliospheric Ions, *Astrophysical Journal, 578*, 194–210, 2002.

Dröge, W., The Rigidity Dependence of Solar Particle Scattering Mean Free Paths, *Astrophysical Journal, 537*, 1073–1079, 2000.

Dworsky, A., and H. J. Fahr, Ion acceleration in connection with a modulated solar wind termination shock: phase space propagation and complete energy spectra, *Astronomy and Astrophysics, 353*, L1–L4, 2000.

Fahr, H. J., Non-Thermal Solar Wind Heating by Supra-Thermal Ions, *Solar Physics, 30*, 193–206, 1973.

Fahr, H. J., and M. Bzowski, A kinetic control of the heliospheric interface hydrodynamics of charge-exchanging fluids, *Astronomy and Astrophysics, 424*, 263–278, 2004.

Fahr, H.-J., and H. Fichtner, The influence of pick-up ion-induced wave pressures on the dynamics of the mass-loaded solar wind, , *158*, 353–363, 1995.

Fahr, H. J., T. Kausch, and H. Scherer, A 5-fluid hydrodynamic approach to model the solar system-interstellar medium interaction, *Astronomy and Astrophysics, 357*, 268–282, 2000.

Fahr, H.-J., H. Fichtner, and K. Scherer, Theoretical aspects of energetic neutral atoms as messengers from distant plasma sites with emphasis on the heliosphere, *Reviews of Geophysics, 45*, G4003, 2007.

Ferreira, S. E. S., The Heliospheric Transport of Galactic Cosmic Rays and Jovian Electrons, Ph.D. thesis, Potchefstroom University for CHE, South Africa, 2001.

Ferreira, S. E. S., The transport of galactic and jovian cosmic ray electrons in the heliosphere, *Advances in Space Research, 35*, 586–596, 2005.

Ferreira, S. E. S., and K. Scherer, Time Evolution of Galactic and Anomalous Cosmic-Ray Spectra in a Dynamic Heliosphere, *Astrophysical Journal, 642*, 1256–1266, 2006.

Ferreira, S. E. S., M. S. Potgieter, and K. Scherer, Modulation of Cosmic-Ray Electrons in a Nonspherical and Irregular Heliosphere, *Astrophysical Journal, 607*, 1014–1023, 2004a.

Ferreira, S. E. S., M. S. Potgieter, and W. R. Webber, Modulation of low-energy cosmic ray electrons in the outer heliosphere, *Advances in Space Research, 34*, 126–131, 2004b.

Ferreira, S. E. S., M. S. Potgieter, and K. Scherer, Transport and acceleration of anomalous cosmic rays in the inner heliosheath, *Journal of Geophysical Research (Space Physics), 112*, 11,101–11,111, 2007.

Fichtner, H., Anomalous Cosmic Rays: Messengers from the Outer Heliosphere, *Space Science Reviews, 95*, 639–754, 2001.

Fichtner, H., J. A. Le Roux, U. Mall, and D. Rucinski, On the transport of pick-up ions in the heliosphere., *Astronomy and Astrophysics, 314*, 650–662, 1996a.

Fichtner, H., S. R. Sreenivasan, and H. J. Fahr, Cosmic ray modulation and a non-spherical heliospheric shock., *Astronomy and Astrophysics, 308*, 248–260, 1996b.

Fisk, L. A., and G. Gloeckler, The Common Spectrum for Accelerated Ions in the Quiet-Time Solar Wind, *Astrophysical Journal, 640*, L79–L82, 2006.

Fisk, L. A., B. Kozlovsky, and R. Ramaty, An Interpretation of the Observed Oxygen and Nitrogen Enhancements in Low-Energy Cosmic Rays, *Astrophysical Journal, 190*, L35–L37, 1974.

Fite, W. L., A. C. H. Smith, and R. F. Stebbings, Charge Transfer in Collisions Involving Symmetric and Asymmetric Resonance, *Proceedings of the Royal Society of London Series A, 268*, 527–536, 1962.

Florinski, V., G. P. Zank, and N. V. Pogorelov, Galactic cosmic ray transport in the global heliosphere, *Journal of Geophysical Research (Space Physics), 108*, 1228–1244, 2003.

Frisch, P. C., Morphology and Ionization of the Interstellar Cloud Surrounding the Solar System, *Science, 265*, 1423–1427, 1994.

Frisch, P. C., Interstellar Matter and the Boundary Conditions of the Heliosphere, *Space Science Reviews, 86*, 107–126, 1998.

Frisch, P. C., The local bubble and interstellar material near the Sun, *ArXiv e-prints*, 2007.

Frisch, P. C., and J. D. Slavin, The Sun's journey through the local interstellar medium: the paleoLISM and paleoheliosphere, *Astrophys. Space Sci. Trans, 2*, 53–61, 2006.

Giacalone, J., and J. R. Jokipii, The Transport of Cosmic Rays across a Turbulent Magnetic Field, *Astrophysical Journal, 520*, 204–214, 1999.

Gloeckler, G., et al., The Solar Wind Ion Composition Spectrometer, *Astronomy and Astrophysics Supplement Series, 92*, 267–289, 1992.

Gry, C., and E. B. Jenkins, Local clouds: Ionization, temperatures, electron densities and interfaces, from GHRS and IMAPS spectra of epsilon Canis Majoris, *Astronomy and Astrophysics, 367*, 617–628, 2001.

Haasbroek, L. J., and M. S. Potgieter, A new model to study galactic cosmic ray modulation in an asymmetrically bounded heliosphere, *Journal of Geophysical Research, 103*, 2099–2104, 1998.

Hattingh, M., The modulation of galactic cosmic rays in a three-dimansional heliosphere, Ph.D. thesis, Potchefstroom University for CHE, South Africa, 1998.

Heber, B., et al., An overview of Jovian electrons during the distant Ulysses Jupiter flyby, *Planetary and Space Science, 55*, 1–11, 2007.

Heerikhuisen, J., V. Florinski, and G. P. Zank, Interaction between the solar wind and interstellar gas: A comparison between Monte Carlo and fluid approaches, *Journal of Geophysical Research (Space Physics), 111*, 1–8, 2006.

Holzer, T. E., Interaction of the solar wind with the neutral component of the interstellar gas., *Journal of Geophysical Research, 77*, 5407–5431, 1972.

Holzer, T. E., Interaction between the solar wind and the interstellar medium, *Annual Review of Astronomy and Astrophysics, 27*, 199–234, 1989.

Holzer, T. E., and W. I. Axford, The Theory of Stellar Winds and Related Flows, *Annual Review of Astronomy and Astrophysics, 8*, 31–60, 1970.

Isenberg, P. A., Turbulence-driven Solar Wind Heating and Energization of Pickup Protons in the Outer Heliosphere, *Astrophys. J., 623*, 502–510, 2005.

Izmodenov, V. V., Modulation of galactic cosmic rays in the region of interaction of the local interstellar medium with the solar wind: Hydrodynamic approximation, *Astronomy Letters, 23*, 221–228, 1997.

Jones, F. C., and D. C. Ellison, The plasma physics of shock acceleration, *Space Science Reviews, 58*, 259–346, 1991.

Karmesin, S. R., P. C. Liewer, and J. U. Brackbill, Motion of the termination shock in response to an 11 year variation in the solar wind, *Geophysical Research Letters, 22*, 1153–1156, 1995.

Kausch, T., Ein hydrodynamisches Mehrkomponentenmodell zur Beschreibung der Wechselwirkung zwischen Heliosphäre und interstellarem Medium, Ph.D. thesis, Institut für Astronomie und Extraterrestrische Forschung der Universität Bonn, 1998.

Koyama, K., R. Petre, E. V. Gotthelf, U. Hwang, M. Matsuura, M. Ozaki, and S. S. Holt, Evidence for Shock Acceleration of High-Energy Electrons in the Supernova Remnant SN:1006, *Nature, 378*, 255–258, 1995.

Langner, U. W., and M. S. Potgieter, Effects of the position of the solar wind termination shock and the heliopause on the heliospheric modulation of cosmic rays, *Advances in Space Research, 35*, 2084–2090, 2005.

Langner, U. W., O. C. de Jager, and M. S. Potgieter, On the local interstellar spectrum for cosmic ray electrons, *Advances in Space Research, 27*, 517–522, 2001.

Le Roux, J. A., and M. S. Potgieter, The simulation of complete 11 and 12 year modulation cycles for cosmic rays in the heliosphere using a drift model with global merged interaction regions, *Astrophysical Journal*, 1995.

Le Roux, J. A., G. P. Zank, and V. S. Ptuskin, An evaluation of perpendicular diffusion models regarding cosmic ray modulation on the basis of a hydromagnetic description for solar wind turbulence, *Journal of Geophysical Research*, 1999.

Lee, M. A., and W.-H. Ip, Hydromagnetic wave excitation by ionised interstellar hydrogen and helium in the solar wind, *Journal of Geophysical Research*, 1987.

LeVeque, R. J., *Finite Volume Methods for Hyperbolic Problems*, Finite Volume Methods for Hyperbolic Problems, 1st ed. New York: Cambridge University Press, 2002, 558 p. ISBN 13978-0521-00924-9, 2002.

Lindsay, B. G., and R. F. Stebbings, Charge transfer cross sections for energetic neutral atom data analysis, *Journal of Geophysical Research (Space Physics), 110*, A12,213, 2005.

Lotz, W., Electron-Impact Ionization Cross-Sections and Ionization Rate Coefficients for Atoms and Ions, *Astrophysical Journal Supplement*, 1967.

McNutt, R. L., Jr., J. Lyon, and C. C. Goodrich, Simulation of the heliosphere - Model, *Journal of Geophysical Research, 103*, 1905–1912, 1998.

Möbius, E., et al., Synopsis of the interstellar He parameters from combined neutral gas, pickup ion and UV scattering observations and related consequences, *Astronomy and Astrophysics, 426*, 897–907, 2004.

Müller, H.-R., P. C. Frisch, V. Florinski, and G. P. Zank, Heliospheric Response to Different Possible Interstellar Environments, *Astrophysical Journal, 647*, 1491–1505, 2006.

Ngobeni, M. D., Aspects of the modulation of cosmic rays in the outer heliosphere, Master's thesis, School of Physics North-West Univeristy (Potchefstroom Campus), 2006.

Opher, M., E. C. Stone, and P. C. Liewer, The Effects of a Local Interstellar Magnetic Field on Voyager 1 and 2 Observations, *Astrophysical Journal, 640*, L71–L74, 2006.

Palmer, I. D., Transport coefficients of low-energy cosmic rays in interplanetary space, *Reviews of Geophysics and Space Physics, 20*, 335–351, 1982.

Parker, E. N., Dynamics of the Interplanetary Gas and Magnetic Fields., *Astrophysical Journal, 128*, 664–676, 1958.

Parker, E. N., The Stellar-Wind Regions., *Astrophysical Journal, 134*, 20–27, 1961.

Parker, E. N., The passage of energetic charged particles through interplanetary space, *Planetary and Space Science, 13*, 9–49, 1965.

Pauls, H. L., and G. P. Zank, Interaction of a nonuniform solar wind with the local interstellar medium, *Journal of Geophysical Research, 101*, 17,081–17,092, 1996.

Pauls, H. L., and G. P. Zank, Interaction of a nonuniform solar wind with the local interstellar medium 2. A two-fluid model, *Journal of Geophysical Research, 102*, 19,779–19,788, 1997.

Pauls, H. L., G. P. Zank, and L. L. Williams, Interaction of the solar wind with the local interstellar medium, *Journal of Geophysical Research, 100*, 21,595–21,604, 1995.

Piskunov, N., B. E. Wood, J. L. Linsky, R. C. Dempsey, and T. R. Ayres, Local Interstellar Medium Properties and Deuterium Abundances for the Lines of Sight toward HR 1099, 31 Comae, beta Ceti, and beta Cassiopeiae, *Astrophysical Journal, 474*, 315–328, 1997.

Pogorelov, N. V., Periodic stellar wind / interstellar medium interaction., *Astronomy and Astrophysics, 297*, 835–840, 1995.

Pogorelov, N. V., and T. Matsuda, Influence of the interstellar magnetic field direction on the shape of the global heliopause, *Journal of Geophysical Research, 103*, 237–245, 1998.

Pogorelov, N. V., and A. Y. Semenov, Solar wind interaction with the magnetized interstellar medium. Shock-capturing modeling., *Astronomy and Astrophysics, 321*, 330–337, 1997.

Pogorelov, N. V., G. P. Zank, and T. Ogino, Three-dimensional Features of the Outer Heliosphere Due to Coupling between the Interstellar and Interplanetary Magnetic Fields. I. Magnetohydrodynamic Model: Interstellar Perspective, *Astrophysical Journal, 614*, 1007–1021, 2004.

Pogorelov, N. V., E. C. Stone, V. Florinski, and G. P. Zank, Termination Shock Asymmetries as Seen by the Voyager Spacecraft: The Role of the Interstellar Magnetic Field and Neutral Hydrogen, *Astrophysical Journal, 668*, 611–624, 2007.

Potgieter, M. S., The Modulation of Galactic Cosmic Rays in the Heliosphere: Theory and Models, *Space Science Reviews, 83*, 147–158, 1998.

Potgieter, M. S., and U. W. Langner, Heliospheric Modulation of Cosmic-Ray Positrons and Electrons: Effects of the Heliosheath and the Solar Wind Termination Shock, *Astrophysical Journal, 602*, 993–1001, 2004.

Potgieter, M. S., and U. W. Langner, Modulation of cosmic rays: Perpendicular diffusion and drifts in a heliosphere with a solar wind termination shock, *Advances in Space Research, 35*, 554–561, 2005.

Ratkiewicz, R., A. Barnes, G. A. Molvik, J. R. Spreiter, S. S. Stahara, M. Vinokur, and S. Venkateswaran, Effect of varying strength and orientation of local interstellar magnetic

field on configuration of exterior heliosphere: 3D MHD simulations, *Astronomy and Astrophysics, 335*, 363–369, 1998.

Scherer, K., and H. J. Fahr, Breathing of heliospheric structures triggered by the solar-cycle activity, *Annales Geophysicae, 21*, 1303–1313, 2003a.

Scherer, K., and H. J. Fahr, Solar cycle induced variations of the outer heliospheric structures, *Geophysical Research Letters, 30*, 1–4, 2003b.

Scherer, K., and S. E. S. Ferreira, A heliospheric hybrid model: hydrodynamic plasma flow and kinetic cosmic ray transport, *Astrophysics and Space Sciences Transactions, 1*, 17–27, 2005.

Scherer, K., et al., Interstellar-Terrestrial Relations: Variable Cosmic Environments, The Dynamic Heliosphere, and Their Imprints on Terrestrial Archives and Climate, *Space Science Reviews, 127*, 327–465, 2006.

Slavin, J. D., and P. C. Frisch, The Boundary Conditions of the Heliosphere: Photoionization Models Constrained by Interstellar and In Situ Data, *ArXiv e-prints, 704*, 2007.

Snyman, J. L., S. E. S. Ferreira, M. S. Potgieter, and K. Scherer, Hydrodynamic modeling of the heliospheric structure, in *36th COSPAR Scientific Assembly, COSPAR, Plenary Meeting*, vol. 36, pp. 730–743, 2006.

Steenberg, C. D., and H. Moraal, Form of the anomalous cosmic ray spectrum at the solar wind termination shock, *Journal of Geophysical Research, 104*, 24,879–24,884, 1999.

Stone, E. C., and A. C. Cummings, Estimate of the Location of the Solar Wind Termination Shock, in *International Cosmic Ray Conference, International Cosmic Ray Conference*, vol. 10, pp. 4263–4266, 2001.

Teufel, A., and R. Schlickeiser, Analytic calculation of the parallel mean free path of heliospheric cosmic rays. I. Dynamical magnetic slab turbulence and random sweeping slab turbulence, *Astronomy and Astrophysics, 393*, 703–715, 2002.

Wang, C., and J. W. Belcher, The heliospheric boundary response to large-scale solar wind fluctuations: A gasdynamic model with pickup ions, *Journal of Geophysical Research, 104*, 549–556, 1999.

Webber, W. R., An empirical estimate of the heliospheric termination shock location with time with application to the intensity increases of MeV protons seen at Voyager 1 in 2002-2005, *Journal of Geophysical Research (Space Physics), 110*, 10,103–10,110, 2005.

Whang, Y. C., and L. F. Burlaga, Termination shock - Solar cycle variations of location and speed, *Journal of Geophysical Research, 98*, 15,221–15,230, 1993.

Whang, Y. C., and L. F. Burlaga, Anticipated Voyager crossing of the termination shock, *Geophysical Research Letters, 27*, 1607–1610, 2000.

Wu, C. S., and R. C. Davidson, Electromagnetic instabilities produced by neutral-particle ionization in interplanetary space., *Journal of Geophysical Research, 77*, 5399–5406, 1972.

Zank, G. P., Interaction of the solar wind with the local interstellar medium: a theoretical perspective, *Space Science Reviews, 89*, 413–688, 1999.

Zank, G. P., H. L. Pauls, L. L. Williams, and D. T. Hall, Interaction of the solar wind with the local interstellar medium: A multifluid approach, *Journal of Geophysical Research, 101*, 21,639–21,656, 1996.

Acknowledgements

I would like to thank my fiancée Leandri, her parents Derek and Matilda and her sister Izaan, as well as my parents Johan and Elisabeth, my brother Izak and my sister Magdaleen for their support during the completion of this work. I would especially like to thank my supervisors Dr. Ferreira and Prof. Potgieter for their patience, guidance and constructive input. Furthermore, I wish to thank Klaus Scherer, Horst Fichtner, Donald Ngobeni and Eugene Engelbrecht for the valuable discussions and input given throughout.

I also wish to thank the following:

- Mathew Holleran for logistical support.
- Petro Sieberhagen and Lizelle le Roux for administrative support.
- The School of Physics and the Unit for Space Science at the Potchefstroom Campus of North-West University.
- The Meraka Institute and the Centre for High Performance Computing (CHPC) for additional funding and logistical support.

Finally, the financial assistance of the National Research Foundation (NRF) towards this research is hereby acknowledged. Opinions expressed and conclusions arrived at, are those of the author and are not necessarily to be attributed to the NRF.

Jasper Snyman

Unit for Space Physics, School of Physics, Potchefstroom Campus, NWU

2520 Potchefstroom, South Africa

jasper_snyman@yahoo.com